Organic Donor-Acceptor Systems for Metal Ion Recognition and OLED Applications

THESIS SUBMITTED TO **AcSIR** FOR THE AWARD OF THE DEGREE OF

DOCTOR OF PHILOSOPHY IN CHEMISTRY

UNDER THE FACULTY OF SCIENCE

By

SHAMEEL T.

Enrollment No: 10CC12A39015

Under the Supervision of

Dr. D. RAMAIAH

PHOTOSCIENCES AND PHOTONICS SECTION

CHEMICAL SCIENCES AND TECHNOLOGY DIVISION

CSIR-NATIONAL INSTITUTE FOR INTERDISCIPLINARY SCIENCE AND TECHNOLOGY (CSIR-NIIST)

THIRUVANANTHAPURAM - 695019, KERALA

APRIL 2018

Dedicated to

My Umma, Uppa and Sajna…

DECLARATION

I hereby declare that the matter embodied in the Ph. D. thesis entitled: "**Organic Donor-Acceptor Systems for Metal Ion Recognition and OLED Applications**" is the result of an independent work carried out by me at the Photosciences and Photonics Section, Chemical Sciences and Technology Division of the CSIR-National Institute for Interdisciplinary Science and Technology (CSIR-NIIST), Thiruvananthapuram, under the supervision of Dr. D. Ramaiah and the same has not been submitted elsewhere for other degree or diploma.

In keeping with the general practice of reporting scientific observations, research materials obtained from other investigations has been duly cited and acknowledged in the thesis.

Shameel T.

Thiruvananthapuram
April 18, 2018

डा. डी रमैया, एफ ए एससी
निदेशक
Dr. D. Ramaiah, F.A.Sc
DIRECTOR

सीएसआईआर- उत्तर पूर्व विज्ञान तथा प्रौद्योगिकी संस्थान
वैज्ञानिक तथा औद्योगिक अनुसंधान परिषद्
जोरहाट-785006, आसाम, भारत

CSIR-NORTH EAST INSTITUTE OF SCIENCE & TECHNOLOGY
COUNCIL OF SCIENTIFIC & INDUSTRIAL RESEARCH (CSIR)
JORHAT-785006, ASSAM, INDIA

April 18, 2018

CERTIFICATE

This is to certify that the work embodied in the thesis entitled: **"Organic Donor-Acceptor Systems for Metal Ion Recognition and OLED Applications"** has been carried out by Mr. Shameel T. under my supervision and guidance at the Photosciences and Photonics Section, Chemical Sciences and Technology Division of the CSIR-National Institute for Interdisciplinary Science and Technology (CSIR-NIIST), Trivandrum and the same has not been submitted elsewhere for a degree.

(D. Ramaiah)

Thesis Supervisor

(*Formerly, Head, Chemical Sciences and Technology Division, CSIR-NIIST, Trivandrum*)

ACKNOWLEDGEMENTS

I have great pleasure in placing on record my deep sense of gratitude to Dr. D. Ramaiah, my thesis supervisor, for suggesting the research problem and for his impeccable guidance, endless support, endearing care and encouragement that led to the successful completion of this work.

I would like to express my sincere thanks to Professor M. V. George for his constant motivation and fruitful discussions during my stay at CSIR-NIIST.

I thank Dr. A. Ajayaghosh, Dr. Suresh Das and Dr. Gangan Pratap, present and former Directors of the CSIR-National Institute for Interdisciplinary Science and Technology (CSIR-NIIST), Thiruvananthapuram, for providing me the necessary facilities for carrying out this work.

I would like to specially mention Dr. K. R. Gopidas and Dr. Joshy Joseph for their valuable advice and discussions for the successful completion of this work. I extend my thanks to Dr. K. Venugopal, Dr. K. Yoosaf and Dr. Biswapriya Deb and scientists of the Photosciences and Photonics Section, Chemical Sciences and Technology Division, for their help and support.

I sincerely acknowledge Dr. Mangalam S. Nair and Dr. R. Luxmi Varma, former and present AcSIR coordinators for their help in successful completion of the course work.

I am very much thankful to Dr. M. L. P. Reddy, Dr. C. Vijayakumar and Dr. P. Binod, my Doctoral Advisory Committee members for their valuable comments and suggestions to improve the quality of my work.

I am indebted to all my group members, particularly, Dr. Lavanya Devi, Dr. K. S. Sanju, Dr. N. Adarsh, Dr. C. K. Suneesh, Dr. B. Hari Shankar, Dr. P. C. Nandajan, Dr. Akhil K. Nair, Dr. M. Betsy, Dr. T. J. Dhanya, Dr. Albish K. Paul, Dr. M. Viji, Dr. Nidhi

Tyagi, Mr. M. Shanmugasundaram, and Mr. R. Aswin for their advice, cordial support and care.

I would like to thank Dr. K. N. Narayanan Unni and Ms. Anjaly Soman for their help in OLED fabrication and Dr. C. H. Suresh and Mrs. Della Theresa for DFT calculations. I also thank Mrs. Saumini Mathew, Mr. Saran and Mr. Gokul for NMR analysis and Mrs. Viji, and Ms. Athira for HRMS data, Mr. Aswin, Mr. Vishnu and Mr. Vibhu Darshan for AFM analysis and Mr. Robert Philip and Mr. Kiran for general help.

I am very much cherished with the true friendship by Mr. T. Thanveer, Mr. M. Sreejith, Mr. Mohammed Yoosuf, Mr. K. V. Sudheesh, Mr. K. C. Naeem, Mr. K. V. Sandeepa, Mr. M. Mathews, Dr. Arun Gopi and Mr. K. Alex and all the present and former members of the Photosciences and Photonics Section and other Divisions of CSIR-NIIST.

Words are inadequate to express my gratitude to my family members who constantly stood as a source of encouragement and confidence. I take this opportunity to pay respect to all my teachers who guided and blessed me.

Finally, I sincerely thank Council of Scientific and Industrial Research (CSIR), UGC, and DST Government of India for financial assistance.

Shameel T.

CONTENTS

PREFACE

Design and development of organic donor-acceptor small molecules for optoelectronic applications is an active area of current research due to their distinct advantages like easy synthesis, excellent purity and tunable band gap. In this regard, the present thesis describes design, synthesis and photophysical properties of few organic donor-acceptor dyads and investigation of their utility as emitters in the organic light emitting diodes and as metal ion sensors. This thesis is organized into four Chapters. The Chapter 1 gives a brief introduction to the organic donor-acceptor molecules and their applications especially in the area of organic light emitting diodes and chemosensors. Recent developments in these fields and major objectives of the current thesis are also highlighted in this chapter.

The second Chapter deals with the design and synthesis of solution processable green emitting organic D-π-A dyads **1** and **2**, combining electron donating phenoxazine and accepting oxadiazole groups and investigation of their photophysical, thermal, electrochemical, morphological and device performance aspects. To understand the intramolecular charge transfer between the donor and acceptor moieties, the position of the phenoxazine moiety at the phenylene linker has been changed from *para*- in the dyad **1** to *meta*- in the dyad **2**. These dyads showed substitution dependent absorption properties and green emission with fluorescence quantum yields of 0.18 and 0.03, respectively in toluene. Similar absorption and emission behaviour was observed in the film state.

Furthermore, the solvent dependent studies have showed negligible changes in the absorption spectra, while a red shift in the emission spectra was observed upon increasing the solvent polarity. Lippert Mataga plot was employed to calculate the changes in the dipole moment between the ground and excited states and these dyads were found to have intramolecular charge transfer (ICT) character in the excited states. Interestingly, these molecules exhibited lower ΔE_{ST} values (< 0.26 eV), which makes them effective for reverse intersystem crossing and delayed fluorescence emitters. The optimised geometries obtained via DFT calculations using B3LYP-6311G functional showed that the HOMO and LUMO were exclusively centred on the donor and acceptor moieties, respectively. Moreover, these systems were found to be thermally stable up to 425 °C. The AFM images of solution processed films revealed smooth and homogeneous film morphologies. The solution processed un-doped OLEDs were fabricated with device configuration having ITO (120 nm)/ PEDOT: PSS (40 nm)/ dyad **1** or **2** (50 nm)/ TPBi (40 nm)/ LiF(1 nm)/ Al (100 nm). The dyads **1** and **2** showed green electroluminescence having λ_{max} at 504 nm and 505 nm with CIE coordinates of (0.26, 0.49) and (0.27, 0.47), respectively. Of these systems, the device based on the dyad **1** exhibited a luminance maximum of *ca.* 1751 cd m^{-2}, demonstrating thereby its potential use in OLED applications.

Among the various luminescent systems, emitters of deep blue electroluminescence with excellent colour purity have great deal of importance as these are one of the important components for fabricating white OLEDs. In this context, design and synthesis of deep blue emitting, solution processable organic D-π-A dyads and investigation of their photophysical, electrochemical, thermal, and

morphological and device performance aspects forms the subject matter of Chapter 3. The designed molecules were incorporated with electron donating carbazole and accepting oxadiazole groups linked through a phenylene linker by *para*- (for the dyad **1**) and *meta*- (for the dyad **2**) substitution. In addition, these unsymmetrical structures with long alkyl chains were adopted to achieve better solubility in organic solvents. We observed a similar trend in the substitution dependent absorption and emission spectra of the dyads **1** and **2** as in the case of phenoxazine derivatives described in the Chapter 2. That is, the absorption band correspond to ICT at 350 nm was found to be suppressed as the position of donor changed from *para*- in the dyad **1** to *meta*- in the dyad **2**. These dyads showed deep blue emission with fluorescence quantum yields of 0.88 and 0.11 in toluene. Upon changing the solvent polarity, we observed a minimal change in the absorption spectra and increased red shift in the emission spectra. The observed large change in the dipole moment between the ground and excited states of these dyads suggest intramolecular charge transfer (ICT) between the donor and acceptor moiety. Furthermore, the fluorescence and delayed fluorescence for these dyads was studied by time resolved fluorescence experiments. Both these dyads were found to be thermally quite stable up to 390 °C and solution processable by forming a homogeneous film. The solution processed un-doped OLEDs based on these dyads **1** and **2**, exhibited deep blue electroluminescence in NUV region having λ_{max} at 410 nm and 408 nm with CIE coordinates of (0.16, 0.07) and (0.16, 0.05), respectively, having high colour purity. The devices based the dyads **1** and **2** showed a maximum luminance of *ca.* 62.17 and 61.45 cd m^{-2}, respectively.

The design and investigation of metal ion recognition aspects of a new colorimetric chemosensor based on diethylaminoquinoline carbaldehyde (**AQC**) forms the subject matter of the Chapter 4 of the thesis. The probe was synthesized in quantitative yields and its sensing behaviour towards various metal ions has been investigated through photophysical, IR and NMR techniques under different conditions. The probe **AQC** was found to selectively interact and detect Cu^{2+} and Hg^{2+} ions from a mixture of transition metal ions with an easy, well defined naked eye visible colour changes from yellow to colourless and pink, respectively. The uniqueness of this system is that it forms stable 1:1 stoichiometric complexes involving diethylamino moiety for the selective recognition of Cu^{2+} ions with a detection limit of 25 ppb. In contrast, it forms a 2:1 stoichiometric complex involving quinoline nitrogen and aldehyde functionality for the selective recognition of Hg^{2+} ions, and showed a detection limit of 360 ppb. The association constants for both Cu^{2+} and Hg^{2+} ions complexes were determined and are found to be *ca.* $2.1 \pm 0.1 \times 10^4$ M^{-1} and $1.29 \pm 0.2 \times 10^8$ M^{-2}, respectively. Uniquely, we have fabricated a simple solid state dipstick device that can be used for the easy visual detection of Cu^{2+} and Hg^{2+} ions in the aqueous medium, demonstrating thereby its effective use for the heavy metal ion analysis in water.

***Note**: The numbers of various compounds given here correspond to those given under the respective chapters.*

Sl. No	List of Figures	Page
1.	Figure 1.1	2
2.	Figure 1.2	4
3.	Figure 1.3	5
4.	Figure 1.4	7
5.	Figure 1.5	8
6.	Figure 1.6	15
7.	Figure 1.7	17
8.	Figure 1.8	19
9.	Figure 1.9	21
10.	Figure 1.10	24
11.	Figure 1.11	24
12.	Figure 1.12	26
13.	Figure 1.13	26
14.	Figure 1.14	29
15.	Figure 1.15	31
16.	Figure 2.1	46
17.	Figure 2.2	47
18.	Figure 2.3	48
19.	Figure 2.4	50
20.	Figure 2.5	50
21.	Figure 2.6	54
22.	Figure 2.7	54
23.	Figure 2.8	55
24.	Figure 2.9	56
25.	Figure 2.10	56
26.	Figure 2.11	57
27.	Figure 2.12	57
28.	Figure 2.13	59

List of Tables

List of Schemes

List of Charts

List of Abbreviations

1. A – Ampere
2. Å - Angstrom
3. Ag – Silver
4. Al – Aluminum
5. AFM- Atomic force microscopy
6. B3LYP – Becke, three-parameter, Lee-Yang-Parr
7. ^{o}C – Degree Celsius
8. CIE – Commission Internationale de L'Eclairage
9. Cd – Candela
10. cm – Centimeter
11. *ca.* – *circa*
12. Ca – Calcium
13. Co – Cobalt
14. Cd – Cadmium
15. CV – Cyclic voltammetry
16. CE – Current efficiency
17. CT – Charge transfer
18. $CDCl_3$ – Deuterated chloroform
19. CH_3CN – Acetonitrile
20. Calcd. – Calculated
21. Cu – Copper
22. Cl^- – Chloride

23. ClO_4^- – Perchlorate
24. $CH3COO^-$ – Acetate
25. D-A – Donor-Acceptor
26. DCM – Dichloromethane
27. DFT – Density functional theory
28. ΔE_{ST} – Energy gap between the S_1 and T_1 state
29. *et al.* – *Et allii/alia*
30. ε – Molar extinction coefficient
31. E_{gap} – Energy gap (band gap)
32. E_{HOMO} – Energy of HOMO
33. E_{LUMO} – Energy of LUMO
34. E_s – Singlet energy
35. E_T – Triplet energy
36. ESI-MS – Electrospray ionoisation mass spectrometry
37. EDTA – Ethylenediaminetetraacetic acid
38. EQE – External quantum efficiency
39. EL – Electroluminescence
40. EML – Emissive layer
41. ETL – Electron transporting layer
42. EIL – Electron injection layer
43. eV – Electron volt
44. FAB-MS – Fast atom bombardment mass spectrometry
45. FT-IR – Fourier transform infrared

46. g - Gram

47. h – Hour

48. HOMO – Highest occupied molecular orbital

49. Hg – Mercury

50. HCl – Hydrochloric acid

51. HIL – Hole injection layer

52. HTL – Hole transporting layer

53. ICT – Intramolecular charge transfer

54. ISC – Intersystem crossing

55. IR – Infrared

56. ITO – Indium tin oxide

57. J – Current density

58. K – Kelvin

59. k_r – Radiative rate constant

60. k_{nr} – Non-radiative rate constant

61. LED – Light emitting diode

62. LCD – Liquid crystal display

63. LUMO – Lowest unoccupied molecular orbital

64. L – Lumens

65. LiF – Lithium fluoride

66. λ_{max} – Wavelength maximum

67. LOD – Limit of detection

68. LMCT– Ligand to metal charge transfer

69. M – Molar

70. mg – Milligram

71. mL – Millilitre

72. µM – Micromolar

73. µs – Microseconds

74. µm – Micrometer

75. mM – Millimolar

76. mmol – Millimole

77. mp – Melting point

78. Mg – Magnesium

79. Mn – Manganese

80. MALDI-TOF-MS – Matrix-assisted laser desorption ionization-time of flight- mass spectrometry

81. NTSC - National television standards committee

82. Na – Sodium

83. Ni – Nickel

84. nm – Nanometer

85. NMR – Nuclear magnetic resonance

86. ns – Nanosecond

87. υ_{max} – Frequency maximum

88. vs – Versus

89. OLED – Organic light emitting diode

90. Pb – Lead

91. PL – Photoluminescence

92. PLQY – Photoluminescence quantum yield

93. PE – Power efficiency

94. ppb – Parts per billion

95. ppm – Parts per million

96. Φ_F – Quantum yields of fluorescence

97. RT – Room temperature

98. RISC – Reverse intersystem crossing

99. s – Seconds

100. S_1-Lowest singlet excited state

101. TLC – Thin layer chromatography

102. TGA – Thermogravimetric analysis

103. T_1 – Lowest triplet excited state

104. T_d –Decomposition temperature

105. THF – Tetrahydrofuran

106. TADF – Thermally activated delayed fluorescence

107. TMS – Tetramethylsilane

108. τ_f– Fluorescence lifetime

109. TPBi – 1,3,5-Tris(N-phenylbenzimidazol-2-yl)benzene

110. UV – Ultraviolet

111. Vis – Visible

112. W – Watt

113. Zn – Zinc

Chapter 1

Organic Donor-Acceptor Systems for Optoelectronic Applications: An Overview

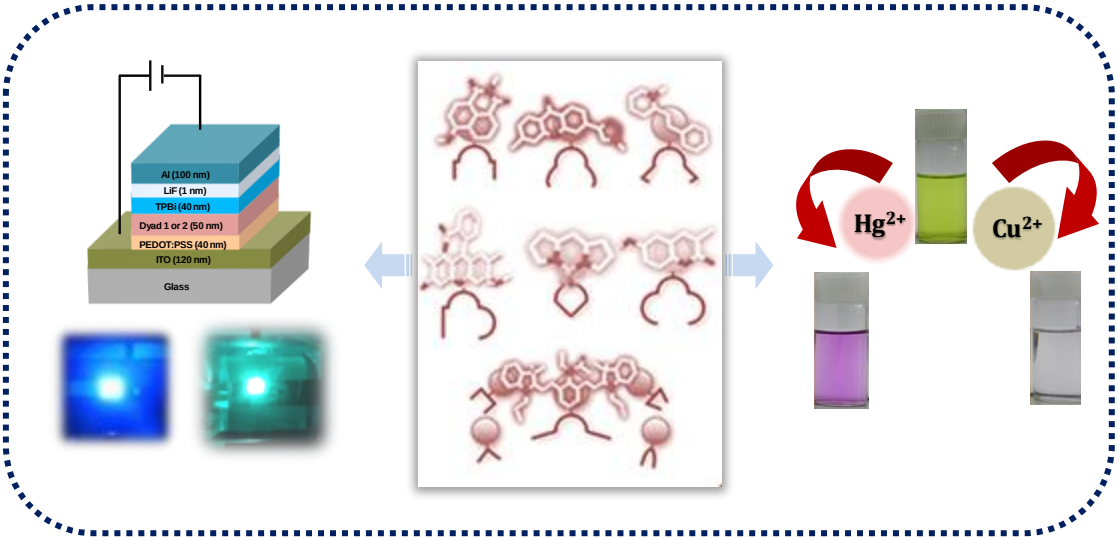

1.1. Introduction

The organic donor-acceptor systems are of great interest due to their significant advantages like easy synthesis, high purity and tunable band gap energy over their polymer and inorganic analogues.[1] Understanding the structure-property relationship of these molecules has great importance as this would help us to develop new and simple organic molecules with multifunctional properties. The optical, electrochemical and electronic properties of such organic donor-acceptor systems can be fine-tuned by various structural modifications and functionalizations.[2] In these molecules, due to the D–A interaction, a new low energy molecular orbital of intramolecular charge transfer

(ICT) state is possible and the electrons in this state can be easily excited using visible light. The ICT causes the polarization of the D-π-A structure and generation of a large molecular dipole. The ICT characteristics of donor-acceptor small molecules can be demonstrated by the UV/Vis absorption spectra of aniline, nitrobenzene, 4-nitroaniline and 3-nitroaniline (Figure 1.1).[3] Aniline and nitrobenzene show absorption only in the UV region, whereas 4-nitroaniline shows intense and bathochromically shifted absorption maxima, which is assigned to ICT-band. In contrast, 3-nitroaniline exhibits only a diminished CT-band as a result of a non-conjugating arrangement of the amino donor and the nitro acceptor groups. In other words, due to the *meta*-substitution of electron withdrawing nitro group, the ICT has been suppressed in 3-nitroanline.

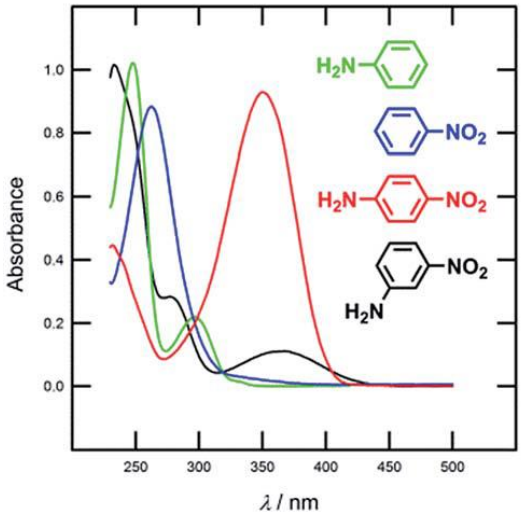

Figure 1.1. UV/Vis spectra of D–π–A systems based on aniline and nitroaniline. Reproduced with permission from Reference 3 and RSC Copyright 2014.

In general, the optoelectronic properties of a D-A system can be tuned either through the donor unit, acceptor unit or π-spacer which connect the donor and acceptor units in the molecules.[4] The widely used electron donor moieties have

functional groups possessing +M effect such as N,N-dialkylamino groups (-NR_2), alkoxy groups (-OR) or electron rich heterocyclic moieties such as thiophene, carbazoles, phenoxazines etc. The optoelectronic properties can be modified through donor units by i) introducing a stronger or weaker donor group; ii) addition of one or more donors; and iii) changing the position of donor unit across the acceptor unit in a conjugating or non-conjugating arrangement.[5] The π-conjugated bridge between the electron donor and acceptor moieties can be a combination of multiple bonds, aromatic or heteroaromatic groups. It was found that the incorporation of a heterocyclic moiety into the system provides significant advantages of higher chemical and thermal stability, acid–base and chelating properties, non-centrosymmetry etc.[6] On the other hand, the most used electron acceptors involve substituents featuring –M effects such as -NO_2, -CN and -CHO or electron deficient heterocyclic compounds such as, benzothiazole, oxadiazoles, quinoxalines, imidazoles etc. In this context, numerous studies have been carried out on the donor-acceptor molecules in recent years to understand the effect of donor, acceptor groups as well as π-linkage.[7] In this thesis, we have particularly focused on the strength and position of the donor moieties to develop novel multifunctional molecules.

The organic D-A systems have been extensively explored for many potential applications including organic light emitting diodes,[8] biological labeling,[9] photodynamic therapy,[10] photosensitizers,[11] nonlinear optics,[12] chemosensors,[13] photocatalysts,[14] for organic synthesis,[15] singlet oxygen sensitizers,[16] and dye sensitized solar cells[17] (Figure 1.2). In this chapter, we primarily focused on applications of such organic donor-acceptor systems in OLEDs and as metal ion probes.

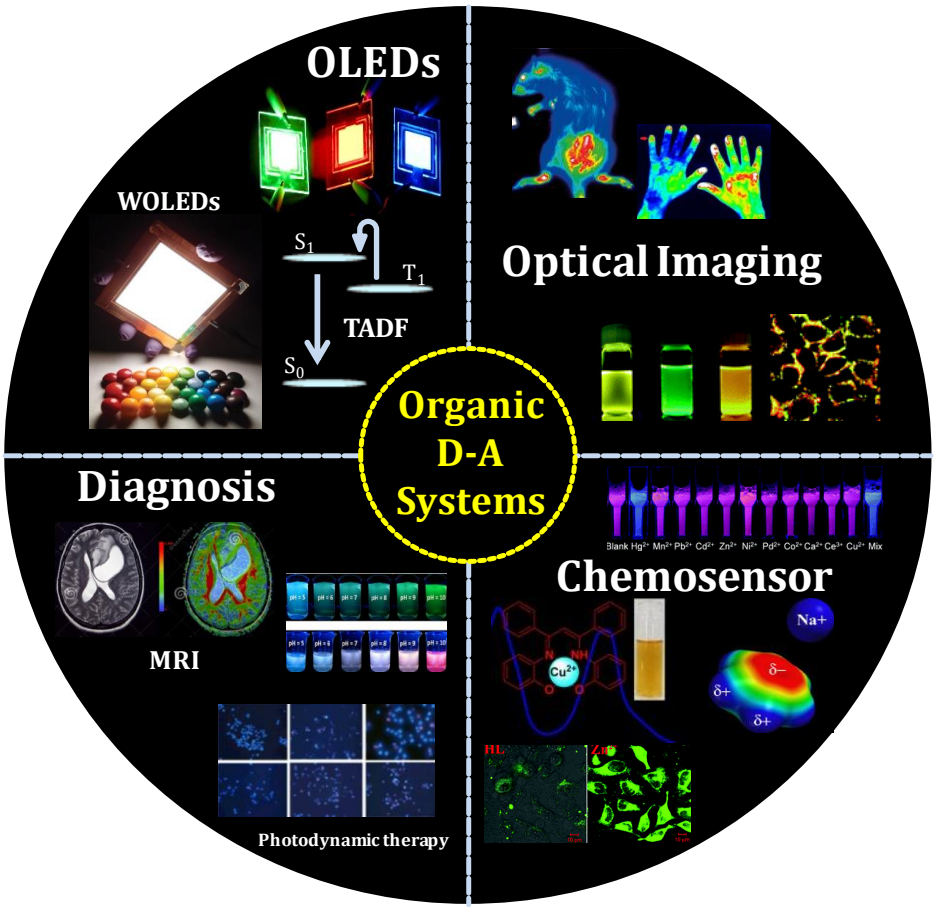

Figure 1.2. Applications of the organic D-π-A systems inspired from the attractive photophysical properties.

1.2. Organic Light Emitting Diodes (OLEDs)

The organic light emitting diodes (OLEDs) in which an organic emissive film is sandwiched between a cathode and a transparent anode, which emits light in response to an electric current. The structure of most common OLEDs consist of five functional layers including hole injection layer (HIL), hole transporting layer (HTL), emission layer (EML), electron transporting layer (ETL), and electron injection layer (EIL). Up on electrical excitation, the electrons move from the cathode and holes move from the anode. At the emissive layer, an exciton is generated and the recombination of electron-

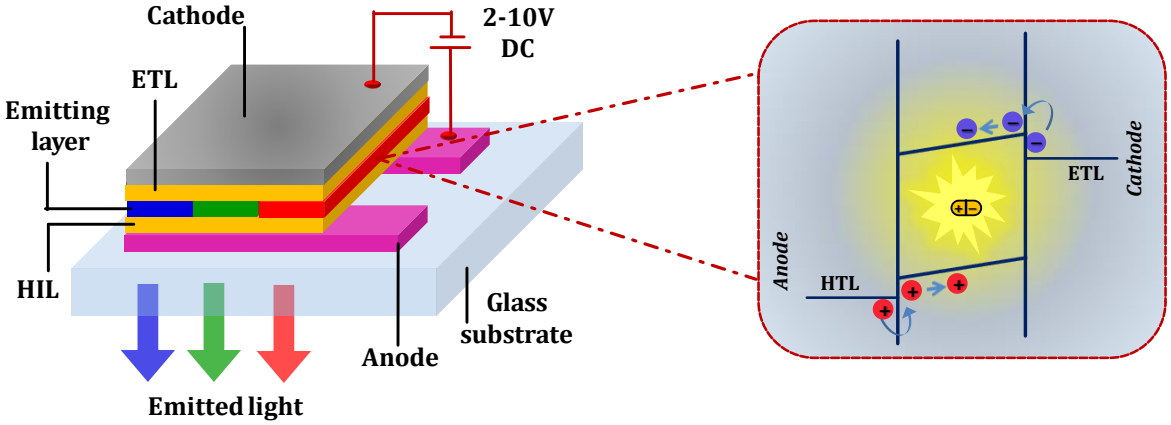

Figure 1.3. Basic structure and working principle of a typical OLED system.

hole pair produces emission corresponds to the energy gap of the material (Figure 1.3).[18] OLEDs of various emission colors are possible with emitters of suitable band gap. This area of research has been started by the pioneering work of Tang and co-workers,[19] in which they have developed a multilayer OLEDs using AlQ_3 as an emitter. After that, a wide range of materials have been developed and these efforts are still continuing to get efficient, cost effective and solution processable emitters with excellent color purity.[20]

OLEDs provide a wide variety of possibilities for making them superior to liquid crystal displays (LCDs), inorganic LEDs and fluorescent tubes. OLED displays do not require a backlight and so they are extremely thin (<400 nm) and compatible with any simple substrates. Their solution processability makes them easy to fabricate and reducing the cost of devices. The devices with a variety of colors and functionality are possible as one can easily tune the properties of the organic materials by changing the functional groups. Compared to LCDs, OLED displays provide improved image quality like better contrast, higher brightness, wider viewing angle (>160˚), a fast response

time (μs and less) and lower power consumption (2-10 V). They can also be made transparent, flexible and foldable. This creates many possibilities for innovative and distinct applications such as e-papers, wearable devices, transparent windows or car windshields etc. In spite of many advantages, there are still a few drawbacks limiting OLEDs mass production. The disadvantages of OLEDs are mainly related to their stability and lifetime. The organic materials can easily be damaged by the presence of UV light, oxygen and humidity. Since high band gap materials usually degrade faster, the blue OLED pixels have a very different life span from the green and red pixels. Extensive efforts in encapsulation techniques, device structures and material synthesis are still needed to extend the lifetime of the device based on such systems.

1.3. Classification of Organic Emitters

The organic small molecules based luminescent materials are categorized as the conventional fluorescent materials and phosphorescent materials. The fluorescent materials are generally known as first generation materials, which can harvest only the singlet excitons (25%), generated by electrical excitation (Figure 1.4). For real practical applications, these materials are limited by their low efficiency in device performance. On the other hand, the organo-transition metal complexes known as phosphorescent materials can harvest both singlet and the more populated triplet excitons (75%), which could attribute their high external quantum efficiencies (EQEs).[21] The efficiencies of phosphorescent OLEDs are found to be four times higher than that of the conventional fluorescent OLEDs. However, phosphorescent OLEDs containing transition metal based compounds are rather expensive and unsustainable because

they are made of rare metals like Ir or Pt, which limit their commercial applications.[22] While OLEDs containing Cu (I) complexes that exhibit high EQE comparable to those with transition metal complexes have been demonstrated as an alternative, but possess relatively low reliability and high driving voltage.[23] Therefore, both conventional fluorescence and phosphorescence based OLEDs have many disadvantages when compared to their advantages.

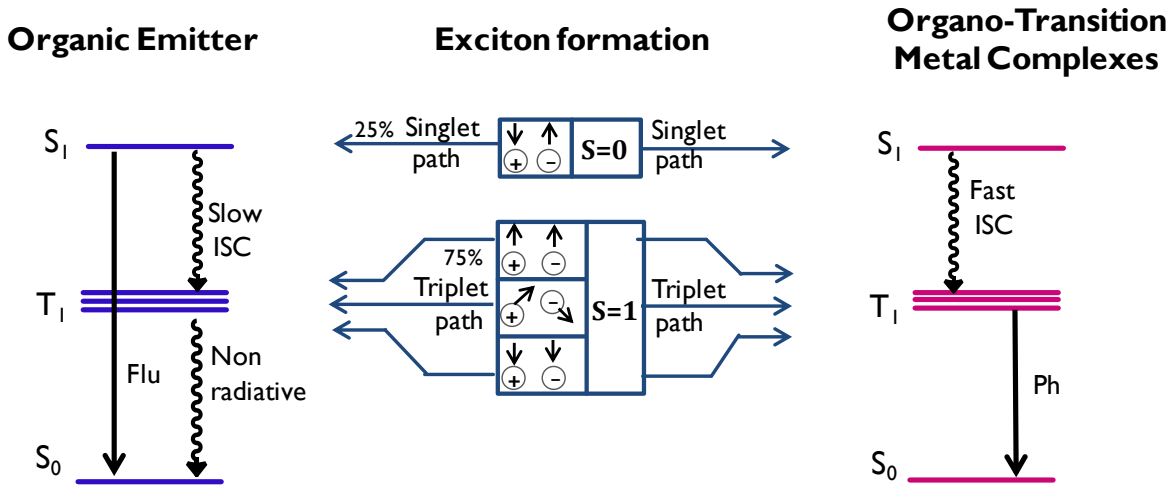

Figure 1.4. Jablonski diagram showing the ground and excited state properties of fluorescent and phosphorescent emitters.

Recently, Adachi and co-workers developed a third generation material, which can harvest both singlet and triplet exciton by thermally activated delayed fluorescence (TADF) mechanism.[24] In TADF, the lowest triplet excited states (T_1), which are normally non-emissive, are converted to the emissive lowest singlet excited states (S_1), via an intersystem crossing (ISC) by thermal activation. A small energy difference between S_1 and T_1 states (ΔE_{ST}) is needed to realize efficient TADF. A small ΔE_{ST} value means that there is a small overlap integral between the wave functions of the ground and excited

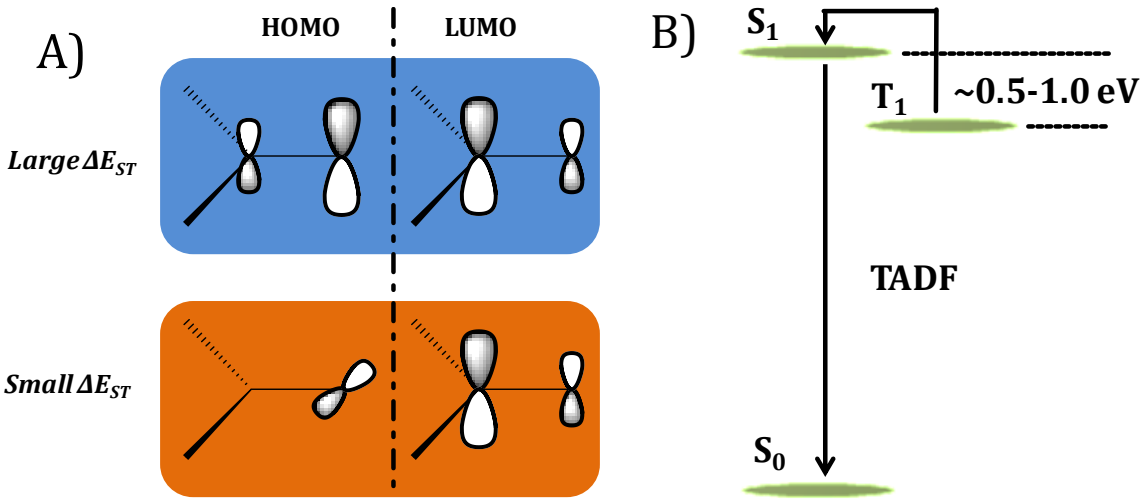

Figure 1.5. (A) Pictorial representation of the strategy for realizing small ΔE_{ST} in organic molecules for TADF. (B) Modified Jablonski diagram for a molecule exhibiting TADF property.

states of a luminescent molecule and thus, minimizing the electron–electron repulsion between the orbitals in the triplet state [Figure 1.5]. The overlap between the wave functions can be effectively minimized in D-π-A molecules by localizing the electron densities of the HOMO and LUMO on donor and acceptor moieties, respectively. An additional steric separation between the acceptor and donor units helps to localize the electron densities and that can be effectively achieved by introducing a spiro junction or bulky substituent between the acceptor and donor units.

1.4. Donor-Acceptor Type Emitters for OLEDs

In general, TADF molecules have donor-acceptor structure with a large steric hindrance or twisted structure between the donor and acceptor units. Different kinds of donor and acceptor groups have been used to develop donor–acceptor type TADF molecules. The aromatic amines of carbazole,

diphenylamine, phenoxazine, phenothiazine, 9,9-dimethyl-9,10-dihydroacridine, 5-phenyl-5,10-dihydrophenazine, 5,10-dihydrophenazine and their derivatives were widely used as donor groups due to their stability, strong electron donating ability as well as high triplet states. On the other hand, various types of acceptors were used in these donor-acceptor molecules to tune their emission color, excited state lifetimes and fluorescence quantum yields. A discussion on the major properties of donor–acceptor combinations based on the acceptor units is discussed below since this thesis focused mainly on such systems for OLEDs.

1.4.1. Cyano substituted acceptors

Due to the strong electron withdrawing character, the cyano group has been widely employed to construct strong acceptors in the D-A structures with intramolecular charge transfer properties. Adachi and co-workers have developed a series of highly efficient TADF emitters using carbazole as a donor and dicyanobenzene as an electron acceptor (Chart 1.1).[25] High photoluminescence (PL) efficiency and various emission colours were achieved by changing the number and the relative position of the donor and acceptor units in these emitters. It was found that, the cyano group suppresses both non-radiative deactivation and changes in the geometries of the S_1 and T_1 states of these molecules, leading to high quantum efficiency. The authors have achieved molecule **3** with green emission (507 nm), **6** with orange emission (577 nm) and **1** with sky blue emission (470 nm). Moreover, the HOMOs and LUMOs of these emitters were localized on the donor and acceptor moieties, respectively, and

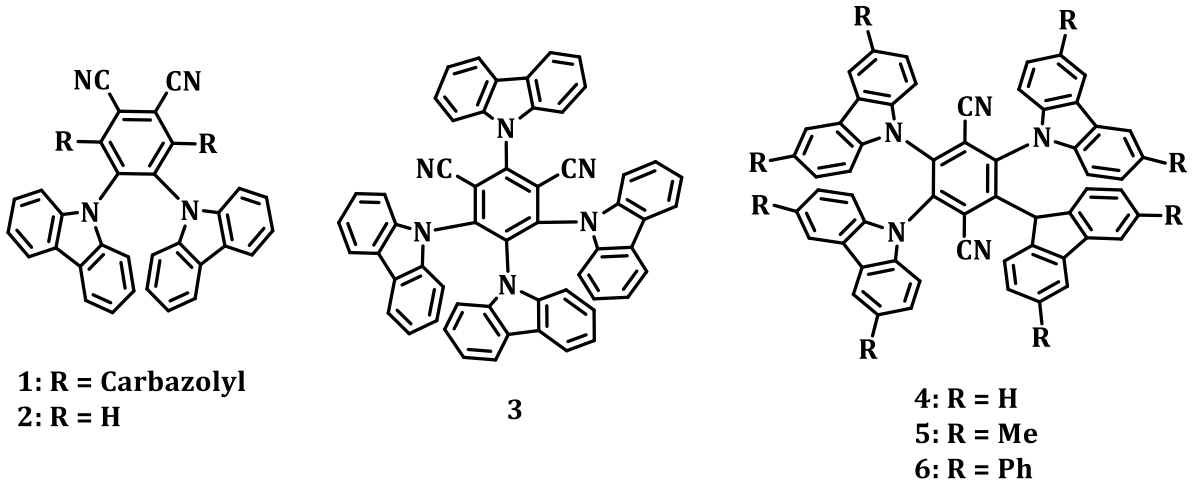

Chart 1.1. Molecular structures of D-A systems **1-6**, Me-methyl; Ph-Phenyl.

thus small values of ΔE_{ST} were achieved. The carbazolyl units in these dyads were twisted from the plane of dicyanobenzene due to steric hindrance. The multilayer green OLEDx using emitter **3** in 4,4'-bis(carbazol-9-yl)biphenyl (CBP) a host resulted in high EQE of 19.3 ± 1.5%. In addition, the sky blue device in 2,8-bis(diphenylphosphoryl)dibenzo[b,d]thiophene (PPT) and orange device in CBP demonstrated EQEs of 8.0 ± 1% and 11.2 ± 1%, respectively.

1.4.2. Triazine substituted acceptors

The triazine group has three potential modification sites and is highly electron deficient moiety. The aromatic amine–triazine hybrids composed of electron donating aromatic amine and electron accepting triazine units are widely reported for OLEDs.[26] These types of materials show excellent thermal, morphological, optical and electrical properties. Among the various reported molecules, Kaji and co-workers presented a molecular design strategy to achieve a small ΔE_{ST} by utilizing *meta*- linking between the

donor and acceptor moieties (Chart 1.2).[27] The electron donating carbazolyl groups were substituted on to an electron accepting triphenyltriazine unit through *meta*- (in molecule **7**) and *para*- (in molecule **8**) linkage. The *meta*-substituted compound **7** exhibited a lower ΔE_{ST} compared to the *para*-substituted compound **8** due to the poor overlap between HOMO and LUMO orbitals. Therefore, by simply changing the linkage position between electron-donating and electron-accepting moieties, the ΔE_{ST} of fluorescent molecules can be reduced without further chemical modification. Further, the *meta*- linking strategy was explored to develop various emitters.[28]

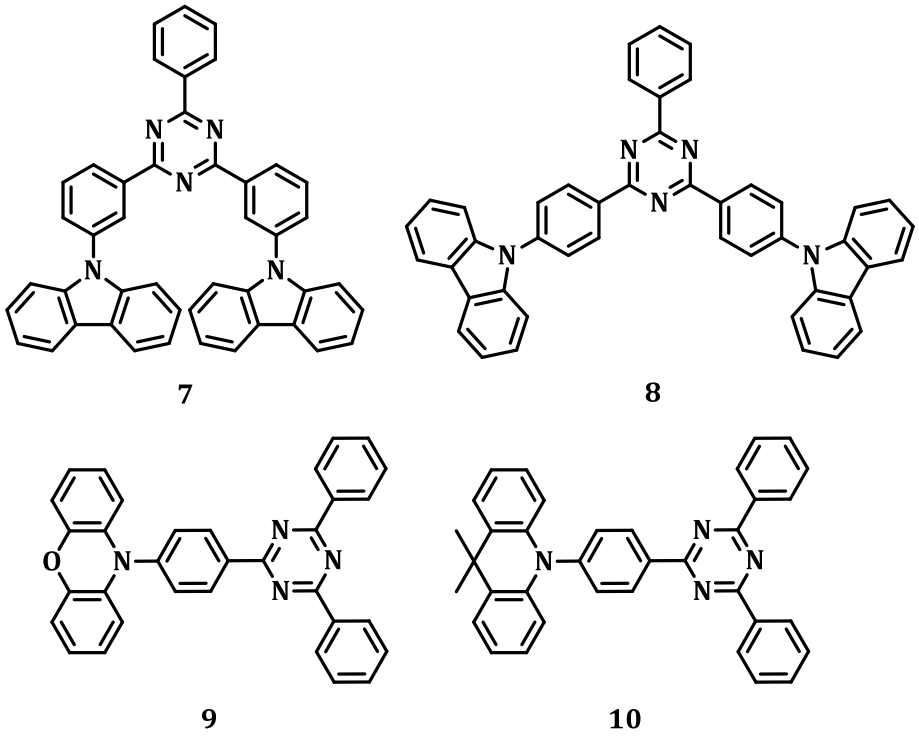

Chart 1.2. Molecular structures of the D-A systems **7-10** reported.

Adachi and co-workers introduced a twisted configuration into the molecule by selecting phenoxazine instead of carbazole as the donor unit.[29] The phenoxazine unit has a morpholine like six membered ring and which causes steric repulsion towards

any neighboring substituent. Moreover, the intramolecular charge transfer properties these systems can be tuned by a relatively strong donor phenoxazine instead of a weak donor carbazole. In the case of **9**, the phenoxazine unit provides a unique molecular geometry to achieve an effective separation of HOMO and LUMO levels and induces the charge transfer transition. The oxygen atom of phenoxazine localizes the electron density distribution of the HOMO onto the donor unit. For the reason that the overlap between HOMO and LUMO was small, the exchange interaction between two electrons in HOMO and LUMO was effectively less, and as a result ΔE_{ST} is quite small and calculated to be 0.070 eV for the dyad **9**. The fabricated multilayer OLED using the emitter **9** as the emissive layer exhibited an EQE of *ca.* 12.5% with green emission.

Wu and co-workers[30] have reported another system **10**, which was derived from the dyad **9**, in which the phenoxazine donor is replaced with the 9,9-dimethyl-9,10-dihydroacridine unit (Chart 1.2). The system **10** showed excellent luminescence characteristics both in a host and un-doped films. At room temperature, the dyad **10** doped with 9-(3-(9H-carbazol-9-yl)phenyl)-9H-carbazole-3-(carbonitrile) (mCPCN) exhibited a high PLQY of *ca.* ~90%, higher than that of **9** (*ca.* 66%). The compound **10** as an emissive layer achieved high EQEs of up to *ca.* 26.5% in a device using a host and *ca.* 20% for an un-doped device.

1.4.3. Diphenyl sulfoxide substituted acceptors

As the oxygen atoms of the sulfonyl group are highly electronegative, this group has significant electron withdrawing properties and thus the diphenyl sulfoxide has been exploited as an effective accepter moiety. In addition, the sulfonyl group of

diphenyl sulfoxide has a tetrahedral geometry and which limits the conjugation of the molecules. Adachi and co-workers have synthesized a deep blue emitter **11** (Chart 1.3), which is based on diphenyl sulfoxide as the acceptor and carbazole as the donor group.[31] The tert-butyl groups on the donor unit were introduced to enhance the electron donating ability. The PLQY of the compound in the host, bis[2-(diphenylphosphino)phenyl]ether oxide (DPEPO) film was found to be 0.80 (λ_{max}, 423 nm). Using the doped DPEPO films as the emitting layers, a multilayer device was fabricated and achieved an EQE of *ca.* 9.9%. The CIE coordinates for the EL of the device were (0.15, 0.07), which were very close to those of the National Television Standards Committee (NTSC) standard blue values of 0.14, 0.08. In another report, Sun and co-workers have studied the impact of the change in the position of 3,6-di-tert-butylcarbazole units by fixing the position central diphenyl sulfone backbone in the

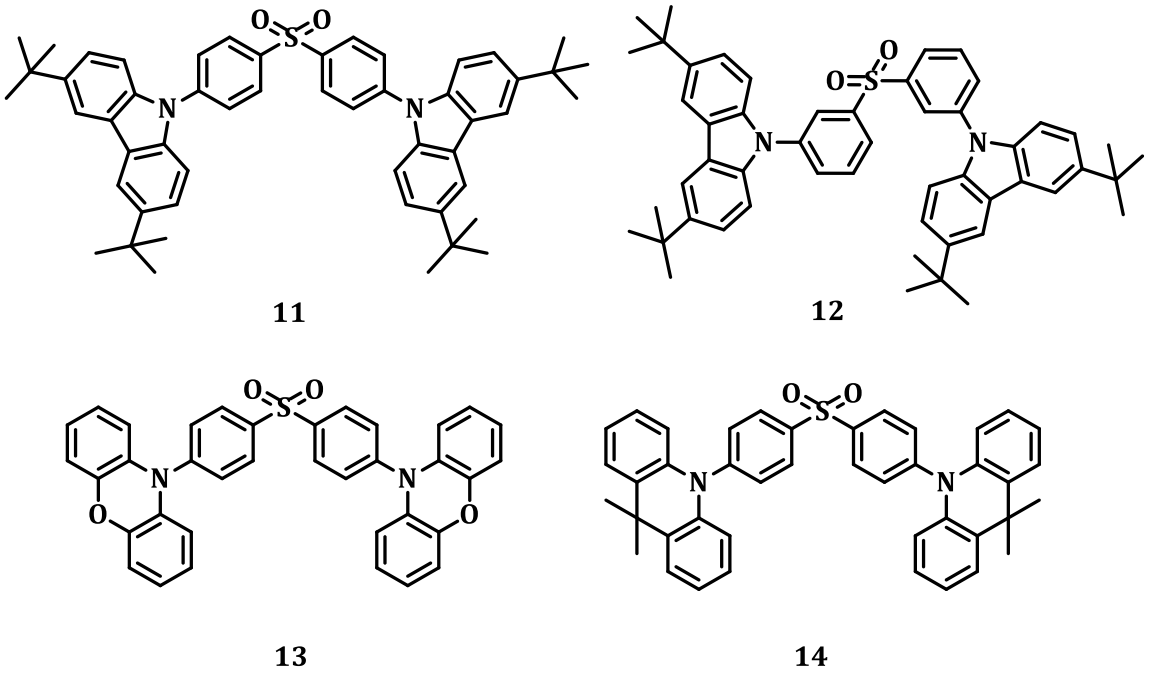

11 **12**

13 **14**

Chart 1.3. Molecular structures of D-A systems **11-14** based on diphenyl sulfoxide.

emitter **11** (Chart 1.3). When 3,6-di-tert-butylcarbazole is linked at the *meta* position, the energy gap between the singlet and triplet states of **12** was reduced and as a result the TADF properties were enhanced.[32]

Further, Adachi and co-workers have reported diphenyl sulfone derivatives containing different donor units in order to understand the effect of donor units.[33] The dyads **13** and **14** combine phenoxazine and 9,9-dimethyl-9,10-dihydroacridine instead of carbazole donor units. In oxygen-free toluene solution at room temperature, the PLQYs of these two compounds were found be *ca.* ~80%. The singlet-triplet energy gaps were reduced to almost 0.08 eV for these two derivatives. The devices using the dyads **13** and **14** achieved the highest EQEs of *ca.*17.5% ca. 19.5%, respectively.

1.4.4. Thianthrenetetraoxide substituted acceptors

Su and co-workers have introduced a new acceptor unit, thianthrene-9,9',10,10'-tetraoxide, which was derived from the diphenyl sulfone group. In this context, two emitters **15** and **16** were synthesized using the new acceptor unit along with 9,9-dimethyl-9,10 dihydroacridine and phenoxazine as the electron donor units.[34] The HOMOs were mainly located on the donor moieties due to their strong electron donating properties. Because of the strong electron withdrawing ability of the acceptor unit and the extended π-conjugation, the LUMOs were dispersed over the phenyl bridge and the acceptor unit. From the fluorescence and phosphorescence spectra, ΔE_{ST} of **15** and **16** were estimated to be 0.058 and 0.048 eV, respectively. The devices based on these systems **15** and **16** co-deposited with CBP at a concentration of *ca.* 6 wt% as EML showed quite low turn-on voltages of 3.5 V and 3.7 V, indicating efficient charge-

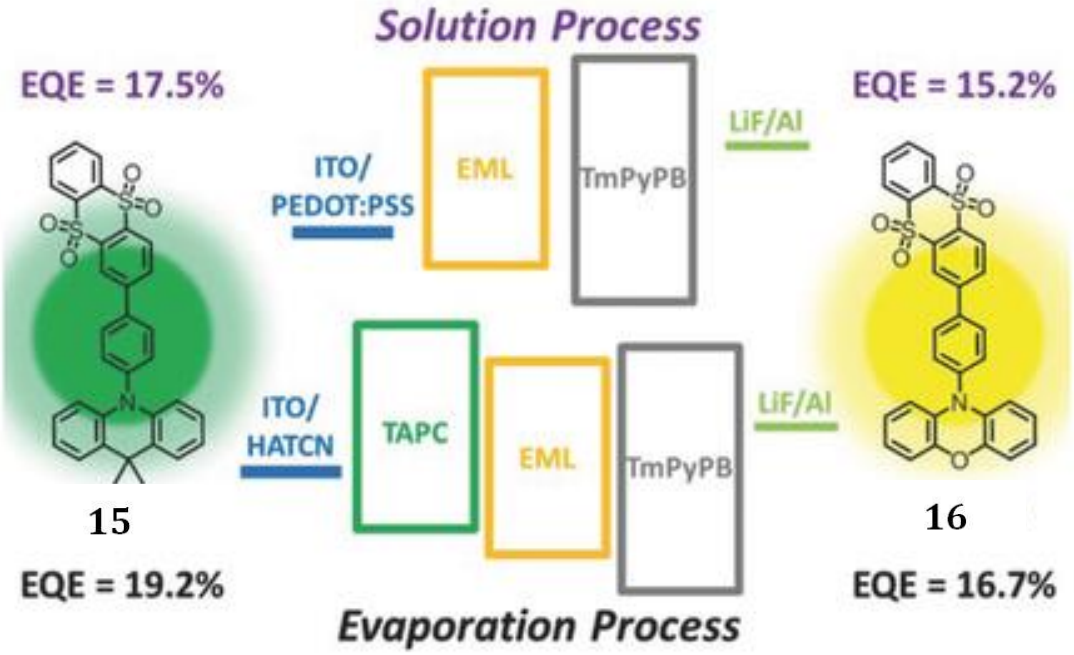

Figure 1.6. Chemical structures of **15** and **16** with their OLED structures, EQE for evaporation and solution processable OLEDs. Reproduced with permission from Reference 34. Copyright 2015 John Wiley & Sons.

carrier injection and transport into EML in such a device structure. The device based on **15** emitted green light with a maximal current efficiency (CE) of 61.8 cd A^{-1}, power efficiency (PE) of 54 lm W^{-1}, and an EQE of *ca.* 19.2%. In addition, the device based on **16** exhibited an yellow emission with a maxial CE of 49.3 cd A^{-1}, a PE of 38.5 lm W^{-1}, an EQE of *ca.* 16.7%, and maximum luminance over 17000 cd m^{-2}. Similar to the evaporation processed devices, remarkable EQE values of *ca.* 17.5% and *ca.* 15.2% were achieved for the solution processed devices based on **15** and **16**, respectively (Figure 1.6). The observed higher efficiencies of the devices indicate that a balanced charge carrier recombination could also be achieved without any hole transport layer.

1.4.5. Oxadiazole substituted acceptors

The electron accepting 1,3,4-oxadiazole moieties have been widely used as building blocks for electron transporting materials in OLEDs. Adachi and co-workers[35] have developed highly efficient emitters **17** and **18** containing 2,5-diphenyl-1,3,4-oxadiazole acceptor and phenoxazine donor units (Chart 1.4). In oxygen free toluene solution, the D–A–D-type molecule **18** showed a higher PLQY of *ca.* 43.1% than that of the D–A type molecule **17** (*ca.* 29.8%) due to its small ΔE_{ST} value. Up on nitrogen bubbling, the PLQY of the molecules **17** and **18** was increased from *ca.* 19.9% to 43.1% and *ca.* 18.1% to 29.8%, respectively. The larger increase in the PLQY for **18** compared to **17** shows that the former exhibits a more effective T_1 to S_1 up-conversion than the latter. The OLED device with 6 wt% **18:** DPEPO as EML showed a green electroluminescence with an EQE of *ca.* 14.9%. Further, Adachi and co-workers have extended their studies to the device performance of the corresponding molecules using the acceptor moieties triazole and diazole with sulfur atom instead of oxygen. The fabricated devices based on these derivatives showed lower efficiencies compared to the oxadiazole derivatives.[36]

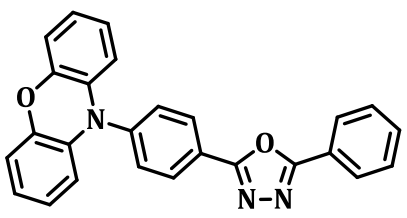

17

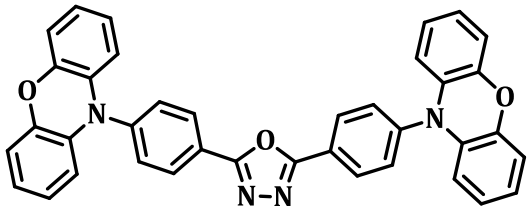

18

Chart 1.4. Molecular structures of D-A systems **17** and **18** based on oxadiazole unit.

1.4.6. Phenoxaphosphine oxide and phenoxathiin dioxide substituted acceptors

Yasuda and co-workers have reported two efficient blue emitters, **19** and **20** (Figure 1.7), made of phenoxaphosphine oxide and phenoxathiin dioxide acceptor units, respectively.[37] Because of the strong electron withdrawing characteristics of the phosphine oxide and sulfone groups, the LUMO values of **19** and **20** were localized on the phenoxaphosphine oxide and phenoxathiin dioxide acceptor moieties, respectively. On the other hand, the HOMOs of both the molecules were distributed mainly on the 9,9-dimethyl-9,10-dihydroacridine donor moiety. Owing to the well separated molecular orbitals, small ΔE_{ST} values of 0.02 and 0.10 eV were observed for **18** and **19**,

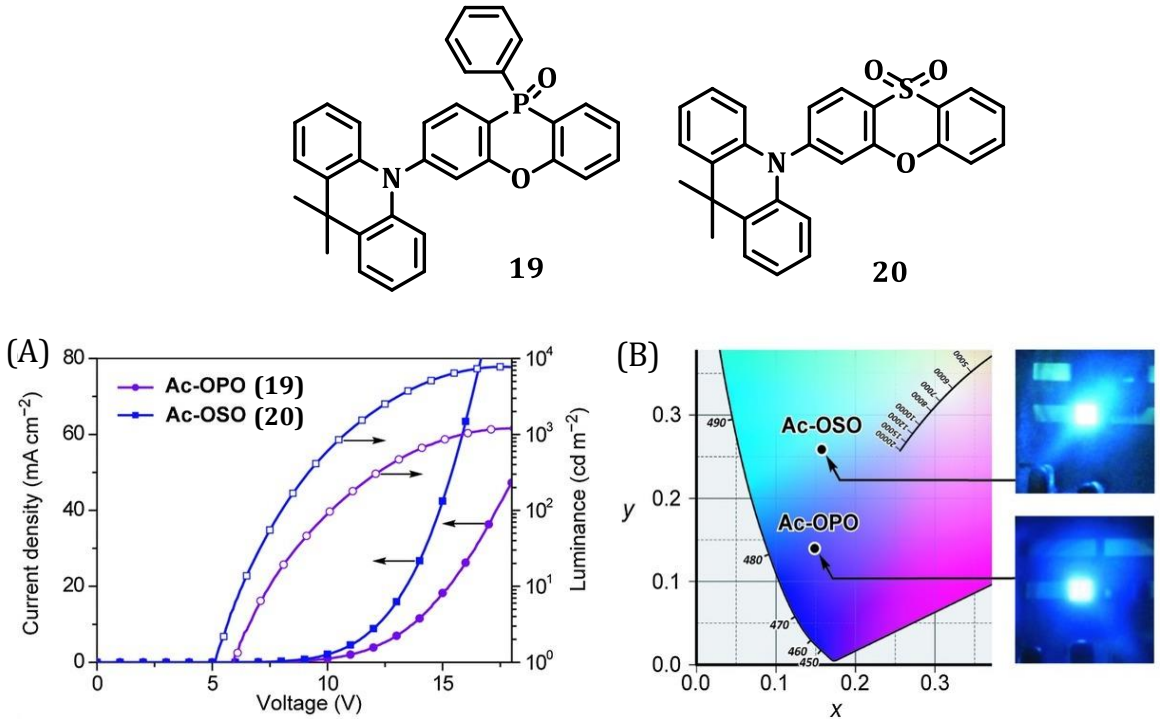

Figure 1.7. Molecular structures and device characteristics of emitters **19** and **20.** Reproduced with permission from Reference 37. Copyright © 2016, John Wiley and Sons.

respectively. It was also found that the calculated HOMOs and LUMOs of the molecules were weakly overlapped on the phenyl ring of the acceptor moiety, which results an enhancement in the radiative decay and efficient light emission. The doped films of **18** and **19** in DPEPO showed excellent PLQYs of *ca.* 62% ± 2% and *ca.* 98% ± 2%, respectively. The estimated ΔE_{ST} values from the onsets of the fluorescence (300 K) and low temperature phosphorescence (5 K) spectra of **18** and **19** were found to be 0.03 and 0.06 eV, which are quite favorable for efficient reverse intersystem crossing. The fabricated OLEDs showed blue emission with maximum EQE value of *ca.* 12.3% for **18** and *ca.* 20.5% for **19**, with color coordinates of (0.15, 0.14) and (0.16, 0.26), respectively.

1.4.7. Triarylboron substituted acceptors

The triarylboron compounds were strong electron acceptors due to the presence of a vacant p-orbital on the central boron atom. The donor-acceptor dyads combining triarylboron acceptor and aromatic amine based donor groups have received immense attention owing to their strong intramolecular charge transfer properties.[38] Shuichi Oi and co-workers have developed two new donor-acceptor triarylboranes exhibiting TADF characteristics.[39] The electron accepting dimesitylphenylborane unit used as the acceptor and 9,9-dimethylacridane (**21**) and phenoxazine (**22**) as the donor units. These dyads **21** and **22** exhibited blue and green TADF with good photoluminescence quantum yields of *ca.* 89 and 87% in toluene, respectively. These compounds showed a well separated HOMO and LUMO between the donor and accepter moieties due to the large dihedral angles

between phenylene linkage and donor units (Figure 1.8). Resultantly, a small energy gap between the S_1 and T_1 state and reverse intersystem crossing of excitons was observed. OLEDs using the compounds **21** and **22** as emitters

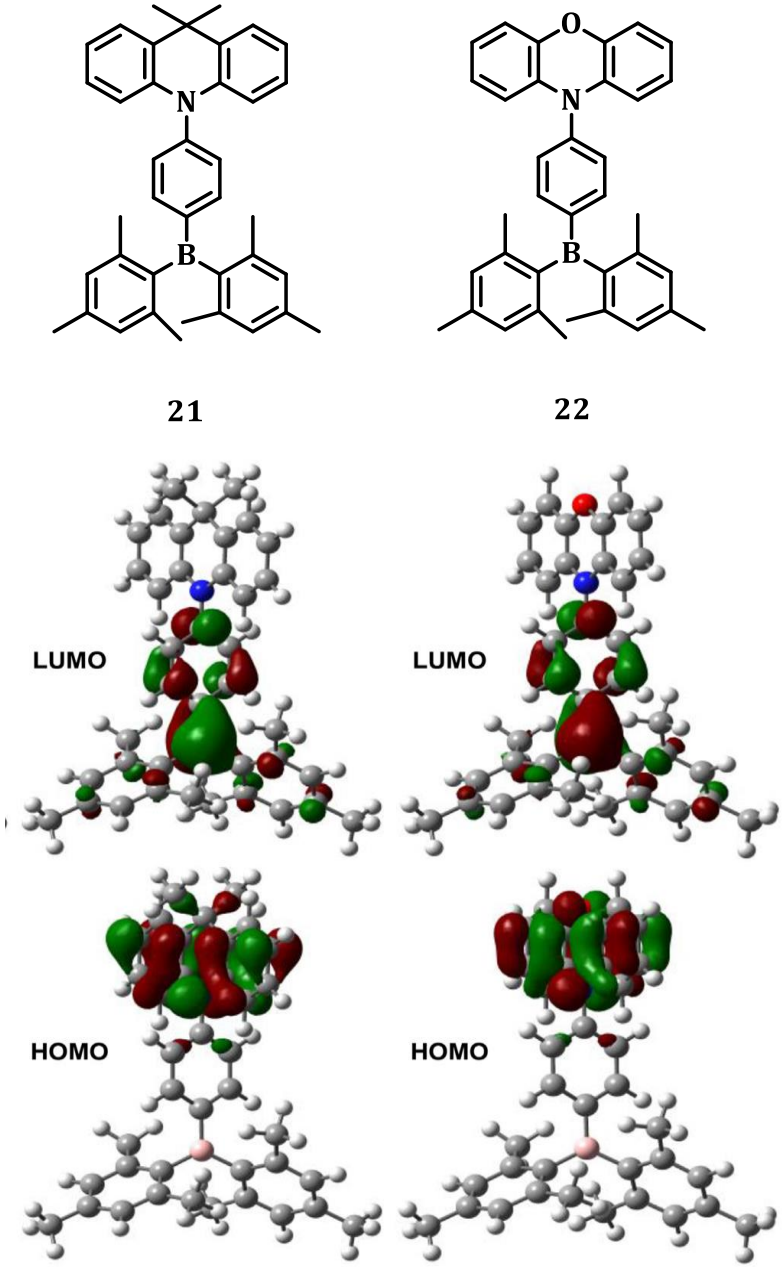

Figure 1.8. Molecular structures and HOMO and LUMO of the emitters **21** and **22**. Reproduced with permission from Reference 39. Copyright © 2016, Elsevier B.V.

showed blue and green emission with maximum EQEs of *ca.* 16.0% and *ca.* 17.3%, respectively.

Among the various organic emitters developed so far, the performances of blue emitters need to be improved in terms of efficiency, lifetime and color purity compared to that of green and red emitters. In addition, the deep blue emitters with good color purity are necessary for the generation of white light emitting diodes, which are considered as next generation solid state lighting devices. From the literature review, it is known that almost all the high efficiency green OLEDs are based on phosphorescent class of materials, which utilized expensive rare metals like Ir, Pt etc. So that, the development of novel deep blue and green emitters with good color purity and solution processability is of current research interest for the commercialization of OLEDs. Compared to the doped OLEDs, the un-doped OLEDs are more attractive due to ease of fabrication and better device reliability. In the field of OLEDs, numerous classes of organic light emitting materials have been developed and these efforts are still continuing in order to find materials that are easy to synthesize and exhibit improved solution processability and high efficiency in un-doped devices.

1.5. Chemical Sensors for Metal Ions

The molecular recognition is a fundamental and vital process in biology, which involves specific covalent or non-covalent interactions between a receptor (host) and an analyte (guest).[40] In this context, the development of molecular probes for the selective and sensitive detection of analytes has been an active area of research because such effective molecules can have biological and medicinal applications. In the host-

guest chemistry the term "sensor" is more likely related to a molecular event, which upon stimulation by any form of energy results in change of its own state and properties.[41] These changes can be successfully utilized for the qualitative and quantitative analysis of the stimulant. Depending on the type of signals produced with respect to the binding event, the sensors may be classified into two categories; electronic sensors and optical sensors.[42] The electronic sensors generate signals in the form of changes in the electrochemical properties. On the other hand, the optical sensors act as a result of changes in the optical properties of the receptor molecules. The optical and photophysical changes in a receptor molecule are found to be more valuable owing to their technical simplicity and non-invasiveness.[43] The optical molecular probes can be further classified into two categories such as i) chromogenic (or colorimetric) molecules and ii) fluorogenic (or fluorescent) molecules. In the colorimetric probes, the interactions with analytes result in absorption changes and thus the color of the receptor molecules. Whereas, the fluorescent probes involve the changes in the fluorescence properties. The colorimetric sensors can offer qualitative and quantitative information through visual changes.

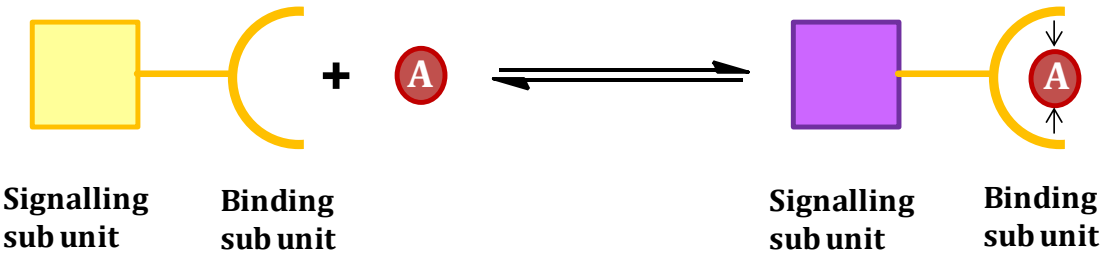

Figure 1.9. Schematic representation of binding of an analyte (guest) by a chemosensor (host), producing a complex with altered optical properties.

In general, the chemosensors consist of three components such as a chemical receptor capable of recognizing the guest with high selectivity, a signaling unit which converts the binding event into a measureable physical change and a method which measure this change and converting it into useful information (Figure 1.9). The design of probes can be broadly classified under three different approaches, [44] which are i) binding site-signaling subunit approach (chemosensors), ii) displacement approach and iii) chemodosimeter approach. These approaches differ with respect to the arrangements of the binding site or reactive site, and the signaling subunit and also the mode of interactions with the analyte. In the "binding site-signaling subunit" approach, these two parts are linked through a covalent bond.[45] The interactions of the analyte with the binding site induces changes in the electronic properties of the signaling subunit and which results in its detection. On the other hand, the displacement approach is based on the formation of molecular assemblies of binding site-signaling subunit through non-covalent interactions.[46] Up on addition of analyte, the coordinated indicator is displaced from the binding site into the solution with a concomitant change in their optical properties. In the chemodosimeter approach, a specific anion-induced chemical reaction occurs, which results in an optical signal.[47] Out of these three approaches the colorimetric chemosensors have been widely exploited.

In the designing of a colorimetric chemosensor, organic molecules having electron donor and acceptor moieties were more preferable since they exhibited intramolecular charge transfer characteristics and thus color for the chemosensor. In such molecules, a visible color change can be observed as a result of any alters in the

strength of intramolecular charge transfer during interactions with metal ions. In this context, we discuss some of the literature reported chemosensors for the selective and naked eye detection of metal ions especially for the Cu^{2+} and Hg^{2+} ions.

1.5.1. Colorimetric chemosensors for copper ions

Copper (Cu) is the third most abundant heavy metal in human body and is an essential trace element in biological systems as a catalytic co-factor in metalloenzymes like superoxide dismutase and cytochrome c oxidase. In excess, copper is toxic and can cause various diseases like Alzheimer's and Wilson's disease.[48] Therefore, it is urgently needed to develop simple and sensitive chemosensors for the detection of Cu^{2+}. Azobenzene based colorimetric receptors are one of the widely studied probes for the Cu^{2+} ion recognition properties. Jung and co-workers have developed highly selective azobenzene based colorimetric chemosensors **23a–c** for the detection of Cu^{2+} in solution.[49] In solution, the receptor **23** gave rise to a large cation induced hypsochromic shift for Cu^{2+} resulting in a visible change to the naked eye, from red to pale-yellow. Furthermore, a portable chemosensor kit was prepared by immobilizing the receptor onto the simple silica gel plate. The red color of the modified silica gel plate changes to yellow after immersion in Cu^{2+} solution and no significant color change for other selected metal ions (Figure 1.10). The plate showed detection of Cu^{2+} ions content up to 0.01 mM with the naked eye.

Li and co-workers have developed a colorimetric chemosensor **24** based on a coumarin (Figure 1.11), in which 7-di(ethoxy-carbonylmethyl)aminocoumarin serves as a chromophore core.[50] Diaminomaleonitrile was coupled with coumarin at the 3-

position carbonyl to form Schiff base derivative with enhanced intramolecular charge transfer. The imine and the rest of the amine groups in **24** serve as chelating sites for copper ions. The sensor exhibited good sensitivity and selectivity for the copper cation over other transition metal cations and alkali and alkaline earth metal cations. In the presence of Cu^{2+} ions, **24** showed a visible color change from dark yellow to red whereas, other metal ions didn't induce such a change. In addition, the test strips containing **24** were fabricated, which exhibited a good sensitivity and selectivity to Cu^{2+} ions in solution.

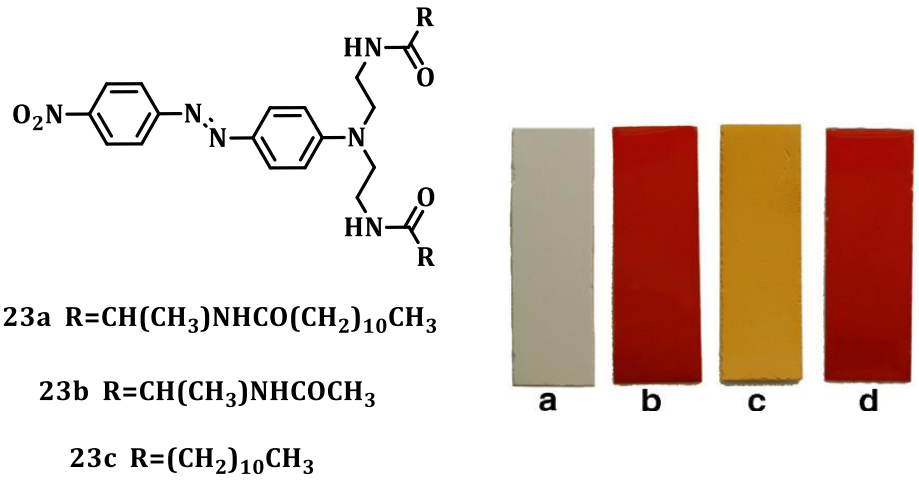

23a R=$CH(CH_3)NHCO(CH_2)_{10}CH_3$

23b R=$CH(CH_3)NHCOCH_3$

23c R=$(CH_2)_{10}CH_3$

Figure 1.10. Pictures of silica gel plates: a) unmodified, b) modified with **23**, (c) plate b after immersion in Cu^{2+} solution, and d) plate b after immersion in Li^+, Na^+, K^+, NH_4^+, Co^{2+}, Cd^{2+}, Pb^{2+}, Fe^{3+} or Zn^{2+} solution. Reproduced with permission from Reference 49. Copyright © 2006 Elsevier Ltd.

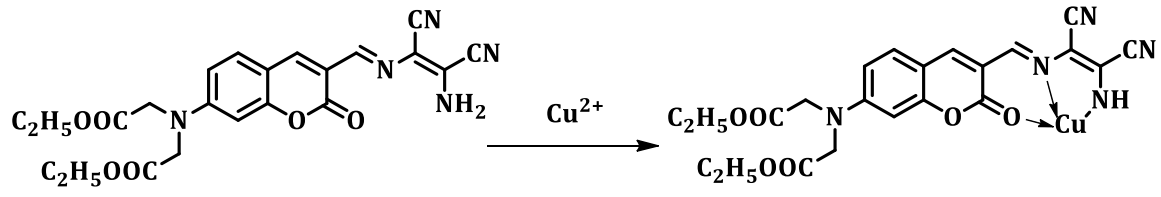

24 **24-Cu^{2+}**

Figure 1.11. Chemical structure of **24** and its binding mode with Cu^{2+} ions.

E. Sinn et al. synthesized a new fluorescein based colorimetric chemosensor **25** for the detection of Cu^{2+} ions through a ring opening mechanism of the sensor.[51] The chemosensor **25** binds to Cu^{2+} ions via the carbonyl oxygen, enamine nitrogen, and hydroxyl groups and formed a pocket with five- and six membered rings. A 1:1 complex was formed by the probe **25** and displayed reversible absorption and fluorescence enhanced responses to Cu^{2+} ions. Addition of Cu^{2+} ions to an aqueous solution of the probe **25** resulted in a visible change from colorless to deep yellow. Later, Hu and co-workers synthesized a new colorimetric probe based on Rhodamine B lactam (**26**) for the detection of Cu^{2+} ions.[52] The probe **26** found to mind with Cu^{2+} ions in the same manner the probe **25** with the formation of five- and six- membered rings. Upon interaction with Cu^{2+} ions, the probe displayed a visual color change from colorless to pink. The stoichiometry of the complex **26-Cu^{2+}** was found to be 1:1 and the detection limit was determined to be as low as 2 μM.

Kim and co-workers[53] have reported a multifunctional chemosensor **27** based on the combination of salicylaldehyde moiety and 2-amino-3-(((E)-(8-hydroxy-2,3,6,7-tetrahydro-1H,5Hpyrido[3,2,1-ij]quinolin-9yl)methylene)amino)maleonitrile (Figure 1.12). The probe exhibited the recognition of both Cu^{2+} and CN^- ions selectively over other transition elements and various anions and exhibited visual color change from violet to pale yellow for CN^- and Cu^{2+} ions, separately in different solvent systems. The observed color change has been attributed to the blue shift generated by the decrease in the push pull effect of the intramolecular charge transfer transition. The stoichiometry of the complex was found to be 1:1 ratio.

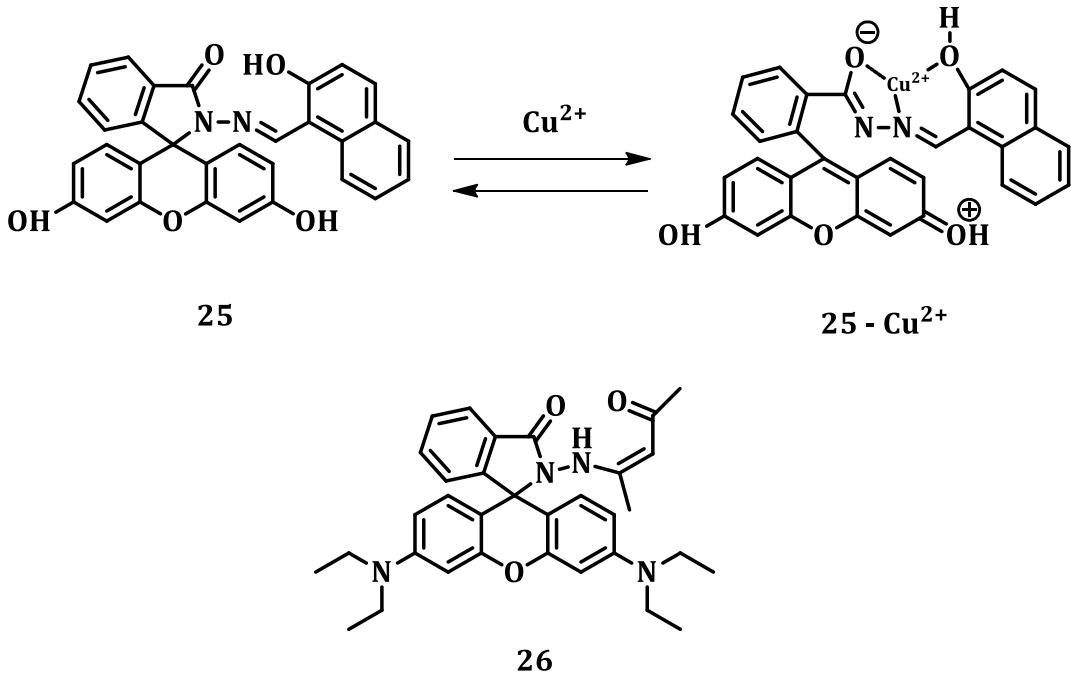

Figure 1.12. Chemical structures of the probes **25** and **26** and the mode of binding of Cu^{2+} ions with the probe **25**.

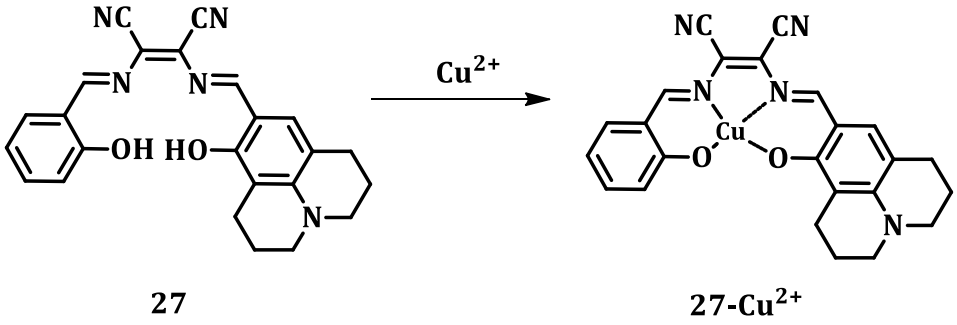

Figure 1.13. Chemical structure of the probe **27** and its binding mode with Cu^{2+} ions.

1.5.2. Colorimetric chemosensors for mercury ions

Mercury (Hg) is a dangerous and widespread global pollutant, which causes severe environmental and health hazards. The marine aquatic organisms convert mercury into methylmercury, a potent neurotoxin. In humans, bioaccumulation of

methylmercury through the food chain leads to serious sensory, motor, and cognitive disorders.[54] Therefore, the detection and quantification of Hg^{2+} is important and which has been an active area of research.

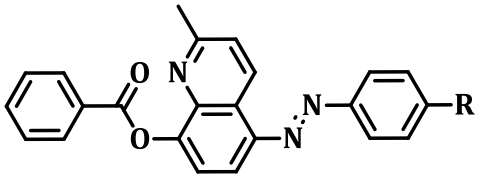

28a R=H

28b R=OCH_3

28c R=$N(CH_3)_2$

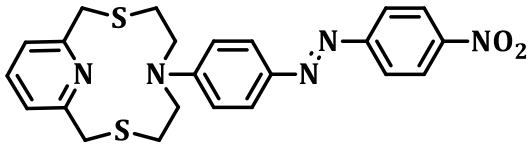

29

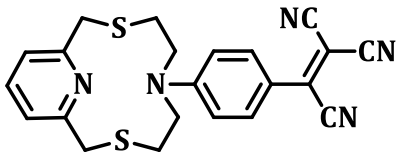

30

Chart 1.5. Chemical structures of the chemosensors **28**-**30**.

Huang and co-workers have reported a series of 8-hydroxyquinoline benzoates **28a-c** (Chart 1.5) with diverse azo-substituents, such as electron donating groups -OCH_3 and -$N(CH_3)_2$ and demonstrated their sensing properties.[55] The probes **28b** and **28c** have a D-π-D structure with the electron donating groups -OCH_3 or -$N(CH_3)_2$ and the relative weak donor, benzoate quinolinyl group. The complexation of these probes with Hg^{2+} make benzoate quinolinyl group as an electron acceptor, and then the complexes **28b-Hg^{2+}** or **28c-Hg^{2+}** act as D-π-A structure with the enhanced ICT characteristics. As a result, after complexation, the absorption spectra were red shifted and a visible color change was observed for **28c** from yellow to red in acetonitrile solution. All the derivatives were found to be highly selective to Hg^{2+} ions over the other transition metal ions.

Choi and co-workers[56] have synthesized two chromogenic N_2S_2-donor macrocycles functionalized with p-nitroazobenzene (**29**) and phenyltricyanovinyl (**30**) units for the naked eye detection of Hg^{2+} ions (Chart 1.5). Because of the D-π-A structures, these derivatives showed ICT band in the absorption spectra and thus intense color. Both these systems exhibited excellent Hg^{2+} selectivity by showing a visible metal induced color change from red to colorless. The selective recognition was attributed to the formation of stable 1:1 complexes between the ligands and Hg^{2+} ions in solution.

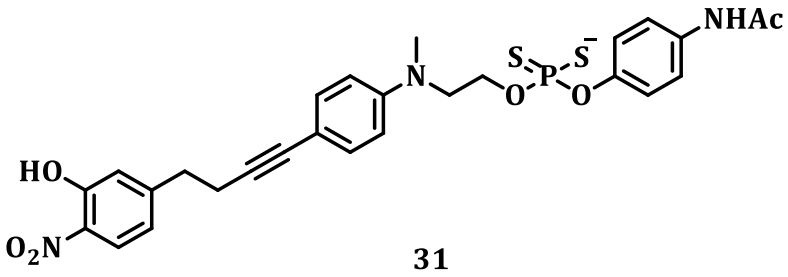

31

Chart 1.6. Chemical structures of the chemosensor **31.**

K. D. Janda et al. have reported a new phosphorodithioate based ligand **31** that specifically communicates a color change when exposed to the mercuric ions.[57] The detection was achieved by monitoring the regulation of the dye's charge transfer upon binding of Hg^{2+} to a pendant sulfur-containing ligand. The probe **31** has a soft metal binding site, phosphorodithioate and an adjacent amine group, which were effectively involved in the charge transfer (Chart 1.6). The binding of Hg^{2+} ions to the phosphorodithioate group alter the electron donating capability of the terminal nitrogen atom of the amine moiety through ligand participation and ultimately altering

the charge transfer and hypsochromically shifting of the absorption maximum. The addition of mercuric ions resulted in a distinct color change from yellow to red.

A benzothiazolium hemicyanine dye **32** was employed by Palomares and co-workers for the selective and sensitive detection of Hg^{2+} ions in aqueous solutions.[58] The hemicyanine dye **32** found to undergo interactions with the Hg^{2+} ions through the the involvement of the electron donor aniline moiety and electron acceptor benzothiazolium species, while the sulfur atom acted as the coordinating element. In the presence of Hg^{2+}, the dye **32** formed a stable complex with 1:1 stoichiometry, and found to undergo geometric transformation from *trans*-isomer to the *cis*-configuration. This interaction induced a visible color change in the dye form pink red to yellow at micromolar concentrations of mercury ions (Figure 1.13). The color change and quenching of the dye emission were observed selectively for mercury ions when compared to the other biologically relevant cations such as Pb^{2+}, Cd^{2+}, Zn^{2+}, Fe^{2+} etc.

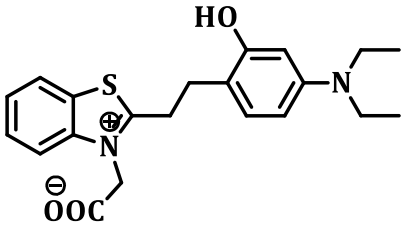

32

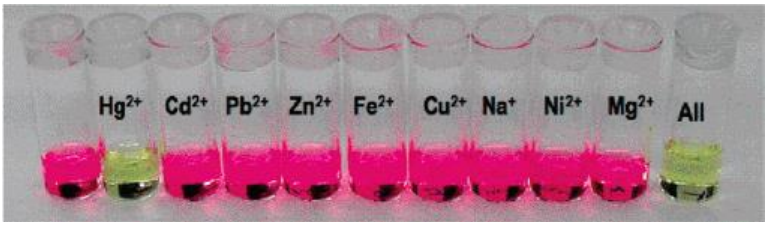

Figure 1.14. Structure of the dye **32** and its selectivity towards Hg^{2+} in aqueous solutions. Reproduced with permission from Reference 58. Copyright 2006 American Chemical Society.

Tong and co-workers have designed a highly selective colorimetric chemosensor 2-(4-(diphenyl-amino)phenyl)quinazoline-4(3H)-thione) (**33**) for the selective and naked eye detection of Hg^{2+} ions.[59] With the addition of Hg^{2+} ions, this probe showed a 2:1 stoichiometry through a coordination bond interaction between the sulfur atom and Hg^{2+} with an association constant of 4.17 x 10^8 M^{-2} (Figure 1.15). The interaction of the probe with Hg^{2+} ions resulted in a color change from yellow to red having a detection limit of 1.5 μM. The probe was found to be extraordinarily selective to Hg^{2+} ions over a wide range of mono and bivalent metal ions. The absorption spectrum of the **33**-Hg^{2+} complex was found to be restored upon the addition of KI to the solution of the complex. In an another report, Yoon and co-workers have reported novel Rhodamine B derivatives **34** and **35** bearing mono and bis-boronic acid groups, respectively, as Hg^{2+} selective fluorescent and colorimetric sensors.[60] Both these derivatives displayed fluorescent enhancement and distinct color change from colorless to red with the addition of Hg^{2+}. The large fluorescence enhancement as well as the colorimetric change can be attributed to the spirolactam ring opening induced by the Hg^{2+}ions. A 1:1 stoichiometry was observed for the complexes **34-Hg^{2+}** and **35-Hg^{2+}** having the association constants of 3.3 x 10^3 M^{-1} and 2.1 x 10^4 M^{-1}. Compared to the mono-boronic probe **34**, the bis-boronic probe **35** displayed a nine-fold tighter binding with Hg^{2+}. The stronger binding can be attributed to an additional boronic acid ligand in the case of the probe **35**. This observation along with larger binding constant observed for **35** suggests that boronic acid moiety plays an important role in the binding with Hg^{2+}ions.

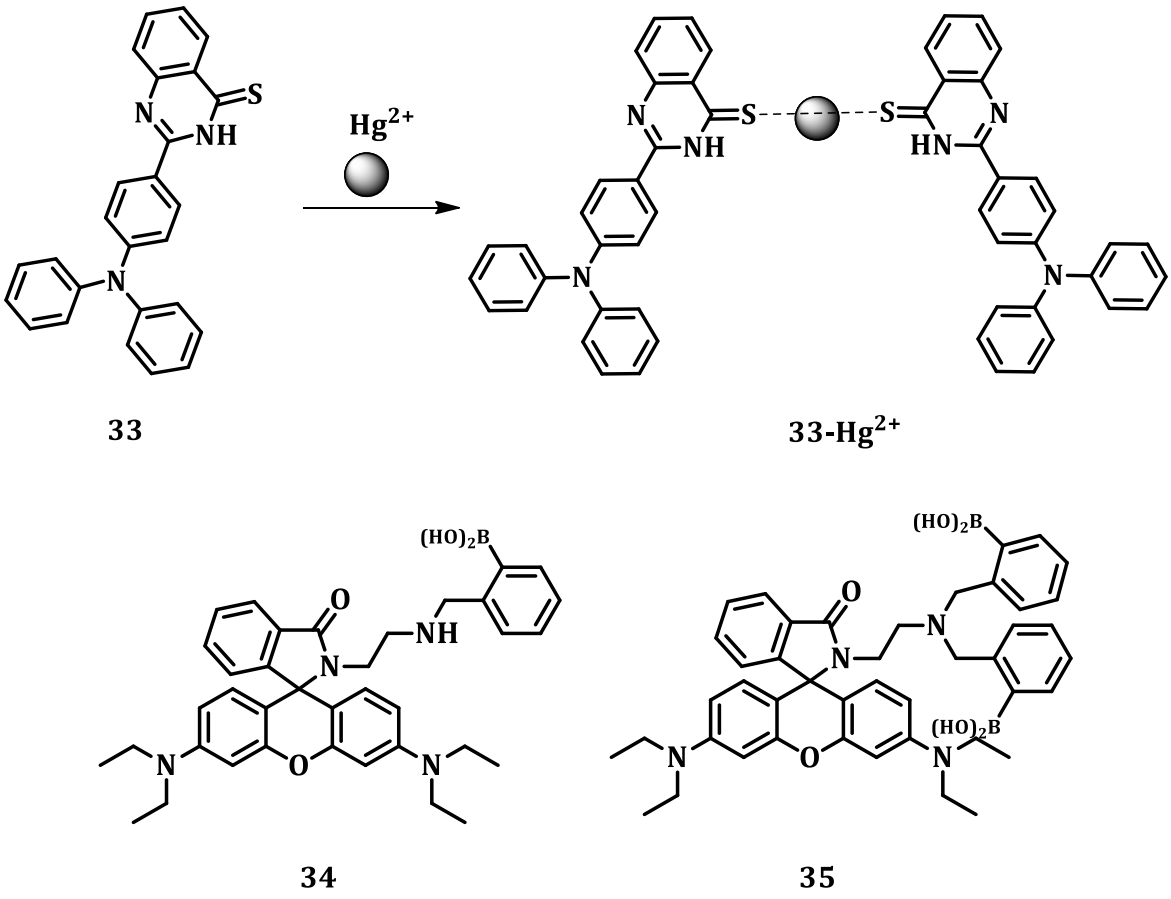

Figure 1.15. Structures of the probes **33-35** and the binding mechanism of the probe **33** with Hg^{2+} ions in THF.

1.6. Objectives of the Present Thesis

Development of functionalized organic donor-acceptor molecules having favorable photophysical properties for sensing and optoelectronic applications has immense significance due to their advantages like easy synthesis, high purity, tunable energy and low cost over their polymer and inorganic analogues. In this context, our main objective has been to design and synthesis of a few functional organic small molecules with D-π-A structure and investigation of their utility as emitters in the organic light emitting diodes (OLEDs) and as metal ion sensors. In OLEDs, the green

OLEDs belong to the costly phosphorescent class of emitters and hence there is an urgent need to develop highly efficient and low cost green emitters. In this regard, another objective of this thesis has been to design novel solution processable green fluorescent emitters based on phenoxazine donor and oxadiazole acceptors and investigation of their photophysical, thermal, morphological and device performance aspects. Yet another objective has been to develop solution processable deep blue organic emitters based on carbazole donor and oxadiazole acceptor and study of their optoelectronic properties. The last objective of the thesis has been to design donor-acceptor based chemosensors and systematic investigation of their potential as selective and sensitive probes for the detection of biologically relevant metal ions.

Our results indicate that the newly synthesized phenoxazine-oxadiazole hybrids exhibited favorable photophysical, thermal and morphological stability properties for the fabrication of OLEDs. The fabricated un-doped solution processed OLED devices based on these dyads showed green electroluminescence with good to marginal luminescence characteristics. Interetingly, the carbazole-oxadiazole dyads, on the other hand, exhibited deep blue emission with good fluorescence quantum yields and color purity both in the solution and film state. The observed excellent thermal and morphological stability of these dyads made them as potential candidates for the device fabrication. Furthermore, we have fabricated un-doped deep blue OLEDs based on these dyads by a solution process method. Our results indicate that, the adopted design strategy afforded a reduced aggregation and good solution processability for the developed emitters.

Lastly, the chemosensor developed based on quinolines-carbaldehyde found to selectively detect both $Cu^{2+}$and Hg^{2+} ions over other transition metal ions with an easy, well defined naked eye visible color change from yellow to colorless and pink, respectively. Further, we have extended the potential of this probe for the on-site analysis by fabricating a simple solid state dipstick device that can be used for the easy visual detection and analysis of Cu^{2+} and Hg^{2+} ions in the aqueous medium. Overall, the investigated functional organic donor-acceptor dyad molecules showed interesting photophysical properties and thereby exhibited their potential as efficient green and blue emitters in OLEDs and molecular probes for the recognition of Cu^{2+} and Hg^{2+} ions.

1.7. References

(1) Lin, Y.; Li, Y.; Zhan, X. *Chem. Soc. Rev.* **2012**, *41*, 4245.

(2) (a) Marsden, J. A.; Miller, J. J.; Shirtcliff, L. D.; Haley, M. M. *J. Am. Chem. Soc.* **2005**, *127*, 2464(b) Liu, X.; Sun, Y.; Hsu, B. B. Y.; Lorbach, A.; Qi, L.; Heeger, A. J.; Bazan, G. C. *J. Am. Chem. Soc.* **2014**, *136*, 5697.

(3) Bures, F. *RSC Adv.* **2014**, *4*, 58826.

(4) (a) Roncali, J. *Chem. Rev.* **1997**, *97*, 173(b) Perepichka, D. F.; Bryce, M. R. *Angew. Chem. Int. Ed.* **2005**, *44*, 5370.

(5) Kulhánek, J.; Bureš, F. *Beilstein J. Org. Chem.* **2012**, *8*, 25.

(6) (a) Kulhánek, J.; Bureš, F.; Opršal, J.; Kuznik, W.; Mikysek, T.; Růžička, A. *Asian J. Org. Chem.* **2013**, *2*, 422(b) Albert, I. D. L.; Marks, T. J.; Ratner, M. A. *J. Am. Chem. Soc.* **1997**, *119*, 6575.

(7) (a) Li, C.; Wei, J.; Han, J.; Li, Z.; Song, X.; Zhang, Z.; Zhang, J.; Wang, Y. *J. Mater. Chem. C* **2016**, *4*, 10120(b) Vivas, M. G.; Silva, D. L.; Malinge, J.; Boujtita, M.; Zaleśny, R.; Bartkowiak, W.; Ågren, H.; Canuto, S.; De Boni, L.; Ishow, E.; Mendonca, C. R. *Scientific Reports* **2014**, *4*, 4447.

(8) Li, Y.; Liu, J.-Y.; Zhao, Y.-D.; Cao, Y.-C. *Mater. Today* **2017**, *20*, 258.

(9) Gonçalves, M. S. T. *Chem. Rev.* **2009**, *109*, 190.

(10) Senge, M. O.; Fazekas, M.; Pintea, M.; Zawadzka, M.; Blau, W. J. *Eur. J. Org. Chem.* **2011**, *2011*, 5797.

(11) (a) Won, Y. S.; Yang, Y. S.; Kim, J. H.; Ryu, J.-H.; Kim, K. K.; Park, S. S. *Energy Fuels* **2010**, *24*, 3676(b) Michinobu, T.; Satoh, N.; Cai, J.; Li, Y.; Han, L. *J. Mater. Chem. C* **2014**, *2*, 3367.

(12) Singer, K. D.; Sohn, J. E.; King, L. A.; Gordon, H. M.; Katz, H. E.; Dirk, C. W. *J. Opt. Soc. Am. B* **1989**, *6*, 1339.

(13) Jiang, P.; Guo, Z. *Coord. Chem. Rev.* **2004**, *248*, 205.

(14) Li, X.; Cui, S.; Wang, D.; Zhou, Y.; Zhou, H.; Hu, Y.; Liu, J. g.; Long, Y.; Wu, W.; Hua, J.; Tian, H. *ChemSusChem* **2014**, *7*, 2879.

(15) Luo, J.; Zhang, J. *ACS Catalysis* **2016**, *6*, 873.

(16) Morone, M.; Beverina, L.; Abbotto, A.; Silvestri, F.; Collini, E.; Ferrante, C.; Bozio, R.; Pagani, G. A. *Org. Lett.* **2006**, *8*, 2719.

(17) Ooyama, Y.; Inoue, S.; Nagano, T.; Kushimoto, K.; Ohshita, J.; Imae, I.; Komaguchi, K.; Harima, Y. *Angew. Chem. Int. Ed.* **2011**, *50*, 7429.

(18) Geffroy, B.; Roy, P. l.; Prat, C. *Polym. Int.* **2006**, *55*, 572.

(19) Tang, C. W.; VanSlyke, S. A. *Appl. Phys. Lett.* **1987**, *51*, 913.

(20) (a) Tao, S.; Hong, Z.; Peng, Z.; Ju, W.; Zhang, X.; Wang, P.; Wu, S.; Lee, S. *Chem. Phys. Lett.* **2004**, *397*, 1(b) Jeon, S.-O.; Jeon, Y.-M.; Kim, J.-W.; Lee, C.-W.; Gong, M.-S. *Org. Electron.* **2008**, *9*, 522(c) Lee, J.; Park, C. H.; Kwon, J.; Yoon, S. C.; Do, L.-M.; Lee, C. *Synth. Met.* **2012**, *162*, 1961(d) Fang, Q.; Xu, B.; Jiang, B.; Fu, H.; Chen, X.; Cao, A. *Chem. Commun.* **2005**, 1468.

(21) (a) Baldo, M. A.; O'Brien, D. F.; You, Y.; Shoustikov, A.; Sibley, S.; Thompson, M. E.; Forrest, S. R. *Nature* **1998**, *395*, 151(b) Wilson, J. S.; Dhoot, A. S.; Seeley, A. J. A. B.; Khan, M. S.; Köhler, A.; Friend, R. H. *Nature* **2001**, *413*, 828.

(22) (a) Baldo, M. A.; Lamansky, S.; Burrows, P. E.; Thompson, M. E.; Forrest, S. R. *Appl. Phys. Lett.* **1999**, *75*, 4(b) Adachi, C.; Baldo, M. A.; Thompson, M. E.; Forrest, S. R. *J. Appl. Phys.* **2001**, *90*, 5048.

(23) Zhang, Q.; Komino, T.; Huang, S.; Matsunami, S.; Goushi, K.; Adachi, C. *Adv. Funct. Mater.* **2012**, *22*, 2327.

(24) (a) Endo, A.; Ogasawara, M.; Takahashi, A.; Yokoyama, D.; Kato, Y.; Adachi, C. *Adv. Mater.* **2009**, *21*, 4802(b) Endo, A.; Sato, K.; Yoshimura, K.; Kai, T.; Kawada, A.; Miyazaki, H.; Adachi, C. *Appl. Phys. Lett.* **2011**, *98*, 083302.

(25) Uoyama, H.; Goushi, K.; Shizu, K.; Nomura, H.; Adachi, C. *Nature* **2012**, *492*, 234.

(26) (a) Chang, C.-H.; Kuo, M.-C.; Lin, W.-C.; Chen, Y.-T.; Wong, K.-T.; Chou, S.-H.; Mondal, E.; Kwong, R. C.; Xia, S.; Nakagawa, T.; Adachi, C. *J. Mater. Chem.* **2012**, *22*, 3832(b) Lee, S. Y.; Yasuda, T.; Nomura, H.; Adachi, C. *Appl. Phys. Lett.* **2012**, *101*, 093306.

(27) Shizu, K.; Sakai, Y.; Tanaka, H.; Hirata, S.; Adachi, C.; Kaji, H. *ITE Trans. on MTA* **2015**, *3*, 108.

(28) (a) Rajamalli, P.; Senthilkumar, N.; Gandeepan, P.; Ren-Wu, C.-Z.; Lin, H.-W.; Cheng, C.-H. *J. Mater. Chem. C* **2016**, *4*, 900(b) Liu, M.; Seino, Y.; Chen, D.; Inomata, S.; Su, S.-J.; Sasabe, H.; Kido, J. *Chem. Commun.* **2015**, *51*, 16353.

(29) Tanaka, H.; Shizu, K.; Miyazaki, H.; Adachi, C. *Chem. Commun.* **2012**, *48*, 11392.

(30) Tsai, W.-L.; Huang, M.-H.; Lee, W.-K.; Hsu, Y.-J.; Pan, K.-C.; Huang, Y.-H.; Ting, H.-C.; Sarma, M.; Ho, Y.-Y.; Hu, H.-C.; Chen, C.-C.; Lee, M.-T.; Wong, K.-T.; Wu, C.-C. *Chem. Commun.* **2015**, *51*, 13662.

(31) Zhang, Q.; Li, J.; Shizu, K.; Huang, S.; Hirata, S.; Miyazaki, H.; Adachi, C. *J. Am. Chem. Soc.* **2012**, *134*, 14706.

(32) Huang, B.; Qi, Q.; Jiang, W.; Tang, J.; Liu, Y.; Fan, W.; Yin, Z.; Shi, F.; Ban, X.; Xu, H.; Sun, Y. *Dyes Pigm.* **2014**, *111*, 135.

(33) Zhang, Q.; Li, B.; Huang, S.; Nomura, H.; Tanaka, H.; Adachi, C. *Nat. Photonics* **2014**, *8*, 326.

(34) Xie, G.; Li, X.; Chen, D.; Wang, Z.; Cai, X.; Chen, D.; Li, Y.; Liu, K.; Cao, Y.; Su, S. J. *Adv. Mater.* **2016**, *28*, 181.

(35) Lee, J.; Shizu, K.; Tanaka, H.; Nomura, H.; Yasuda, T.; Adachi, C. *J. Mater. Chem. C* **2013**, *1*, 4599.

(36) Tanaka, H.; Shizu, K.; Lee, J.; Adachi, C. *J. Phys. Chem. C* **2015**, *119*, 2948.

(37) Lee, S. Y.; Adachi, C.; Yasuda, T. *Adv. Mater.* **2016**, *28*, 4626.

(38) (a) Numata, M.; Yasuda, T.; Adachi, C. *Chem. Commun.* **2015**, *51*, 9443(b) Kitamoto, Y.; Namikawa, T.; Ikemizu, D.; Miyata, Y.; Suzuki, T.; Kita, H.; Sato, T.; Oi, S. *J. Mater. Chem. C* **2015**, *3*, 9122(c) Suzuki, K.; Kubo, S.; Shizu, K.; Fukushima, T.; Wakamiya, A.; Murata, Y.; Adachi, C.; Kaji, H. *Angew. Chem.* **2015**, *127*, 15446.

(39) Kitamoto, Y.; Namikawa, T.; Suzuki, T.; Miyata, Y.; Kita, H.; Sato, T.; Oi, S. *Org. Electron.* **2016**, *34*, 208.

(40) Lehn, J. M. *Angew. Chem. Int. Ed.* **1988**, *27*, 89.

(41) Prodi, L. *New J. Chem.* **2005**, *29*, 20.

(42) Prodi, L.; Bolletta, F.; Montalti, M.; Zaccheroni, N. *Coord. Chem. Rev.* **2000**, *205*, 59.

(43) Janata, J. *Chem. Rev.* **2008**, *108*, 327.

(44) Martínez-Máñez, R.; Sancenón, F. *Chem. Rev.* **2003**, *103*, 4419.

(45) Bissell, R. A.; de Silva, A. P.; Gunaratne, H. Q. N.; Lynch, P. L. M.; Maguire, G. E. M.; Sandanayake, K. R. A. S. *Chem. Soc. Rev.* **1992**, *21*, 187.

(46) Wiskur, S. L.; Ait-Haddou, H.; Lavigne, J. J.; Anslyn, E. V. *Acc. Chem. Res.* **2001**, *34*, 963.

(47) Martínez-Máñez, R.; Sancenón, F. *Coord. Chem. Rev.* **2006**, *250*, 3081.

(48) Bull, P. C.; Thomas, G. R.; Rommens, J. M.; Forbes, J. R.; Cox, D. W. *Nat. Genet.* **1993**, *5*, 327.

(49) Lee, S. J.; Lee, S. S.; Jeong, I. Y.; Lee, J. Y.; Jung, J. H. *Tet. Lett.* **2007**, *48*, 393.

(50) Sheng, R.; Wang, P.; Gao, Y.; Wu, Y.; Liu, W.; Ma, J.; Li, H.; Wu, S. *Org. Lett.* **2008**, *10*, 5015.

(51) Abebe, F. A.; Sinn, E. *Tet. Lett.* **2011**, *52*, 5234.

(52) Hu, Y.; Zhang, J.; Lv, Y.-Z.; Huang, X.-H.; Hu, S.-l. *Spectrochimica Acta Part A: Molecular and Biomolecular Spectroscopy* **2016**, *157*, 164.

(53) Jo, T. G.; Na, Y. J.; Lee, J. J.; Lee, M. M.; Lee, S. Y.; Kim, C. *Sens. Actuators B, Chem.* **2015**, *211*, 498.

(54) (a) Harris, H. H.; Pickering, I. J.; George, G. N. *Science* **2003**, *301*, 1203(b) Boening, D. W. *Chemosphere* **2000**, *40*, 1335.

(55) Cheng, Y.; Zhang, M.; Yang, H.; Li, F.; Yi, T.; Huang, C. *Dyes Pigm.* **2008**, *76*, 775.

(56) Lee, H. G.; Lee, J.-E.; Choi, K. S. *Inorg. Chem. Commun.* **2006**, *9*, 582.

(57) Brümmer, O.; La Clair, J. J.; Janda, K. D. *Org. Lett.* **1999**, *1*, 415.

(58) Tatay, S.; Gaviña, P.; Coronado, E.; Palomares, E. *Org. Lett.* **2006**, *8*, 3857.

(59) Mei, Q.; Wang, L.; Tian, B.; Yan, F.; Zhang, B.; Huang, W.; Tong, B. *New J. Chem.* **2012**, *36*, 1879.

(60) Kim, S. K.; Swamy, K. M. K.; Chung, S.-Y.; Kim, H. N.; Kim, M. J.; Jeong, Y.; Yoon, J. *Tet. Lett.* **2010**, *51*, 3286.

Chapter 2

Design of Green Light Emitting Dyads Based on Phenoxazine and Oxadiazole for OLED Applications

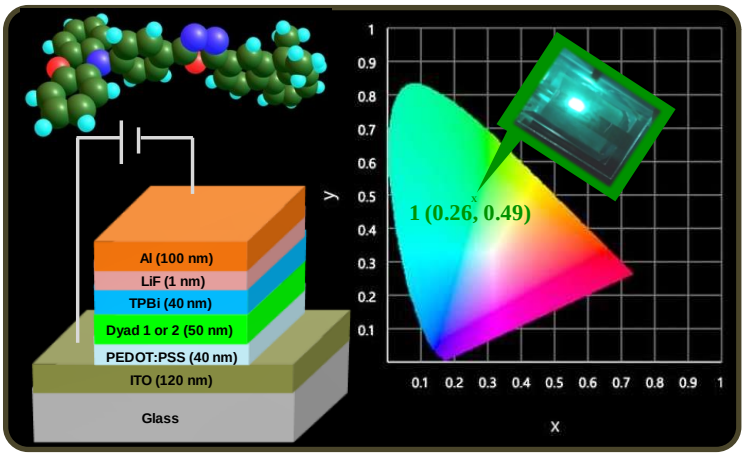

2.1. Abstract

With an objective to develop organic small molecule based green light emitting materials, we have synthesized the dyads **1** and **2** having electron donating phenoxazine and accepting oxadiazole groups. The intramolecular electron communication between the donor and acceptor moieties of these dyads was tuned by changing the substitution pattern at the phenylene linker. The dyad **1** showed a broad absorption band at 390 nm and an intense band at 330 nm. The band at 390 nm disappeared and a new shoulder at 345 nm was formed as the position of the phenoxazine moiety changed from the *para*-position (for the dyad **1**) to the *meta*-position (for the dyad **2**). These dyads showed green fluorescence both in toluene and film state. The *meta*- substituted dyad **2** exhibited a substantially low fluorescence

quantum yield (Φ_F = 0.03) compared to that of *para*- derivative dyad **1** (Φ_F = 0.25) due to the decrease in conjugation between the donor and acceptor subunits. On changing the polarity of the solvent from non-polar to polar, we observed negligible changes in the absorption maxima, while the emission maxima showed redshift of *ca.* 155 nm and 160 nm for the dyads **1** and **2**, respectively. Furthermore, we observed significant changes in the dipole moment of *ca.* 19.51 and 19.42 D for the dyads **1** and **2** respectively, which suggest ICT character between donor and acceptor moieties. These dyads exhibited lower ΔE_{ST} values of *ca.* 0.19 eV and delayed fluorescence which confirmed their potential as TADF emitters.

The ground state optimized geometries of the dyads **1** and **2** showed that the HOMO and LUMO levels are exclusively centered on the donor and acceptor moieties, respectively. The HOMO and LUMO values estimated from the measured redox potentials and optical band gap and calculated using DFT methods were found to be in reasonably agreement. From the thermogravimetric analysis, it was observed that both the dyads are thermally quite stable up to 425 °C. Moreover, we obtained a smooth and homogeneous film by a solution process which confirms the good film forming ability of these dyads. Furthermore, we have fabricated the solution processed un-doped OLEDs based on these dyads, with device configuration having ITO (120 nm)/ PEDOT: PSS (40 nm)/ EML (50 nm)/ TPBi (40 nm)/ LiF(1 nm)/ Al (100 nm). The devices thus fabricated exhibited green emission with CIE coordinates of (0.26, 0.49) and (0.27, 0.47) for the dyads **1** and **2**, respectively, with a luminance intensity maximum of *ca.*1751 cd m^{-2} for the dyad **1**, thereby demonstrating its potential use in OLED applications.

2.2. Introduction

Design of novel organic luminescent molecules for OLEDs and study of their structure-property relationship have attracted much attention since the pioneering work of Tang and Vanslyke in 1980s.[1] The discovery of new emitting materials for the development of efficient devices is quite challenging.[2] Among the various emitters reported, the green emitters have a great deal of importance since green is one of the three primary colours used for the white light emission.[3] It was noted that the high efficiency green OLEDs belong to the phosphorescent class of emitters, which utilizes expensive rare earth metals like Ir, Pt etc. For example, Cheng and co-workers have reported solution processable iridium dendrimers with rigid hole transporting carbazole dendrons having an external quantum efficiency (EQE) value of *ca.* 16.6%.[4]

In another seminal work, Osawa and co-workers have reported a complex, (1,2-bis(o-ditolylphosphino)benzene)CuBr, which exhibited green luminescence and current efficiency of *ca.* 65.3 cd A^{-1} and EQE of *ca.* 21.3%.[5] In this context, the design of efficient organic green fluorescent emitters has been an active area of research in recent years. The small organic donor-acceptor type fluorophores have distinct advantages in OLED device fabrication over polymers and inorganic compounds, because such systems can be easily synthesized, purified and analyzed.[6] In addition, one can have large degree of control over the electronic and optical properties of such systems in accordance with the structural modifications with different donor and acceptor moieties.[7]

The fluorescent OLEDs of multilayered structures with host-dopant systems have also been reported.[8] Considering the practical applications, sequential layer-by-layer fabrication procedures and the precise control of host-dopant ratio increases the complexity and thus the cost of such OLEDs.[9] For this reason, organic light emitting materials with bipolar characteristics are being developed, such that the device architecture can be simplified.[10] The bipolar charge transport can be achieved by incorporating both electron donating and withdrawing moieties into the same molecule.[11] Further, these unsymmetrical structures, when substituted with long alkyl chains provide better solubility, hence improved solution processability and reduced aggregation induced quenching of emission intensity.[12] In this respect, development of non-doped OLEDs based on solution processable small molecules with bipolar characteristics is highly desirable for their commercialization.

In general, the materials having electron withdrawing molecular building blocks like oxadiazoles, pyridine, phenanthroline, benzimidazole, quinolines, triazines, and quinoxalines have been used as electron transport building blocks in OLEDs.[13] Among these, 1,3,4-oxadiazoles are well known for their electron transporting and hole blocking abilities due to their electron deficient nature.[14] Moreover, incorporation of such oxadiazole group found to enhance the thermal stability, which is an essential property of OLED materials.[15] On the other hand, the electron donating building blocks like carbazoles,[16] diphenylamine,[17] phenoxazine,[18] and phenothiazine,[19] were extensively studied and among these, the phenoxazine derivatives have been widely used in the design of green

emitters and as hole transporting materials.[20] In addition, the morpholine like six membered ring of phenoxazine unit found to induce steric repulsion towards the neighbouring substituents and thereby resulting in a twisted structure. The formation of such a structure is important for facilitating an effective separation of HOMO and LUMO in these systems.[20] In addition, such D-A dyads having a small ΔE_{ST} value make them useful as thermally activated delayed fluorescence emitters (TADF), which are important systems to enhance efficiency of OLEDs.[21]

With an objective to develop organic light emitting diodes based on donor acceptor systems, we designed and synthesised two novel green luminescent dyads **1** and **2** (Chart 2.1) having electron donating phenoxazine and accepting oxadiazole moieties and have investigated their photophysical properties, morphological aspects and also their use in OLEDs. Interestingly, these systems exhibited substitution dependent photophysical properties and showed green emission in solution, thin-film and in the devices fabricated based on these dyads. Interestingly, in the device evaluation, we observed a maximum luminescence intensity of *ca.* 1751 cd m^{-2} for the dyad **1**, which clearly demonstrates its potential use in OLEDs applications.

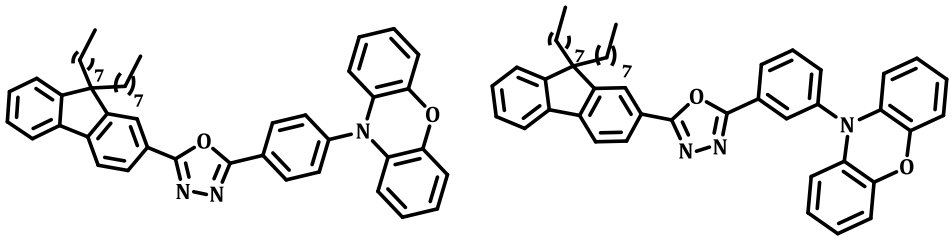

1 **2**

Chart 2.1. Structures of the investigated donor-acceptor dyads **1** and **2**.

2.3. Results and Discussion

2.3.1. Synthesis and photophysical properties

The designed dyads have donor phenoxazine and acceptor 2-(9,9-dioctyl-9H-fluoren-2-yl)-1,3,4-oxadiazole connected through a phenylene linker by *para*- (dyad **1**) and *meta*- (dyad **2**) substitution. To achieve the solution processability, we have adopted the unsymmetrical structures, incorporating the long alkyl chains. As shown in Scheme 2.1, the precursors, **7a** and **7b** were synthesized by modifying the reported procedures,[22] in *ca.* 75% yields. The mono bromination of fluorene followed by the alkylation yielded 2-bromo-9,9-dioctyl-9H-fluorene in good yields. The product upon Rosenmund-von Braun reaction gave the corresponding carbonitrile derivatives, 9,9-dioctyl-

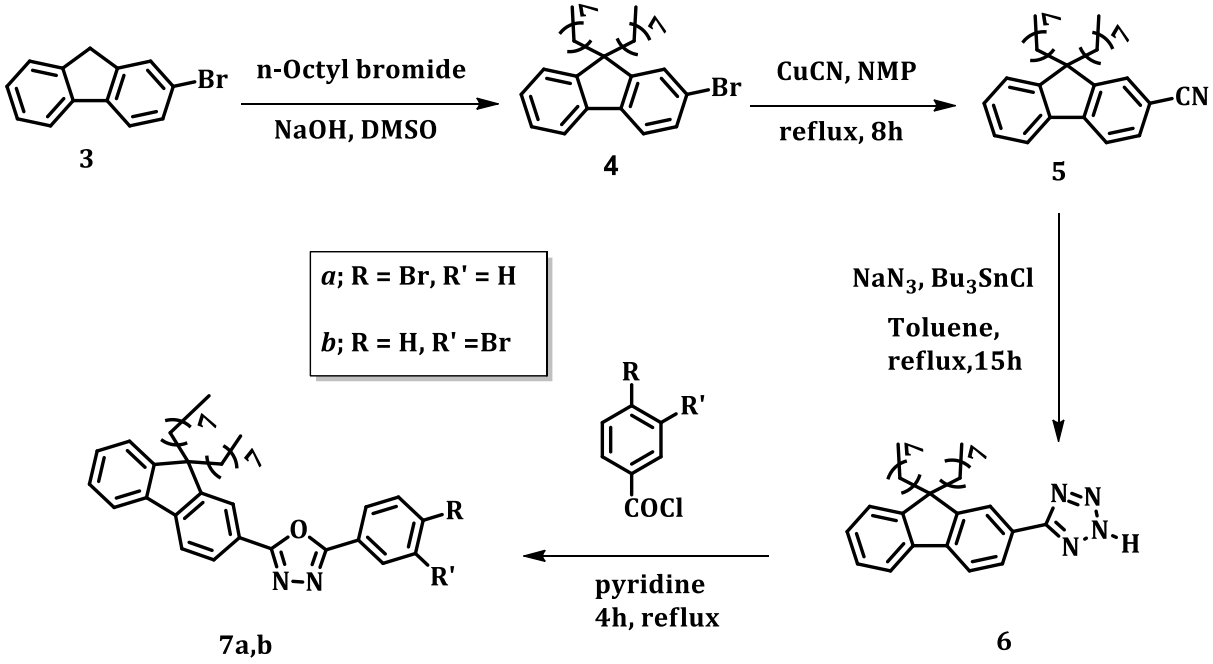

Scheme 2.1. Synthetic method adopted for the precursors **7a** and **7b**.

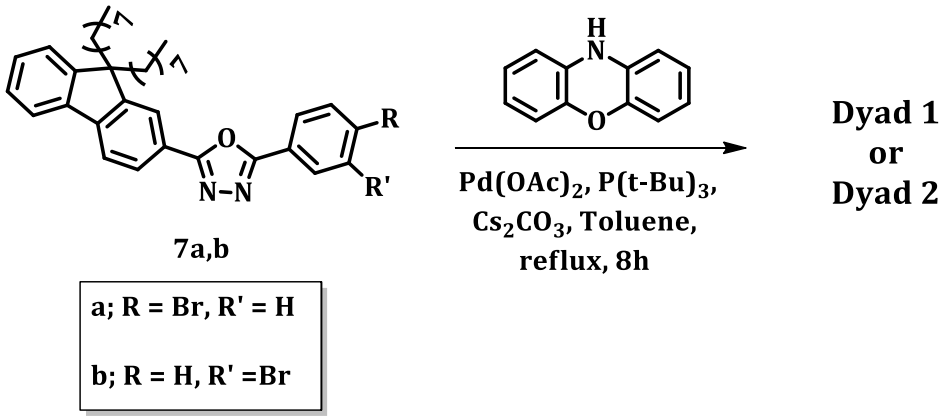

Scheme 2.2. Synthetic method adopted for the donor-acceptor dyads **1** and **2**.

9H- fluorene-2-carbonitrile in *ca.* 70% yields. The tetrazole derivatives, on the other hand, were prepared and which on refluxing with *para*- and *meta*-bromobenzoyl chlorides, gave the precursors **7a** and **7b** in excellent yields. The synthesis of the target dyad molecules were achieved through Buchwald-Hartwig coupling reaction between the donor and acceptor molecules (Scheme 2.2).[23] The phenoxazine system, upon Pd-catalyzed cross-coupling reaction with **7a** and **7b** in presence of cesium carbonate as the additive base, gave the dyads **1** and **2** in *ca.* 80 and 75% yields, respectively. The starting materials as well as the dyads were purified through column chromatography and recrystallization and characterized on the basis of spectroscopic and analytical evidences.

The UV-Visible absorption and fluorescence spectra of the dyads **1** and **2** have been studied in toluene solution and neat films, obtained by spin coating of solution in toluene on the quartz plates (Figure 2.1). A broad absorption peak at around 390 nm observed for the dyad **1**, which can be assigned to the charge transfer transition from the electron donating phenoxazine group to the electron

accepting oxadiazole moiety.[24] Interestingly, we observed negligible absorption at 390 nm and instead a new broad band having absorption in the region from 345 to 380 nm was observed, as the position of the phenoxazine moiety changed from the *para*- position (dyad **1**) to the *meta*- position (dyad **2**). These observations can be attributed to the decrease in conjugation between the donor and acceptor subunits in case of the dyad **2** owing to its *meta*- linkage, which is in agreement with the literature reports.[25]

When the emission properties were investigated in toluene, we observed green fluorescence having λ_{max} at 502 and 522 nm (excitation wavelength, λ_{exc} = 330 nm) for the dyads **1** and **2**, respectively. Similar to the solution, the thin film of **1** showed a broad and less intense absorption peak at around 390 nm and an intense peak at 338 nm (Figure 2.1A). Similar observations were made with the dyad **2,** whose spectrum showed peaks at 348 nm and 337 nm (Figure 2.1B). The emission maxima of the films of the dyads **1** and **2** were observed at 500 nm

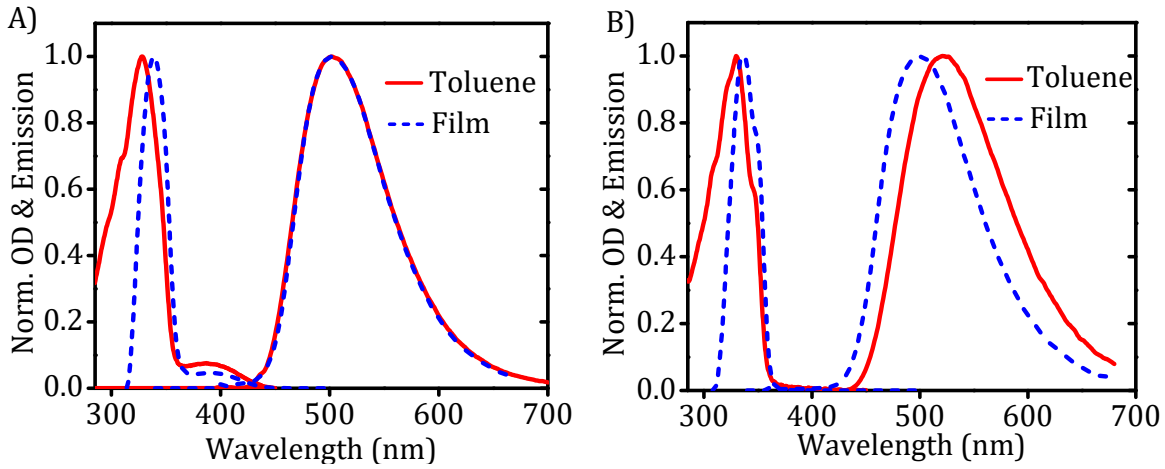

Figure 2.1. Normalized absorption and fluorescence spectra at 298 K of the dyads, A) dyad **1** and B) dyad **2** in toluene and thin film.

Table 2.1. Summary of the absorption and emission properties of the dyads **1** and **2** in toluene solution and film state. [a]

Dyad	Toluene solution			Film state	
	λ_{abs}[b] nm	ε_{max} [b] M^{-1} cm^{-1} x 10^4	λ_{ems}[b],nm (Φ_F)[b]	λ_{abs}[c] nm	λ_{ems}[c] , nm (Φ_F) [c]
1	390, 328	0.39, 5.17	502 (0.09±0.03)	395, 338	500 (0.25±0.02)
2	345, 330	3.29, 5.50	522 (0.001)	348, 338	500 (0.03)

[a] Average of more than three independent experiments, [b] measured in toluene and [c] measured using spin cast film. λ_{abs}: absorption wavelength; ε_{max}: molar extinction coefficient; λ_{ems}: emission wavelength; Φ_F: absolute quantum yield.

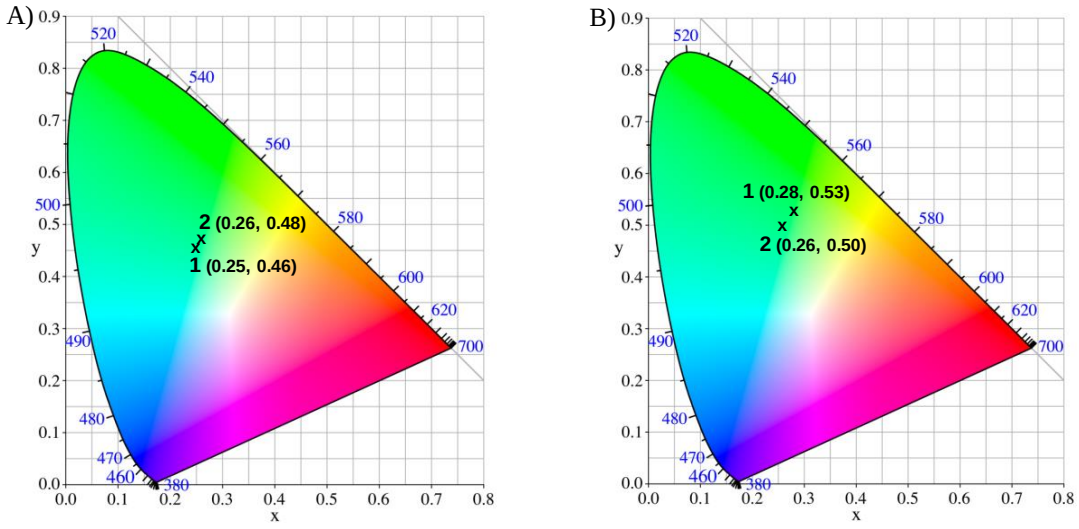

Figure 2.2. CIE chromaticity diagram of the dyads **1** and **2** corresponding to the emission spectra in (A) toluene and (B) thin film state.

(λ_{exc}, 330 nm). The higher Stokes shift observed for the dyads **1** and **2** can be attributed to the charge transfer excited state. The emission maxima of the dyad **1** in film matched with that observed for the toluene solution. This indicates that the dielectric constant of the film of **1** is close to that of toluene solution. In

addition, we have noticed a substantial decrease in the fluorescence quantum yields, when the position of the donor moiety changed from the *para*- (dyad **1**, Φ_F = 0.25) to *meta*- position (dyad **2**, Φ_F = 0.03). The calculated CIE coordinates of the dyads **1** and **2** were found to be (0.25, 0.46) and (0.26, 0.48) in toluene and (0.28, 0.53) and (0.26, 0.50) in the film, respectively, which are close to the pure green emission (Figure 2.2).[26]

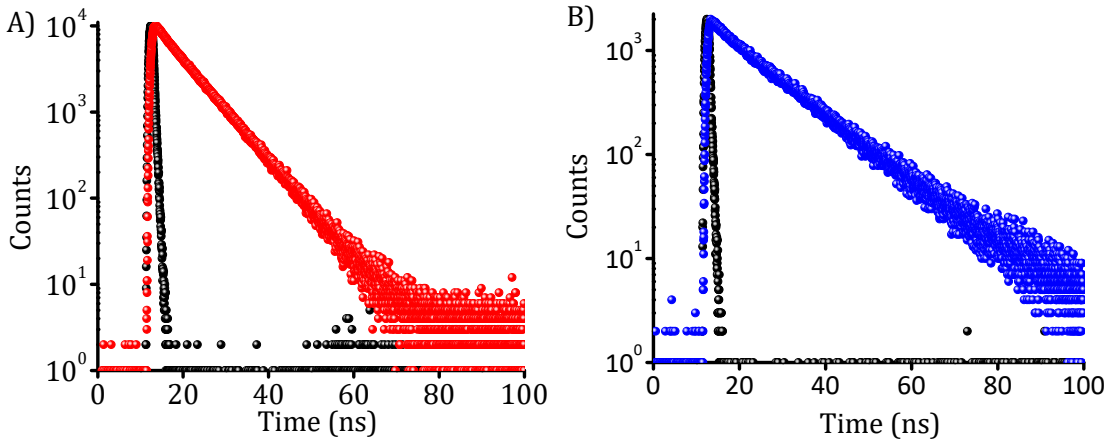

Figure 2.3. Fluorescence decay of A) dyad **1** and B) dyad **2** in toluene.

The fluorescence lifetimes of the dyads **1** and **2** were measured in toluene (Figure 2.3) and the results are summarized in Table 2.2. Both the dyads exhibited bi-exponential decay with a short lived minor component and a comparatively long-lived major component (τ_1 = 2.03 ns (3.67%) and τ_2 = 7.53 ns (96.33%) for the dyad **1**; τ_1 = 3.14 ns (4.42%) and τ_2 = 13.69 (95.58%) for the dyad **2**). The observed bi-exponential decay can be attributed to the presence of different conformers due to the existence of restricted rotation.[27] The rate constants of radiative (k_r) and non-radiative (k_{nr}) decay of the dyads were calculated according to Equations 2.1 and 2.2.[28]

$$k_r = \frac{\Phi_F}{\tau} \ldots\ldots\ldots\ldots \text{(Eq 2.1)}$$

$$k_{nr} = \frac{1 - \Phi_F}{\tau} \ldots\ldots\ldots\ldots \text{(Eq 2.2)}$$

Table 2.2. Summary of lifetime measurements in toluene.[a]

Dyads	τ (ns)	<τ> (ns)	k_r (10^7 S^{-1})	k_{nr} (10^7 S^{-1})
1	τ_1= 2.03 (3.67%) τ_2= 7.53 (96.33%)	6.85	2.63	11.97
2	τ_1= 3.14 (4.42%) τ_2= 13.69 (95.58%)	11.92	0.252	8.14

[a]Average of more than three experiments; <τ>: average fluorescence lifetime; τ: fluorescence lifetime; k_r and k_{nr}: rate constants of radiative and non-radiative transition, respectively.

To understand the effect of polarity, the absorption and emission spectra of dyads **1** and **2** were recorded in various solvents of differing polarity (Figure 2.4). Negligible changes in the absorption spectra with increasing solvent polarity (nonpolar cyclohexane to polar acetonitrile) were observed, which could be attributed to the small difference between the dipole moments of Franck–Condon excited and ground states of these dyads. In contrast, as the polarity of the solvent increased, we observed the broadening of the emission spectrum with a gradual increase in red shift. From the non-polar cyclohexane to polar acetonitrile, we observed a redshift of *ca.* 155 nm (5380 cm^{-1}) and 160 nm (5500 cm^{-1}) for the dyads **1** and **2**, respectively. These observations indicate that the solvent-solute interactions stabilize the intramolecular charge transfer excited states, yielding a dipole moment that is larger than that in the ground state. The

emission maximum (ν_{max}, in wavenumber) was plotted against the solvent polarity parameter $E_T(30)$[29] as shown in Figure 2.5A. These systems exhibited a positive solvatochromism with the emission maximum depending approximately linearly on the solvent polarity.

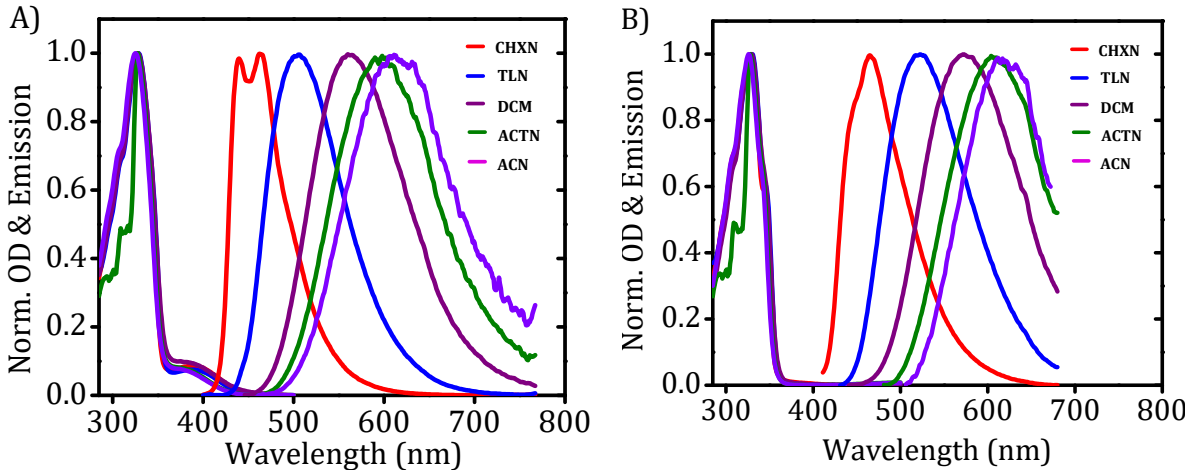

Figure 2.4. Normalized absorption and fluorescence spectra of the A) dyad **1** and B) dyad **2** in different solvents. Excitation wavelength, 330 nm.

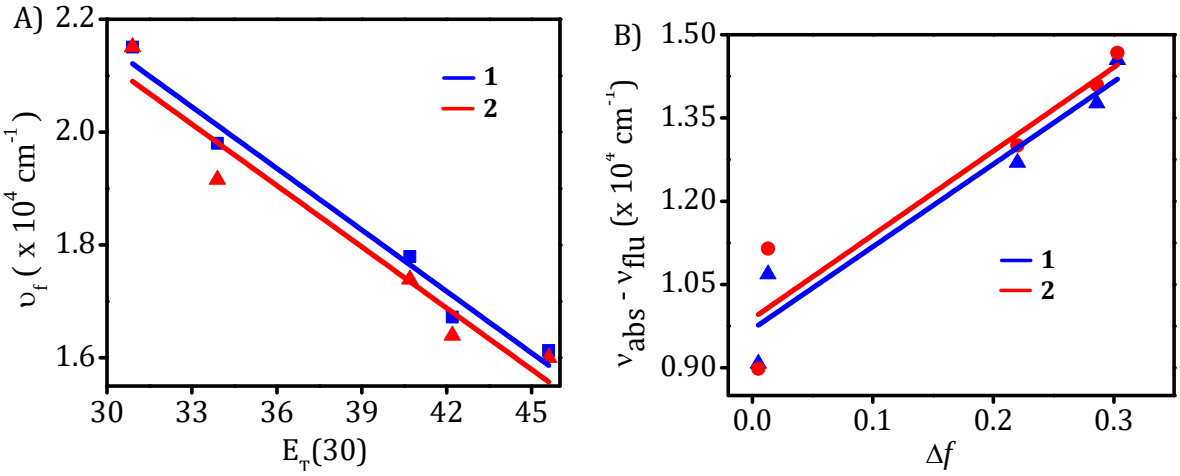

Figure 2.5. A) Plot of the emission maximum in different solvents *vs* solvent polarity parameter $E_T(30)$ and B) plot of Stokes shift against the solvent polarity (Δf). From the left, cyclohexane, toluene, dichloromethane, acetone and acetonitrile solutions and while the solid lines are least-squares fit.

Furthermore, the solvent polarity effect was analyzed in terms of the changes in the dipole moment (Δμ) between the ground (S_0) and excited states (S_1) using a Lippert–Mataga plot (Figure 2.5B).[30] From the changes in Stokes shift in different solvents (Table 2.3 and 2.4), the changes in the dipole moment was calculated using the equation (2.4), wherein, 'ν_{abs}' and 'ν_{flu}' are the absorption and fluorescence maxima of the dyads **1** and **2** in wave numbers, respectively, 'ε_0' is the vacuum permittivity, 'h' is the Plank's constant, 'c' is the speed of light and 'a' is the Onsager cavity radius, which was *ca.* 6.36 and 6.31 Å for the dyads **1** and **2**, respectively, as determined from DFT calculations using Gaussian 09**.** The term Δ*f*, known as the solvent polarity parameter was obtained by the equation 2.3,

$$\Delta f = ((\varepsilon-1)/(2\varepsilon+1)) - ((n^2-1)/(2n^2+1)) \quad \text{..... (Eq. 2.3)}$$

wherein, ε is the dielectric constant and n is the refractive index of the solvent. The Stokes shift for emissions changed linearly with Δ*f* as shown in Figure 2.5B. Using the slope value of *ca.* 14874 and 15098 cm^{-1} for the dyads **1** and **2**, respectively, and equation 2.4, we have estimated the changes in dipole moment (Δμ), which is found to be *ca.* 19.51 and 19.42 D for the dyads **1** and **2**, respectively. The calculated dipole moment for the ground states obtained from DFT calculations are *ca.* 4.68 and 1.91 D while the dipole moment of the charge transfer states obtained by the solvatochromic method are *ca.* 24.19 and 21.33 D for the dyads **1** and **2,** respectively. These results clearly indicate that the high dipole moment of the charge transfer states is responsible for the solvent polarity dependent red shifted emission observed for the dyads, which is in agreement with the literature reported examples.[31]

Table 2.3. Absorption and emission properties of dyad **1** in different solvents. [a]

Solvents	ε	n	Δ*f*	λ_a (nm)	ν_a (cm^{-1})	λ_F (nm)	ν_F (cm^{-1})	$\nu_a - \nu_F$ (cm^{-1})
CHXN	2.02	1.43	0.005	327,390	30581.0	465	21505.4	9075.6
TLN	2.38	1.49	0.013	328, 390	30487.8	505	19801.9	10685.8
DCM	9.10	1.42	0.220	328, 380	30487.8	562	17793.6	12694.2
ACTN	21.00	1.36	0.286	328, 373	30487.8	598	16722.4	13765.4
ACN	37.50	1.35	0.303	326, 372	30674.8	620	16129.0	14545.7

[a]Average of more than three independent experiments; ε: dielectric constant; n: refractive index; Δ*f*: solvent polarity parameter; λ_a: absorption wavelength; ν_a: wave number corresponds to absorption maximum; λ_F: fluorescence wavelength, ν_F: wave number corresponds to fluorescence maximum.

Table 2.4. Absorption and emission properties of dyad **2** in different solvents. [a]

Solvents	ε	n	Δ*f*	λ_a (nm)	ν_a (cm^{-1})	λ_F (nm)	ν_F (cm^{-1})	$\nu_a - \nu_F$ (cm^{-1})
CHXN	2.02	1.43	0.005	328,345	30487.8	465	21505.38	8982.4
TLN	2.38	1.49	0.013	330, 345	30303.0	522	19157.09	11145.9
DCM	9.10	1.42	0.220	329, 343	30395.1	575	17391.30	13003.8
ACTN	21.00	1.36	0.286	328, 341	30487.8	610	16393.44	14094.4
ACN	37.50	1.35	0.303	326, 340	30674.8	625	16000.00	14674.8

[a]Average of more than three independent experiments; ε: dielectric constant; n: refractive index; Δ*f*: solvent polarity parameter; λ_a: absorption wavelength; ν_a: wave number corresponds to absorption maximum; λ_F: fluorescence wavelength; ν_F: wave number corresponds to fluorescence maximum.

$$\nu_{abs} - \nu_{flu} = \frac{1}{4\pi\varepsilon_0}\frac{2\Delta\mu^2}{hca^3}\Delta f + \text{constant} \ldots\ldots\ldots\ldots (\text{Eq } 2.4)$$

Further, we have recorded phosphorescence spectra (delayed by 10 ms) of the dyads **1** and **2** in toluene at 77 K and observed a great overlap with their corresponding fluorescence spectra (Figure 2.6). The triplet energy was determined for both the conjugates from the onset values of corresponding phosphorescence spectrum and the value was found to be *ca.* 2.56 eV for both the dyads. In addition, a small energy difference (ΔE_{ST}) of *ca.* 0.26 and 0.19 eV was observed between the singlet and triplet excited states of the dyads **1** and **2**, respectively, thereby indicating their use as efficient TADF emitters. To understand the TADF properties, we have compared the photoluminescence efficiency of these molecules in air saturated toluene with the oxygen free toluene (by freeze-thaw degassing). For both the conjugates **1** and **2**, we observed an increase in the fluorescence intensity and quantum yields after freeze-thaw degassing of the solutions (Figure 2.7 and Table 2.3). These observations can be attributed to the quenching of the triplet excited states by the dissolved oxygen present in toluene, and the concentration of which is negligible under freeze-thaw degassing conditions. The dyad **2**, which has a lower ΔE_{ST} value of 0.19 eV and correspondingly, showed *ca.* 80% enhancement in the PLQYs intensity, whereas the dyad **1** with a relatively higher ΔE_{ST} value of 0.26 eV, exhibited the low enhancement of *ca.* 64%, in the emission after the removal of oxygen. After removal of oxygen, the fluorescence quantum yields of the dyads **1** and **2** were increased from 0.09 to 0.18 and 0.001 to 0.03 respectively. In addition, we have recorded the delayed fluorescence of the dyads after a delay time of 60 μs in toluene solution (Figure 2.8).

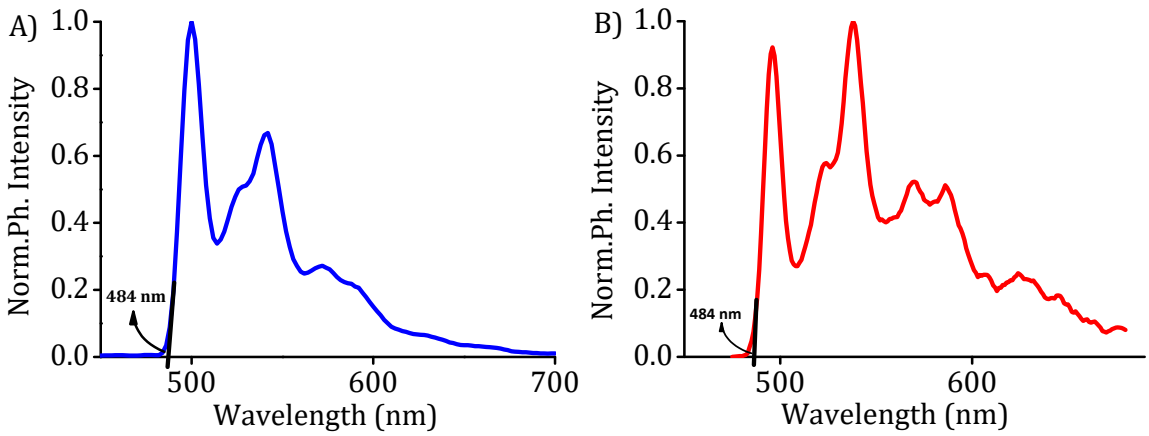

Figure 2.6. Normalized phosphorescence spectra of dyad **1** (A) and **2** (B) in toluene solution at 77K.

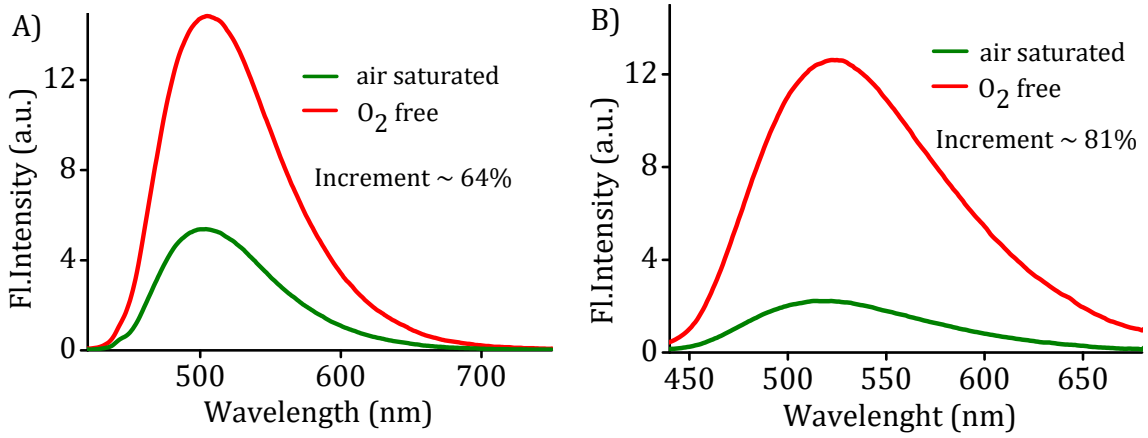

Figure 2.7. Fluorescence intensity changes before and after purging with nitrogen in toluene (10 μM each) solution for the dyads, A) **1** and B) **2** (λ_{exc}, 350 nm).

Table 2.5. Delayed fluorescence properties of dyads **1** and **2** in toluene.

Dyads	ΔE_S (eV)	ΔE_T (eV)	ΔE_{ST} (eV)	Φ_{F+DF}
1	2.82	2.56	0.26	0.18
2	2.75	2.56	0.19	0.03

E_S and E_T: energy of singlet and triplet excited state; Φ_{F+DF}: fluorescence quantum yield in O_2 free toluene solution.

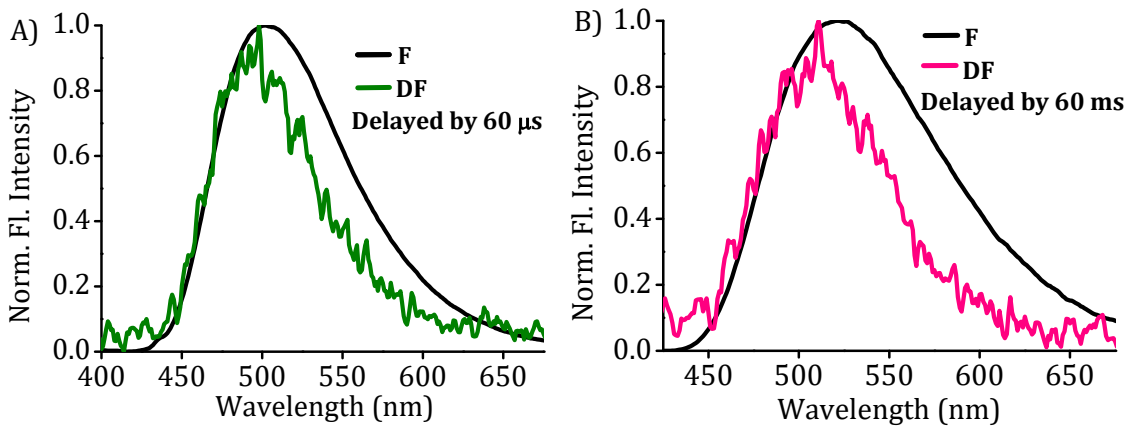

Figure 2.8. Prompt (F) and delayed fluorescence (DF) of the (A) dyad **1** and (B) dyad **2** in toluene solution (10 μM each) at 298 K.

2.3.2. Electrochemical, thermal and morphological analysis

Cyclic voltammetric measurements were performed for dyads **1** and **2** in dry dichloromethane with 0.1 M tetrabutylammonium hexafluorophosphate ($Bu_4N^+PF_6^-$) as the supporting electrolyte, under an argon atmosphere. These dyads showed reversible oxidation waves due to the presence of electron donating phenoxazine group and the oxidation potentials *vs* Ag/Ag^+ were measured to be *ca.* 0.82 and 0.81 V for the dyads **1** and **2**, respectively (Figure 2.9). The redox potential of Fc/Fc^+ (standard value = 4.8 eV with respect to vacuum) was observed at 0.43 V. Based on this, the HOMO energy levels of molecules were estimated using the equation $E^{HOMO} = - E^{ox} - 4.37$ eV, while the LUMO energy levels were obtained from the band gap energies (estimated from the onset wavelengths of the UV absorptions) and the values are tabulated in Table 2.6.[32]

The stability of the dyads was investigated by using thermogravimetric analysis (TGA) (Figure 2.10) and both these dyads were found to be thermally quite stable. The decomposition temperature (T_d), defined as the temperature at which 5% mass loss occurs of the dyads **1** and **2** were determined and the values

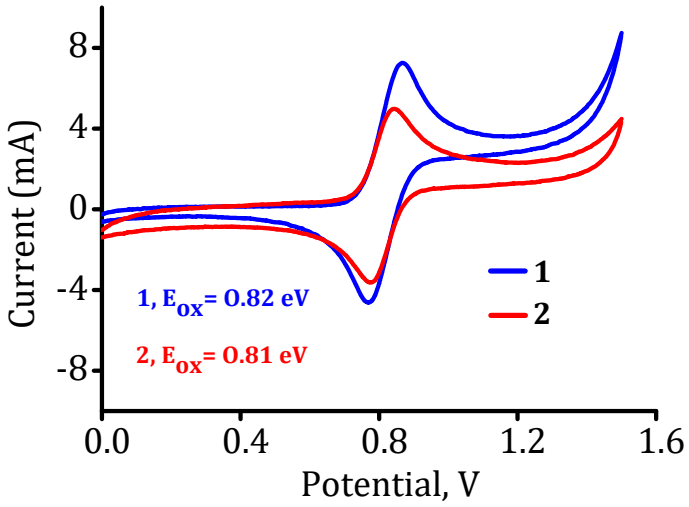

Figure 2.9. Cyclic voltammograms recorded for the dyads **1** and **2** in dry dichloromethane (1 mM solutions; scan rate, 100 mV S^{-1}).

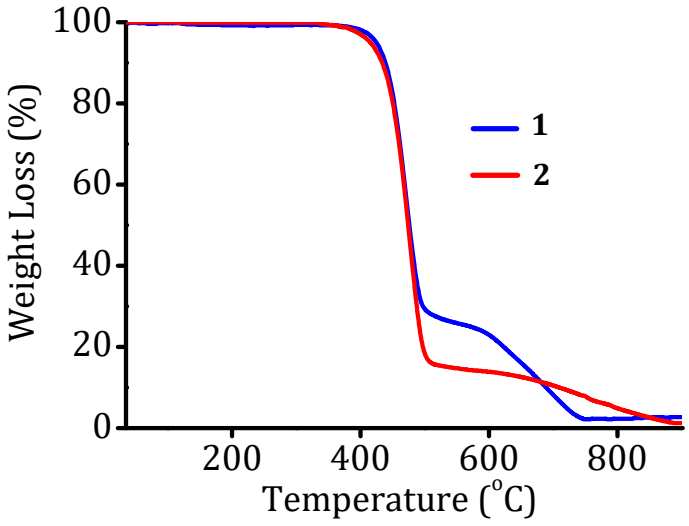

Figure 2.10. Thermogram of the dyads **1** and **2** in N_2 atmosphre at a heating rate of 10 ^{0}C min^{-1}.

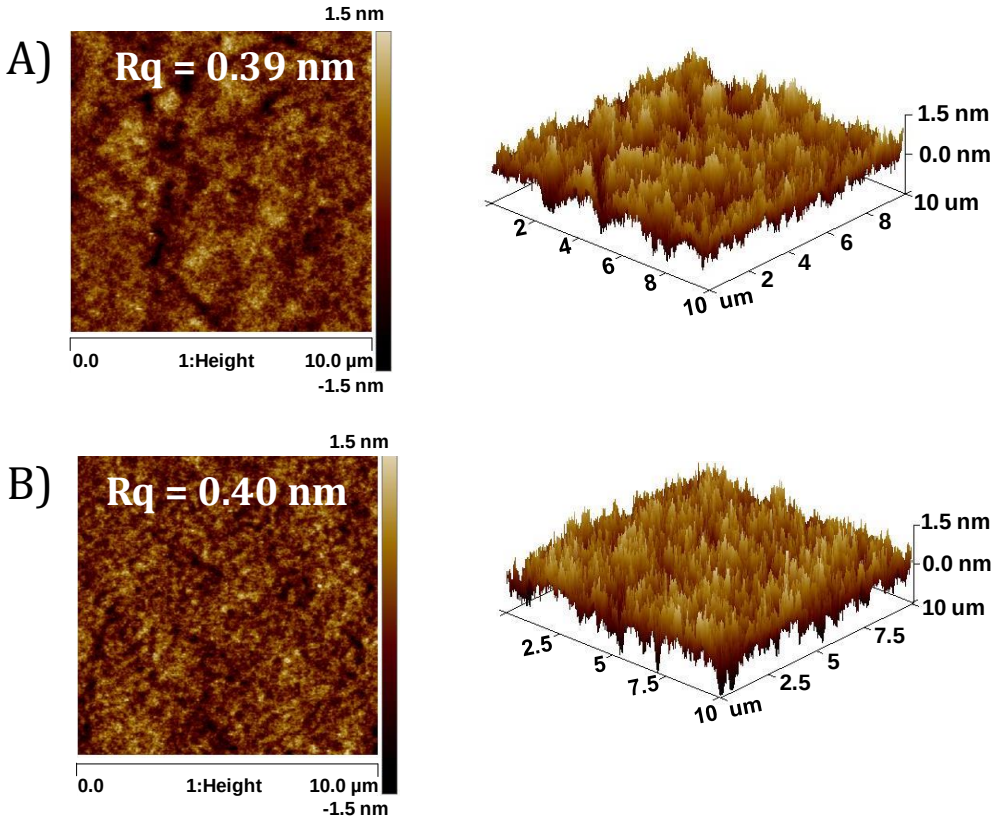

Figure 2.11. A) AFM images of solution processed A) **1** and B) **2** on ITO plate.

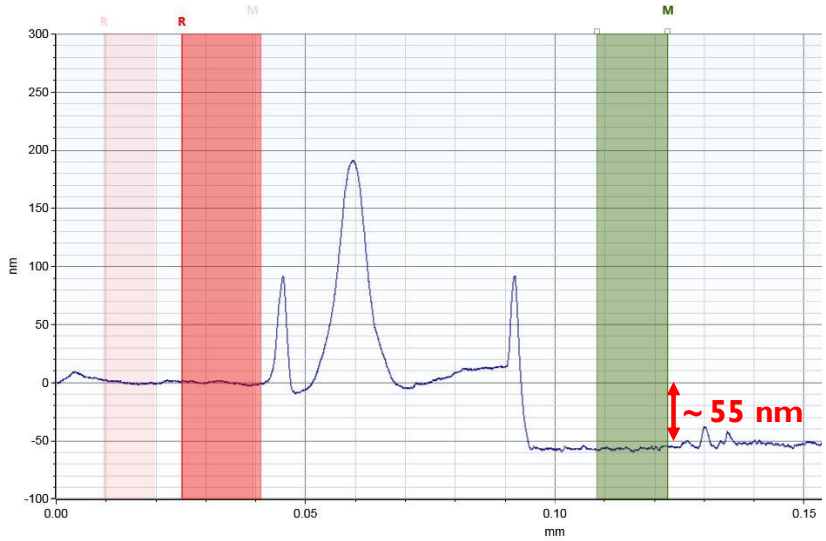

Figure 2.12. Profilogram of the spin casted film of dyad **1** on glass substrate.

were found to be *ca.* 425 and 412 °C and the melting points of the systems are *ca.* 119 and 134 °C, respectively. The thin film forming properties were investigated through atomic force microscopy (AFM).[33] The AFM images of solution processed films of thickness ~55 nm (Figure 2.12) showed homogeneous film morphologies with very small values of root mean square (RMS) roughness of *ca.* 0.39 and 0.40 nm for the dyads **1** and **2,** respectively (Figure 2.11). These results demonstrate that both the dyads exhibit good film forming ability.

2.3.3. Theoretical calculations

The geometry of the dyads **1** and **2** were optimized using B3LYP/6-311G (d,p) level density functional theory. In the cases of **1** and **2**, the dihedral angles (θ_d) between the donor moiety (phenoxazine unit) and the adjacent phenyl ring are *ca.* 88.5^o and 89.2^o, respectively. In these dyads, a planar orientation of the donor moiety with respect to the plane of the N-connected phenyl ring is not possible as this would lead to close proximity between C-H bonds of the phenyl rings of the donor moiety and N- connected phenyl ring. In other words, the non-bonded H...H interactions (steric repulsion) is responsible for the observed twisted configurations. In Figure 2.13, the HOMO and LUMO of the dyads **1** and **2** are depicted using isosurface value 0.03. Since the phenoxazine moiety is nearly orthogonal to the N-connected phenyl ring, the HOMO is seen exclusively centred on the donor moiety and LUMO on the acceptor moiety. A complete separation of HOMO and LUMO is responsible for the observed lower radiative transition. The

calculated HOMO/LUMO values are 5.07/2.17 eV for the dyad **1** and 5.08 /2.14 eV for the dyad **2** and these values were found to be in reasonably agreement with the experimentally estimated values.

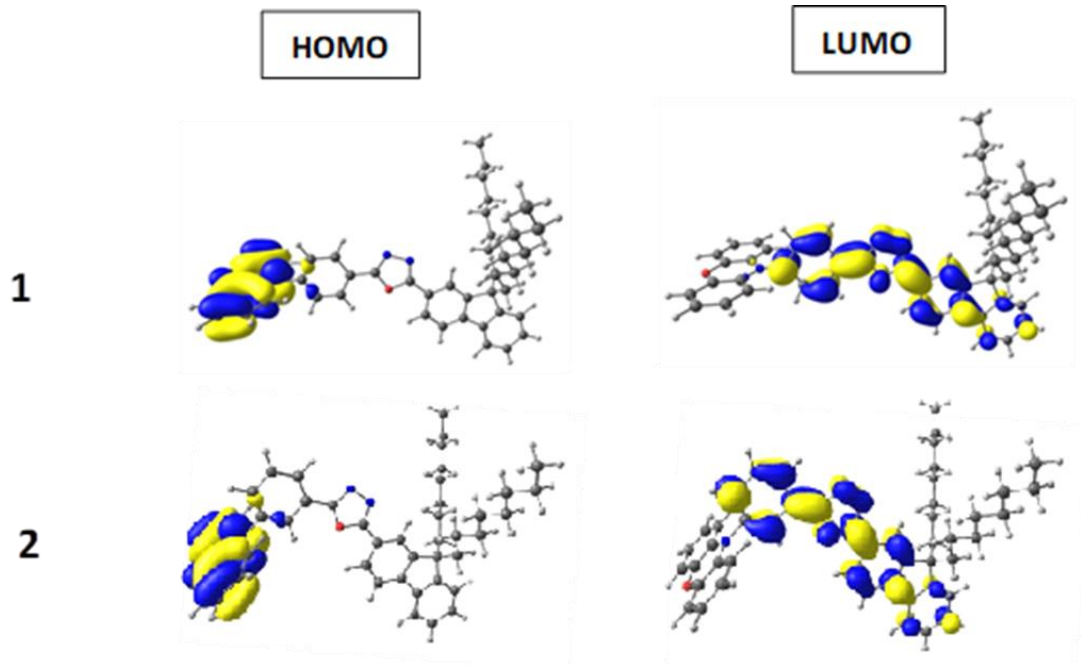

Figure 2.13. HOMO and LUMO of the dyads **1** and **2** calculated at the B3LYP/6-311G (d,p) level.

Table 2.6. Physical and electrochemical data of the dyads **1** and **2**.

Dyads	HOMO/LUMO /ΔE_{gap} (eV)[a]	HOMO/LUMO /ΔE_{gap} (eV)[b]	θ_d[b] (^oC)	Mp/T_d ($^\circ C$)
1	5.19/2.27/2.92	5.07/2.17/2.9	88.5	119 / 425
2	5.18/1.74 /3.44	5.08/2.14/2.94	89.2	134 / 412

[a]Experimentally determined and [b]theoretically calculated. E_{gap}: band gap; θ_d: dihedral angle; Mp: melting point; T_d: decomposition temperature.

2.3.4. Device fabrication

To study the utility of the dyads **1** and **2** in device applications, un-doped OLEDs were fabricated with device configuration (Figure 2.14) having indium tin oxide (ITO) (120 nm)/ Poly(3,4-ethylene-dioxythiophene) poly(styrenesulfonate) (PEDOT: PSS) (40 nm)/ dyad **1** or **2** (50 nm)/ 1,3,5-tris(N-phenylbenzimidazol-2-yl)- benzene (TPBi) (40 nm)/ LiF(1 nm)/ Al (100 nm). Here, ITO was used as a transparent anode, PEDOT:PSS as the hole injection layer (HIL), TPBi as the hole-blocking layer (HBL), LiF (lithium fluoride) as the electron-injecting layer (EIL) while Al (aluminium) acts as a cathode.

The dyads **1** and **2** showed green electroluminescence (EL) having λ_{max} at 504 nm and 505 nm (Figure 2.15A) with CIE coordinates of (0.26, 0.49) and (0.27, 0.47), respectively (Figure 2.16). The EL spectra of devices were similar to the photoluminescence spectra of the spin coated films. Good diode behaviour

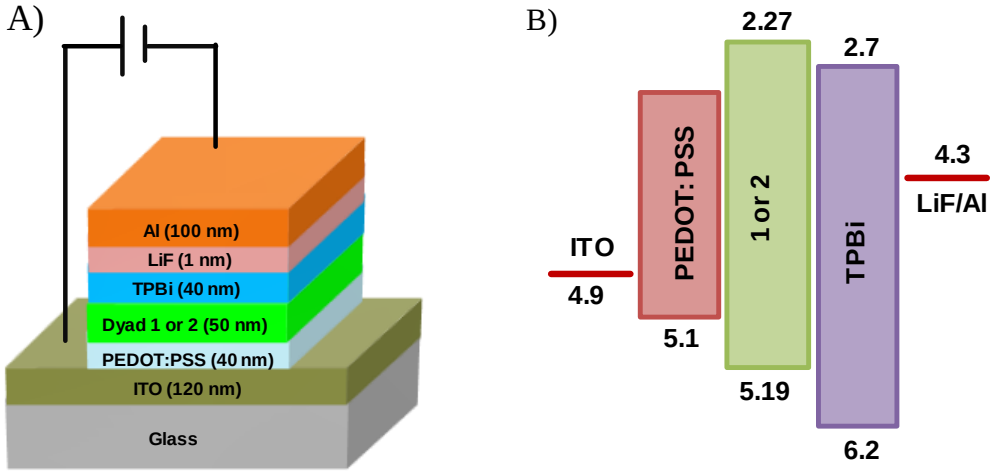

Figure 2.14. Device structure (A) and energy level diagram of the OLEDs fabricated using the dyads **1** and **2**.

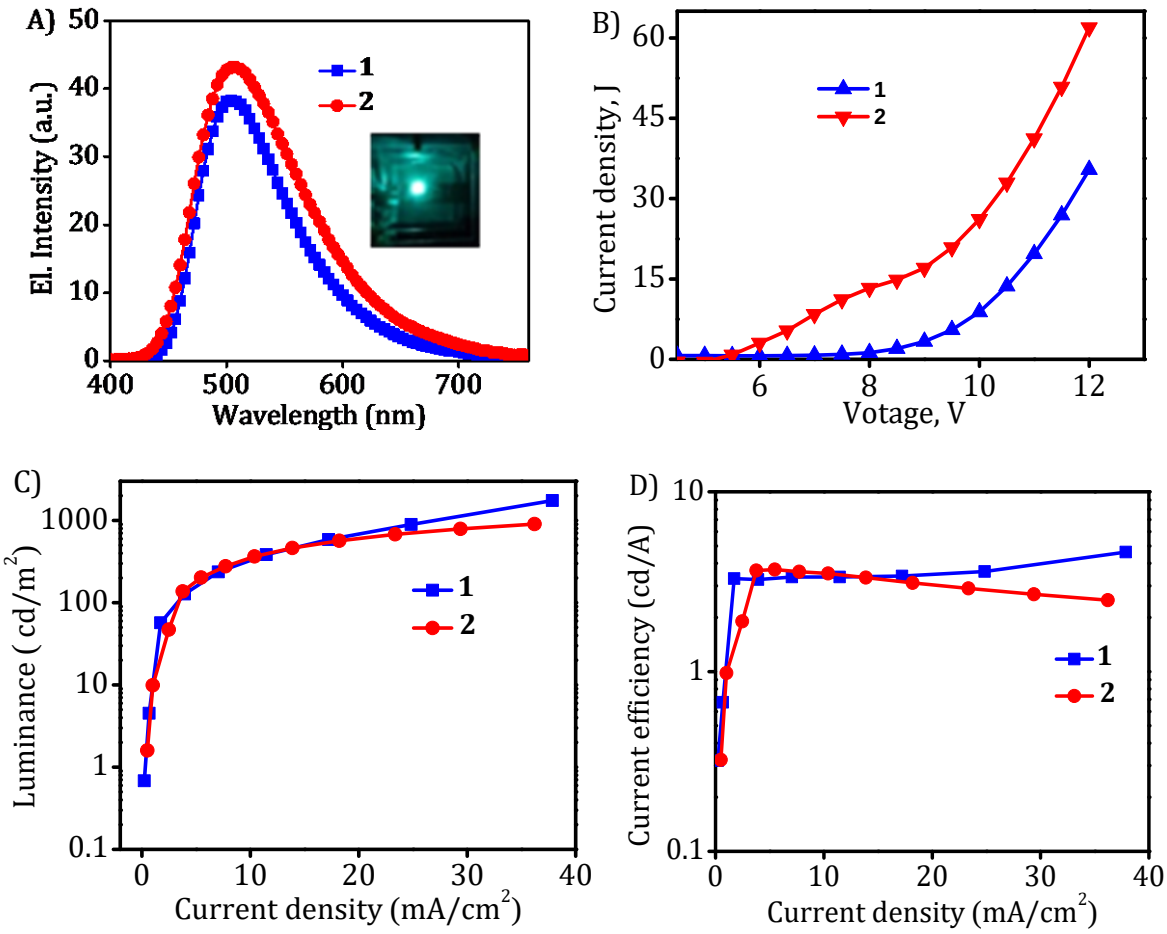

Figure 2.15. A-E) Device characteristics of the un-doped solution processed OLEDs fabricated using the dyads **1** and **2**. Inset shows the photograph of electroluminescence from the fabricated device using the dyad **1.**

was observed for the fabricated devices, which is shown in Figure 2.15B. The turn on voltage (V_{onset}) for these systems is found to be *ca.* 5.5-6 V. The dyad **1** showed a highest luminance of *ca.* 1751 cd m^{-2} with a current efficiency of *ca.* 4.63 cd A^{-1}. In the case of dyad **2** having phenoxazine in the *meta*- position, a comparatively lower luminance of 903.5 cd m^{-2} with a current efficiency of 3.65 cd A^{-1} was observed. This observation is in accordance with the observed higher fluorescence quantum yield of the dyad **1**. The current density – luminance, and

current density - current efficiency characteristics of OLEDs with dyads **1** and **2** are shown in Figures 2.15C and 2.15D and the values are tabulated in Table 2.7. The efficiency of the devices that incorporated the dyad **1** was found to be superior when compared to that of the dyad **2** derivatives and which confirms the importance of the nature and position of the substitution in these dyads.

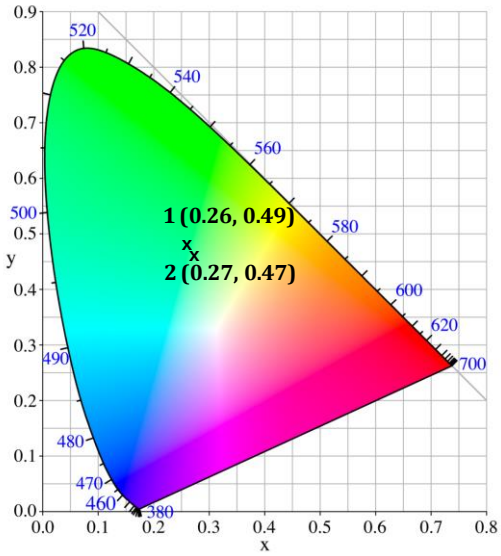

Figure 2.16. CIE coordinates of the emission from devices **1** and **2.**

Table 2.7. Electroluminescence data of the dyads **1** and **2** in OLED device.

Device	V_{onset} (V)	λ_{ems}	CIE coordinates	L_{max} (cd m^{-2})	η_c (cd A^{-1})	η_p (lm W^{-1})
1	5.98	504	(0.26, 0.49)	1751.0	4.63	1.26
2	5.52	505	0.27, 0.47)	903.5	3.65	1.04

V_{onset}: turn-on voltage; λ_{ems}: emission wavelength; L_{max}: maximum luminance; η_c: maximum current efficiency measured; η_p: maximum power efficiency measured. Applied voltage in each case was in the range 11-11.5 V.

2.4. Conclusions

In summary, we have synthesized new green fluorescent organic D-π-A dyads **1** and **2** having a phenoxazine donor and an oxadiazole acceptor coupled through a *para*- or *meta*- phenyl spacer and investigated their photophysical, thermal, electrochemical and morphological properties including their OLED properties. Both the dyads **1** and **2** showed favorable photophysical properties and excellent thermal stability, solution processability and film morphologies. The solution processed un-doped green OLEDs fabricated based on these dyads showed CIE coordinates of (0.26, 0.49) and (0.27, 0.47) for the dyads **1** and **2**, respectively, as green emitters with a luminance of *ca.* 1751 cd m^{-2} for the dyad **1** and 903.5 cd m^{-2} for dyad **2** thereby demonstrating their potential use in various optoelectronic applications including in OLEDs.

2.5. Experimental Section

2.5.1. General techniques

The melting points were determined on a Mel-Temp II melting point apparatus. The electronic absorption spectra were recorded on a Shimadzu UV-3101 or 2401 PC UV-VIS-NIR scanning spectrophotometer. The fluorescence spectra were recorded on a SPEX-Fluorolog F112X spectrofluorimeter. Film-state photoluminescence was measured using the front face emission scan mode on a SPEX Fluorolog F112X spectrofluorimeter.[34] Measurements of solution state and film state fluorescence quantum efficiency were carried out using a calibrated integrating sphere in a SPEX Fluorolog spectrofluorimeter. A Xenon-arc lamp was

used to excite the film samples placed in the sphere, with 330 nm as the excitation wavelength. The integrating sphere system was calibrated using the solid state fluorescence quantum yield of the standard sodium salicylate (white powder) was determined to be 60 ± 10%, which is consistent with previously reported values.[35] Fluorescence lifetimes were measured using an IBH (Fluoro Cube) time correlated picosecond single photon counting (TCSPC) system. The phosphorescence spectra and time resolved studies of delayed fluorescence were carried out using a 1040D phosphorimeter with a pulsed lamp.

The CIE, Commission International de l'Eclairage (International Commission on Illumination), chromaticity coordinates (1931) (x, y) were calculated using HORIBA Jobin Yvon Color Calculator provided with integrating sphere. Thermal stability measurements were performed at a heating rate of 10°C/min in a nitrogen atmosphere using Shimadzu, DTG-60 equipment. Cyclic voltammetry is done by CV-50w electro analyzer in DCM using Pt wire as auxiliary electrode, glassy carbon as working electrode. The potential was referenced to the standard Ag/AgCl electrode and ferrocene was used as external standard. ^{1}H NMR was recorded on a 500 MHz Bruker advanced DPX spectrometer. Mass spectra were recorded either on a JEOL AX503 (HRMS) or Shimadzu Biotech Axima CFR plus instrument. The AFM studies were carried out Bruker nanoscope V multimode 8 AFM. All experiments were carried out at room temperature (25±1 °C), unless otherwise mentioned.

The geometry of the dyads **1** and **2** was optimized with B3LYP/6-311G (d,p) level density functional theory[36] in conjunction with polarized continuum

model (PCM)[37] solvation method (selected solvent is toluene) as implemented in Gaussian 09 package. Vibrational frequency calculations were carried out on **1** and **2** at the same level of theory and verified them as true minima on the potential energy surface (number of imaginary frequency = 0).

The electroluminescence properties of the molecules were studied by fabricating un-doped OLEDs by solution processing. The ETL and cathode were deposited using thermal evaporation at a base pressure of 10^{-8} Torr. Patterned ITO coated glass substrates with a sheet resistance of 10 Ω/sq were used as anodes, which were cleaned with detergent, chloroform, isopropanol and de-ionized water and UV–Ozone treated. On the ITO substrate, the HIL, emitting layer, ETL, EIL, and cathode were deposited sequentially without exposing to atmosphere inside a glove box. The deposition rate of TPBi and Al was maintained at 2 Å s^{-1}, whereas the deposition rates of LiF were 0.1 Å s^{-1}. The deposition rate and thickness of the deposited layers were controlled *in situ* by a quartz crystal thickness monitor. The cathode was deposited on the top of the structure through a shadow mask. The devices were encapsulated using UV curable epoxy inside the glove box. The EL spectra and J–V characteristics were measured using a spectrophotometer and a source meter interfaced to a computer. All the measurements were carried out at room temperature.

2.5.2. Materials and methods

All the reagents used for synthesis and measurements were purchased from Sigma Aldrich or Alfa Aesar, in analytical grade and used as received, unless otherwise stated. TPBi was purchased from LumTec and Aluminium from Kurt J. Lesker.

2.5.3. Synthesis and characterization

Bromo-9H-fluorene (3). To a stirred solution of fluorene (1 g, 6.02 mmol) and 48% HBr (1 mL, 6.02 mmol) in CH_2Cl_2-H_2O (9:1, 20 mL), 30% H_2O_2 (0.68 mL, 6.02 mmol) was slowly added over a period of 15 min at 10-15 °C. The reaction was left at room temperature for 15 h whilst monitoring its progress by TLC. After the reaction, solvent was removed under reduced pressure and the crude product was added to ethyl acetate and washed with water, brine and dried over anhydrous Na_2SO_4. The pure product was isolated by silica gel column chromatography, (1.08 g, 73%), mp 112-114 °C; ^{1}H NMR (500 MHz, $CDCl_3$, TMS) δ 3.86 (s, 2H), 7.31 (m, 1H), 7.36 (t, 1H, J = 7 Hz), 7.47 (m, 1H), 7.52 (d, 1H, J = 7.5 Hz), 7.62 (d, 1H, J = 8 Hz), 7.65 (s, 1H), 7.74 (d, 1H, J = 7.5 Hz).

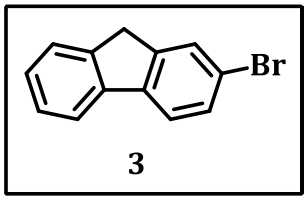

3

2-Bromo-9,9-dioctyl-9H-fluorene (4). A solution of 2-bromofluorene (1g, 4.08 mmol) in DMSO (15 mL) was degassed by purging with argon for 30 min, and then benzyl triethyl ammonium chloride and aq. NaOH (0.818 g, 20.4 mmol) were added. After 10 minute the reaction mixture turned to red, octyl bromide

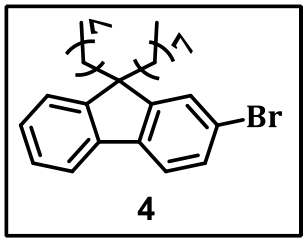

4

(2.85 mL) was added and the reaction mixture was heated to 80 °C for 4 h. The reaction mixture was subsequently cooled to room temperature, poured in to DCM and washed with H_2O. The organic layer was separated and dried over anhydrous Na_2SO_4 and solvent was removed by vacuum evaporator. The pure compound was isolated by silica gel column chromatography, (1.7 g, 89%); ^{1}H NMR (500 MHz, $CDCl_3$, TMS) δ 0.59 (s, 4H), 0.81 (t, 6H, J = 7 Hz), 1.08 (m, 8H), 1.12 (m, 8H), 1.19 (m, 4H), 1.93 (m, 4H), 7.32 (d, 3H, J = 9.5 Hz), 7.44 (d, 2H, J = 8 Hz), 7.55 (d, 1H, J = 8 Hz), 7.65 (d, 1H, J = 4.5 Hz).

9,9-Dioctyl-9H-fluorene-2-carbonitrile (5). 2-Bromo-9,9-dioctyl-9H-fluorene

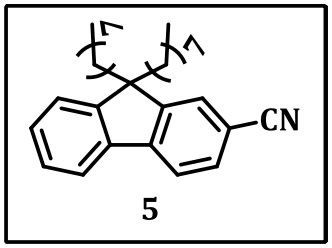

5

(1g, 2.13 mmol) was dissolved in NMP (15 mL) and then CuCN (0.572 g, 6.39 mmol) was added and refluxed overnight. After completing the reaction, 1 g of $FeCl_3$ in 10 mL of 10% HCl was added and stirred for 0.5 h at 120 °C. Then, the reaction mixture was cooled to room temperature and extracted twice with toluene. The combined extract was washed with 6N HCl, H_2O, and then with 10% NaOH solution. The organic part was dried and column chromatography was performed, (0.625 g, 70%); ^{1}H NMR (500 MHz, $CDCl_3$, TMS) δ 0.56 (t, 4H, J = 7 Hz), 0.81 (t, 6H, J = 7 Hz), 1.08 (m, 8H), 1.13 (m, 8H), 1.20 (m, 4H), 1.96 (m, 4H), 7.38 (m, 3H), 7.62 (d, 1H, J = 9.5 Hz), 7.65 (d, 1H, J = 8.5 Hz), 7.75 (t, 2H, J = 8.5 Hz); ESI-MS: Calcd for $C_{30}H_{41}N$, 415.32; Found, 416.33 (M^+).

5-(9,9-Dioctyl-9H-fluoren-2-yl)-2H-tetrazole (6). To a mixture of 9,9-Dioctyl-9H-fluorene-2-carbonitrile (1 g, 2.4 mmol) and NaN_3 (0.312 g, 4.8 mmol) in dry toluene (15 mL), Bu_3SnCl (1.3 mL, 4.8 mmol) was added. Then, the mixture was stirred and refluxed for 24 h. After cooling to room temperature, the above solution was poured to DCM and extracted with water and the organic layer was dried and column chromatography was carried out to give the product (0.75 g, 70%), ^1H NMR (500 MHz, $CDCl_3$, TMS) δ 0.56 (t, 4H, J = 7 Hz), 0.81 (t, 6H, J = 7 Hz), 1.08 (m, 8H), 1.13 (m, 8H), 1.20 (m, 4H), 1.96 (m, 4H), 7.37 (s, 3H), 7.74 (t, 1H, J = 4.5 Hz), 7.87 (d, 1H, J = 8 Hz), 8.16 (d, 1H, J = 8Hz), 8.23 (s, 1H) ESI-MS: Calcd for $C_{30}H_{42}N_4$, 458.34; Found, 459.34 (M^+).

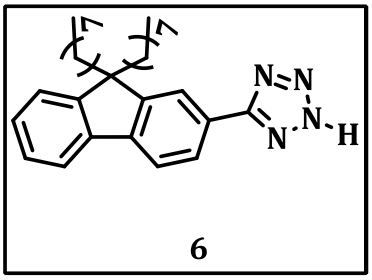

6

2-(4-Bromophenyl)-5-(9,9-dioctyl-9H-fluoren-2-yl)-1,3,4-oxadiazol (7a). A solution of *p*-Bromobenzoyl chloride (0.717 g, 3.27 mmol) was added drop wise to a solution of tetrazol (1 g, 2.18 mmol) in pyridine (20 mL) and refluxed for 2 h under argon. The reaction mixture was then cooled to room temperature prior to being poured into methanol with stirring to precipitate the product. (1 g, 75%), mp = 72-74 °C, ^1H NMR (500 MHz, $CDCl_3$, TMS) δ 0.60 (m, 4H), 0.78 (t, 6H, J = 7 Hz), 1.08 (m, 16H), 1.15 (m, 4H), 2.03 (m, 4H), 7.38 (t, 3H, J = 2.5 Hz), 7.70 (m, 2H), 7.77 (m, 1H), 7.84 (t, 1H, J = 4.5 Hz), 8.06 (m, 2H, 8.09 (t,

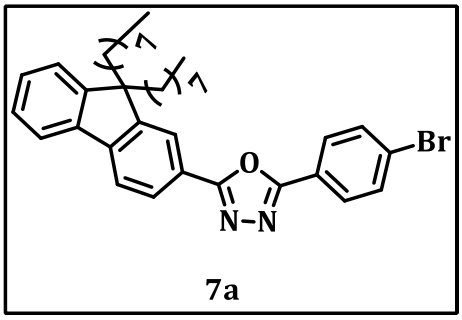

7a

2H, J = 2.5 Hz). ^{13}C NMR (125 MHz, $CDCl_3$) 165.50, 163.72, 151.69, 151.44, 145.04, 139.81, 132.44, 128.36, 127.08, 126.33, 126.08, 123.01, 121.97, 121.33, 120.48, 120.23, 55.50, 40.28, 31.74, 29.94, 29.21, 29.16, 23.76, 22.56, 14.03. ESI-MS: Calcd for $C_{37}H_{45}BrN_2$, 612.27; Found, 613.27 (M^+).

2-(3-Bromophenyl)-5-(9,9-dioctyl-9H-fluoren-2-yl)-1,3,4-oxadiazole (7b). A solution of m-Bromobenzoyl chloride (0.717 g, 3.27 mmol) was added dropwise to a solution of tetrazol (1 g, 2.18 mmol) in pyridine (20 mL) and refluxed for 2 h under argon. Then, the mixture was cooled to room temperature prior to being poured in to methanol with stirring to precipitate the product (1 g, 69%), mp = 77-79 °C, ^{1}H NMR (500 MHz, $CDCl_3$, TMS) δ 0.62 (t, 4H, J = 7 Hz), 0.80 (t, 6H, J = 7 Hz), 1.08 (m, 16H), 1.18 (m, 4H), 2.08 (m, 4H), 7.38 (d, 3H, J= 9.5 Hz), 7.43 (t, 1H, J = 8 Hz), 7.70 (d, 1H, J = 8 Hz), 7.77 (t, 1H, J = 4 Hz), 7.85 (d, 1H, J = 8 Hz), 8.12 (t, 3H, J = 9 Hz), 8.33 (s, 1H). ^{13}C NMR (125 MHz, $CDCl_3$) 165.63, 163. 12, 151.71, 151.44, 145.11, 139.79, 134.60, 130.67, 129.72, 128.40, 127.08, 126.14, 125.90, 125.52, 123.13, 123.05, 121.85, 121.36, 120.50, 120.25, 55.51, 40.28, 31.74, 29.94, 29.21, 29.17, 23.76, 22.56, 14.04. ESI-MS: Calcd for $C_{37}H_{45}BrN_2$, 612.27; Found, 613.27 (M^+).

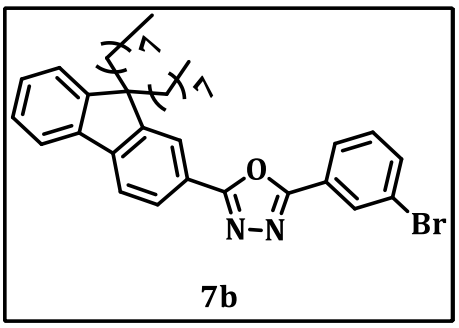

7b

10-(4-(5-(9,9-Dioctyl-9H-fluoren-2-yl)-1,3,4-oxadiazol-2-yl)phenyl)-10H-phenoxazine (1). A mixture of **7a** (1 g, 1.633 mmol), phenoxazine (0.448 g, 2.45 mmol), Cs_2CO_3 (1.596 g, 4.899 mmol), $Pd(OAc)_2$ (37 mg, 0.1633 mmol) and

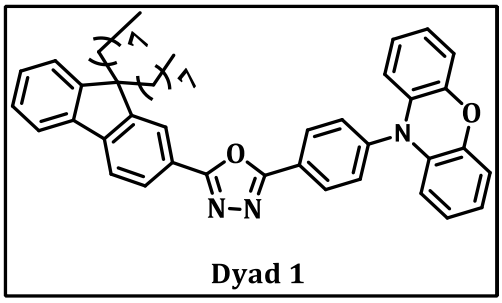

Dyad 1

$p(tBu)_3$ (99 mg, 0.49 mmol) in toluene (30 mL) was heated at 40 °C for 2 h and then the reaction mixture heated at 110 °C for 24 h. After the mixture was cooled to room temperature water and chloroform were added, the organic layer was separated and dried under reduced pressure. Column chromatography was carried out over silica gel using a 5% mixture of ethyl acetate and hexane. (0.94 g, 80%), ^{1}H NMR (500 MHz, $CDCl_3$, TMS) δ 0.62 (s, 4H), 0.79 (t, 6H, J = 7 Hz), 1.09 (m, 16H), 1.17 (m, 4H), 2.05 (m, 4H), 6.01(d, 2H, J = 7.5 Hz), 6.63 (m, 2H), 6.71 (m, 4H), 7.39 (d, 3H, J = 2 Hz), 7.57 (d, 2H, J = 8.5 Hz), 7.78(m, 1H), 7.86(d, 1H, J = 8 Hz), 8.14(t, 2H, J = 3.5 Hz), 8.42 (d, 2H, J = 8.5 Hz). ^{13}C NMR (125 MHz, $CDCl_3$) 165.63, 163.71, 151.73, 151.44, 145.09, 144.00, 142.26, 139.80, 133.79, 131.77, 129.70, 128.41, 127.11, 126.11, 124.08, 123.35, 123.08, 121.97, 121.86, 121.35, 120.51, 120.28, 115.75, 113.28, 55.51, 40.29, 31.76, 29.96, 29.22, 29.19, 23.78, 22.57, 14.06. ESI-MS: Calcd for $C_{49}H_{53}N_3O_2$, 715.41; Found 716.42 (M^++1).

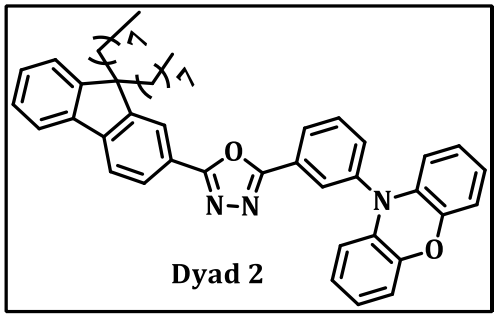

Dyad 2

10-(3-(5-(9,9-Dioctyl-9H-fluoren-2-yl)-1,3,4-oxadiazol-2-yl)phenyl)-10H-phenoxazine (2). A mixture of **7b** (1 g, 1.633 mmol), phenoxazine (0.448 g, 2.45 mmol), Cs_2CO_3 (1.596 g, 4.899 mmol), $Pd(OAc)_2$ (37 mg, 0.1633 mmol) and $p(t\text{-}Bu)_3$ (99 mg, 0.49 mmol) in toluene (30 mL) was heated at 40 °C

for 2 h and then the reaction mixture heated at 110 °C for 24 h. After the mixture was cooled to room temperature water and chloroform added, organic layer was separated and dried under reduced pressure. Column chromatography was carried out over silica gel using a 5% mixture of ethyl acetate and hexane. (0.88 g, 75%), ^{1}H NMR (500 MHz, $CDCl_3$, TMS) δ 0.58 (t, 4H, J = 6.5 Hz) 0.78 (t, 6H, J = 7 Hz), 1.06 (m, 16H), 1.17 (m, 4H), 2.05 (m, 4H), 5.97(m, 2H), 6.63 (m, 2H), 6.69 (m, 2H), 6.74 (m, 2H), 7.37 (t, 3H, J = 2.5 Hz), 7.58 (m, 1H), 7.76(m, 1H), 7.81(m, 2H), 8.13 (m, 3H), 8.35 (m, 1H). ^{13}C NMR (125 MHz, $CDCl_3$) 165.66, 163. 46, 151.71, 151.44, 145.08, 143.95, 140.00, 139.82,134.47, 133.97, 132.10, 129.50, 128.37, 127.31, 127.12, 127.06, 126.19, 123.38,123.05, 121.87, 121.80, 121.33, 120.50, 120.25, 115.71, 113.26, 55.54, 40.26, 31.73, 29.92, 29.22, 23.76, 22.56, 14.04. ESI-MS: Calcd for $C_{49}H_{53}N_3O_2$, 715.42; Found 716.42 (M^++1).

2.6. References

(1) Tang, C. W.; VanSlyke, S. A. *Appl. Phys. Lett.* **1987**, *51*, 913.

(2) Tong, Q.-X.; Lai, S.-L.; Chan, M.-Y.; Zhou, Y.-C.; Kwong, H.-L.; Lee, C.-S.; Lee, S.-T. *Chem. Mater.* **2008**, *20*, 6310.

(3) (a) Yuan, Y.; Zhang, G. Q.; Lu, F.; Tong, Q. X.; Yang, Q. D.; Mo, H. W.; Ng, T. W.; Lo, M. F.; Guo, Z. Q.; Wu, C.; Lee, C. S. *Chem. Asian J.* **2013**, *8*, 1253(b) Shirota, Y.; Kinoshita, M.; Noda, T.; Okumoto, K.; Ohara, T. *J. Am. Chem. Soc.* **2000**, *122*, 11021.

(4) Ding, J.; Gao, J.; Cheng, Y.; Xie, Z.; Wang, L.; Ma, D.; Jing, X.; Wang, F. *Adv. Funct. Mater.* **2006**, *16*, 575.

(5) Hashimoto, M.; Igawa, S.; Yashima, M.; Kawata, I.; Hoshino, M.; Osawa, M. *J. Am. Chem. Soc.* **2011**, *133*, 10348.

(6) Duan, L.; Hou, L.; Lee, T.-W.; Qiao, J.; Zhang, D.; Dong, G.; Wang, L.; Qiu, Y. *J. Mater. Chem.* **2010**, *20*, 6392.

(7) Zhang, Q.; Kuwabara, H.; Potscavage, W. J.; Huang, S.; Hatae, Y.; Shibata, T.; Adachi, C. *J. Am. Chem. Soc.* **2014**, *136*, 18070.

(8) (a) Lee, C. W.; Lee, J. Y. *ACS Appl. Mater. Interfaces* **2015**, *7*, 2899(b) Tsai, M. H.; Lin, H. W.; Su, H. C.; Ke, T. H.; Wu, C. c.; Fang, F. C.; Liao, Y. L.; Wong, K. T.; Wu, C. I. *Adv. Mater.* **2006**, *18*, 1216(c) Kido, J.; Kohda, M.; Okuyama, K.; Nagai, K. *Appl. Phys. Lett.* **1992**, *61*, 761.

(9) Jou, J.-H.; Kumar, S.; Agrawal, A.; Li, T.-H.; Sahoo, S. *J. Mater. Chem. C* **2015**, *3*, 2974.

(10) Jiang, H. *Macromol. Rapid Commun.* **2010**, *31*, 2007.

(11) Zhu, X. H.; Peng, J.; Cao, Y.; Roncali, J. *Chem. Soc. Rev.* **2011**, *40*, 3509.

(12) (a) Huang, F.; Cheng, Y.-J.; Zhang, Y.; Liu, M. S.; Jen, A. K. Y. *J. Mater. Chem.* **2008**, *18*, 4495(b) Yao, L.; Xue, S.; Wang, Q.; Dong, W.; Yang, W.; Wu, H.; Zhang, M.; Yang, B.; Ma, Y. *Chem. Eur. J.* **2012**, *18*, 2707.

(13) (a) Inomata, H.; Goushi, K.; Masuko, T.; Konno, T.; Imai, T.; Sasabe, H.; Brown, J. J.; Adachi, C. *Chem. Mater.* **2004**, *16*, 1285(b) Gong, S.; Zhao, Y.; Wang, M.; Yang, C.; Zhong, C.; Qin, J.; Ma, D. *Chem. Asian J.* **2010**, *5*, 2093(c) Lindner, B. D.; Zhang, Y.; Hofle, S.; Berger, N.; Teusch, C.; Jesper, M.; Hardcastle, K. I.; Qian, X.; Lemmer, U.; Colsmann, A.; Bunz, U. H. F.; Hamburger, M. *J. Mater. Chem. C* **2013**, *1*, 5718(d) Aydemir, M.; Haykr, G.; Turksoy, F.; Gumus, S.; Dias, F. B.; Monkman, A. P. *Phys. Chem. Chem. Phys.* **2015**, *17*, 25572(e) Karthik, D.; Justin Thomas, K. R.; Jou, J.-H.; Kumar, S.; Chen, Y.-L.; Jou, Y.-C. *RSC Adv.* **2015**, *5*, 8727(f) Priyanka, B.; Anusha,

V.; Bhanuprakash, K. *J. Phys. Chem. C* **2015**, *119*, 12251(g) Wei, X.-F.; Tan, W.-Y.; Zou, J.-H.; Guo, Q.-X.; Gao, D.-Y.; Ma, D.-G.; Peng, J.; Cao, Y.; Zhu, X.-H. *J. Mater. Chem. C* **2017**, *5*, 2329.

(14) (a) Paun, A.; Hadade, N. D.; Paraschivescu, C. C.; Matache, M. *J. Mater. Chem. C* **2016**, *4*, 8596(b) Kulkarni, A. P.; Tonzola, C. J.; Babel, A.; Jenekhe, S. A. *Chem. Mater.* **2004**, *16*, 4556.

(15) Gong, S.; Chen, Y.; Zhang, X.; Cai, P.; Zhong, C.; Ma, D.; Qin, J.; Yang, C. *J. Mater. Chem.* **2011**, *21*, 11197.

(16) Prachumrak, N.; Pojanasopa, S.; Tarsang, R.; Namuangruk, S.; Jungsuttiwong, S.; Keawin, T.; Sudyoadsuk, T.; Promarak, V. *New J. Chem.* **2014**, *38*, 3282.

(17) Kapoor, N.; Thomas, K. R. J. *New J. Chem.* **2010**, *34*, 2739.

(18) Park, Y.; Kim, B.; Lee, C.; Hyun, A.; Jang, S.; Lee, J.-H.; Gal, Y.-S.; Kim, T. H.; Kim, K.-S.; Park, J. *J. Phys. Chem. C* **2011**, *115*, 4843.

(19) Belei, D.; Dumea, C.; Bicu, E.; Marin, L. *RSC Adv.* **2015**, *5*, 8849.

(20) Lee, J.; Shizu, K.; Tanaka, H.; Nomura, H.; Yasuda, T.; Adachi, C. *J. Mater. Chem. C* **2013**, *1*, 4599.

(21) (a) Wang, H.; Xie, L.; Peng, Q.; Meng, L.; Wang, Y.; Yi, Y.; Wang, P. *Adv. Mater.* **2014**, *26*, 5198(b) Serevicius, T.; Nakagawa, T.; Kuo, M.-C.; Cheng, S.-H.; Wong, K.-T.; Chang, C.-H.; Kwong, R. C.; Xia, S.; Adachi, C. *Phys. Chem. Chem. Phys.* **2013**, *15*, 15850(c) Nasu, K.; Nakagawa, T.; Nomura, H.; Lin, C.-J.; Cheng, C.-H.; Tseng, M.-R.; Yasuda, T.; Adachi, C. *Chem. Commun.* **2013**, *49*, 10385.

(22) (a) Tsuie, B.; L. Reddinger, J.; A. Sotzing, G.; Soloducho, J.; R. Katritzky, A.; R. Reynolds, J. *J. Mater. Chem.* **1999**, *9*, 2189(b) Vyas, P. V.; Bhatt, A. K.;

Ramachandraiah, G.; Bedekar, A. V. *Tet. Lett.* **2003**, *44*, 4085(c) Wong, K.-T.; Ku, S.-Y.; Cheng, Y.-M.; Lin, X.-Y.; Hung, Y.-Y.; Pu, S.-C.; Chou, P.-T.; Lee, G.-H.; Peng, S.-M. *J. Org. Chem.* **2006**, *71*, 456(d) Reddy, M. A.; Thomas, A.; Srinivas, K.; Rao, V. J.; Bhanuprakash, K.; Sridhar, B.; Kumar, A.; Kamalasanan, M. N.; Srivastava, R. *J. Mater. Chem.* **2009**, *19*, 6172.

(23) Ono, K.; Joho, M.; Saito, K.; Tomura, M.; Matsushita, Y.; Naka, S.; Okada, H.; Onnagawa, H. *Eur. J. Inorg. Chem.* **2006**, *2006*, 3676.

(24) Tanaka, H.; Shizu, K.; Nakanotani, H.; Adachi, C. *Chem. Mater.* **2013**, *25*, 3766.

(25) Tao, Y.; Wang, Q.; Yang, C.; Zhong, C.; Zhang, K.; Qin, J.; Ma, D. *Adv. Funct. Mater.* **2010**, *20*, 304.

(26) Sanju, K. S.; Thurakkal, S.; Neelakandan, P. P.; Joseph, J.; Ramaiah, D. *Phys. Chem. Chem. Phys.* **2015**, *17*, 13495.

(27) Kaafarani, B. R.; El-Ballouli, A. a. O.; Trattnig, R.; Fonari, A.; Sax, S.; Wex, B.; Risko, C.; Khnayzer, R. S.; Barlow, S.; Patra, D.; Timofeeva, T. V.; List, E. J. W.; Bredas, J.-L.; Marder, S. R. *J. Mater. Chem. C* **2013**, *1*, 1638.

(28) Viji, M.; Nair, A. K.; Nandajan, P. C.; Ramaiah, D. *RSC Adv.* **2014**, *4*, 47982.

(29) Kucherak, O. A.; Didier, P.; Mély, Y.; Klymchenko, A. S. *J. Phys. Chem. Lett.* **2010**, *1*, 616.

(30) Ishimatsu, R.; Matsunami, S.; Shizu, K.; Adachi, C.; Nakano, K.; Imato, T. *J. Phys. Chem. A* **2013**, *117*, 5607.

(31) (a) Kim, S.-Y.; Cho, Y.-J.; Lee, A.-R.; Son, H.-j.; Han, W.-S.; Cho, D. W.; Kang, S. O. *Phys. Chem. Chem. Phys.* **2017**, *19*, 426(b) Chen, R.; Zhao, G.; Yang, X.; Jiang, X.; Liu,

J.; Tian, H.; Gao, Y.; Liu, X.; Han, K.; Sun, M.; Sun, L. *J. Mol. Struct.* **2008**, *876*, 102(c) Vázquez, M. E.; Blanco, J. B.; Imperiali, B. *J. Am. Chem. Soc.* **2005**, *127*, 1300.

(32) (a) Ramachandran, E.; Dhamodharan, R. *J. Mater. Chem. C* **2015**, *3*, 8642(b) Chebrolu, L. D.; Thurakkal, S.; Balaraman, H. S.; Danaboyina, R. *Sens. Actuators B, Chem.* **2014**, *204*, 480.

(33) Kuruvilla, E.; Ramaiah, D. *J. Phys. Chem. B* **2007**, *111*, 6549.

(34) Neelakandan, P. P.; Ramaiah, D. *Angew. Chem. Int. Ed.* **2008**, *47*, 8407.

(35) Carlos, L. D.; De Mello DonegÁ, C.; Albuquerque, R. Q.; Alves, S.; Menezes, J. F. S.; Malta, O. L. *Mol. Phys.* **2003**, *101*, 1037.

(36) (a) Becke, A. D. *J. Chem. Phys.* **1993**, *98*, 5648(b) Lee, C.; Yang, W.; Parr, R. G. *Phys. Rev. B: Condens. Matter* **1988**, *37*, 785(c) Krishnan, R.; Binkley, J. S.; Seeger, R.; Pople, J. A. *J. Chem. Phys.* **1980**, *72*, 650.

(37) Miertuš, S.; Scrocco, E.; Tomasi, J. *Chem. Phys.* **1981**, *55*, 117.

Chapter 3

Design of Blue Light Emitting Dyads Based on Carbazole and Oxadiazole for OLED Applications

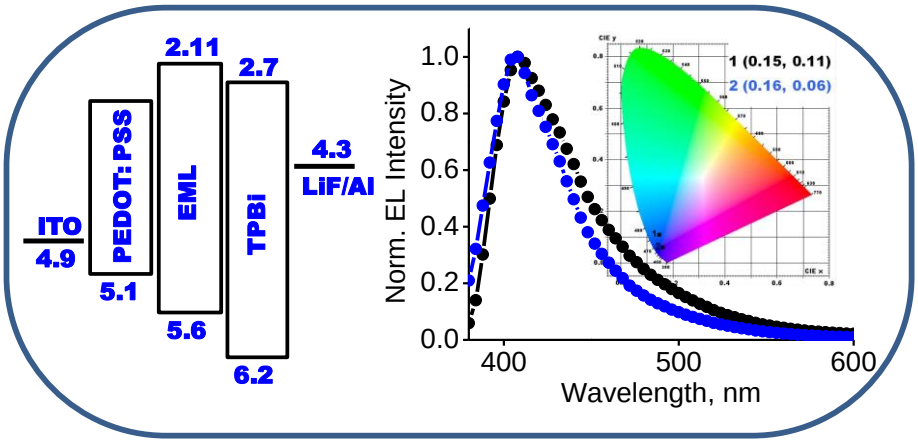

3.1. Abstract

With an objective to develop efficient solution processable deep blue emitters with good colour purity, we have synthesised two versatile D-π-A dyads **1** and **2** combining electron donating carbazole and accepting oxadiazole groups. In order to understand the intramolecular electron communication between the donor and acceptor moieties, we have changed the substitution pattern at the phenylene linker. We found substitution dependent photophysical properties both in the solution and film state. The dyad **1** showed absorption bands at 295, 330 and 350 nm. As the position of the carbazole moiety changed from the *para*-position in dyad **1** to the *meta*-position in dyad **2**, the intensity of the band at 350 nm was decreased and a new shoulder at 345 nm was formed. In the film state,

dyads **1** and **2** showed deep blue emission having λ_{max} at 415 nm and 409 nm with the fluorescence quantum yield (Φ_F) of 0.45 and 0.11, respectively. From the non-polar cyclohexane to polar acetonitrile, a negligible change in the absorption maxima was observed for the dyads **1** and **2** while the emission maxima was red-shifted by *ca.* 90 nm (5380 cm^{-1}) and 110 nm (5500 cm^{-1}), respectively. The observed large change in the dipole moment of *ca.* 22.42 and 23.95 D for the dyads **1** and **2** respectively, suggests ICT character between the donor and acceptor moieties.

From the ground state optimised geometries, the dyads **1** and **2** have a well separated HOMO and LUMO at the hole and electron transporting moieties, respectively. The dyads showed reversible oxidation waves and HOMO/LUMO values of 5.62/2.43 eV for dyad **1** and 5.61/2.22 eV for dyad **2**. In line with the design strategy adopted, both the dyads are found to be thermally quite stable up to 390 °C and solution processable. Furthermore, we have fabricated the solution processed un-doped OLEDs based on these dyads with device configuration having ITO (120 nm)/ PEDOT: PSS (40 nm)/ Dyad **1** or **2** (50 nm)/ TPBi (40 nm)/ LiF(1 nm)/ Al (100 nm). These devices based on the dyads **1** and **2** exhibited deep blue electroluminescence in near ultraviolet (NUV) region having λ_{max} at 410 nm and 408 nm with a narrow full width at half maximum (FWHM) of 54 and 49 nm and CIE coordinates of (0.16, 0.07) and (0.16, 0.05), respectively, which confirms very good color purity. These systems showed a maximum luminance of *ca.* 62.17 and 61.45 cd m^{-2} with a current efficiency of *ca.* 0.45 and 0.44 cd A^{-1}, respectively.

3.2. Introduction

Organic light emitting diodes with various emission colors of high efficiencies and color purity are successfully utilized in full color flat panel displays and solid state white lighting devices.[1] To date, numerous classes of organic light emitting materials have been developed and these efforts are still continuing in order to find out materials that are easy to synthesize and exhibit improved solution processability and high efficiency.[2] Blue light emitting materials are one of the important components for fabricating white OLEDs and are very critical for making high quality displays.[3] In addition, due to their intrinsic larger band gap (E_{gap}), the blue emitters also can serve as a host for a variety of lower energy fluorescent or phosphorescent dopant emitters.[4] Compared with the superior performances of green and red emitters, blue light emitting materials still need to be improved.[5] Owing to the large band gap, the excited states of deep blue emitters possess very high energy levels and the devices based on these emitters were found to be less stable.[6] Hence, the development of efficient deep blue emitting materials with good efficiency and color purity is still a big challenge.

The conventional fluorescence and phosphorescence based OLEDs of dopant-host system were widely accepted for the improved device efficiency.[7] However, the precise control of dopant-host ratio increases the complexity of fabrication process and thus the cost during the mass production of OLEDs.[8] In addition, phase separation in such a dopant-host system is also a potential problem, and therefore, the use of un-doped emitting layer has practical significance due to the ease of fabrication and reliability.[9] A balanced charge transport is essential for effective exciton recombination

in the emissive layer. The hole and electron mobility of the emitters can be improved by combing both electron donating and withdrawing moieties into a single emitter.[10] Solution processable OLEDs are more attractive compared to the vacuum evaporated for the development of low cost devices. In this context, design of unsymmetrical structures substituted with long alkyl chains provide better solubility and reduced aggregation in these molecules.[11]

The small organic donor-acceptor type fluorophores have distinct advantages like comparatively simple synthesis, purification and analysis.[12] A donor-acceptor structure can have large degree of control over the optoelectronic properties in accordance with their structural modification.[13] Changing the donor strength is the one of the way to fine-tune the band gap of D-A emitters. The conjugated building blocks such as anthracene, pyrene, diphenylamine and carbazole have been successfully used for designing and synthesizing blue light emitting active layers.[14] Among these, carbazole is a well-known electron donor building block for optoelectronic materials with good thermal stability and hole transporting ability.[15] Herein, we have designed and synthesized the luminescent dyads **1** and **2** (Chart 3. 1.) having electron donating carbazole and accepting oxadiazole moieties and have invested their photophysical, thermal, electrochemical and morphological aspects and also their use in OLEDs. Interestingly, these systems exhibited substitution dependent photophysical properties and act as deep blue emitters in the device performance, thereby indicating its potential use in OLEDs applications.

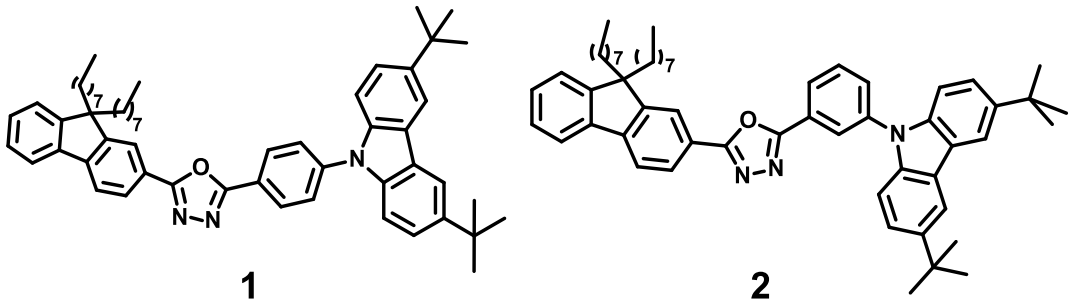

Chart 3.1. Structures of the investigated donor-acceptor dyads **1** and **2**.

3.3. Results and Discussion

3.3.1. Synthesis and photophysical properties

The designed molecules are incorporated with 3,6-di-tert-butyl-carbazole, a relatively weak donor compared to the phenoxazine and acceptor 2-(9,9-dioctyl-9H-fluoren-2-yl)-1,3,4-oxadiazole linked through a phenylene linker by *para*- (dyad **1**) and *meta*- (dyad **2**) substitution. The presence of a weak donor like carbazole results in lower intramolecular charge transfer in the D-A structures and thus a blue shifted absorption and emission spectra. A better solubility in organic solvents was achieved by adopting unsymmetrical structures with long alkyl chains. The *para*- and *meta*- bromo substituted precursors **7a** and **7b** were synthesized as shown in the scheme 3.1. The detailed synthetic procedures adopted and characterization details of the synthesized precursors are given in chapter **2**.

The synthesis of the target dyads **1** and **2** was achieved through Buchwald-Hartwig coupling reaction between the donor 3,6-di-tert-butyl-carbazole and the acceptor *para*- or *meta*- oxadiazole moiety (Scheme 3.1). The carbazole system upon

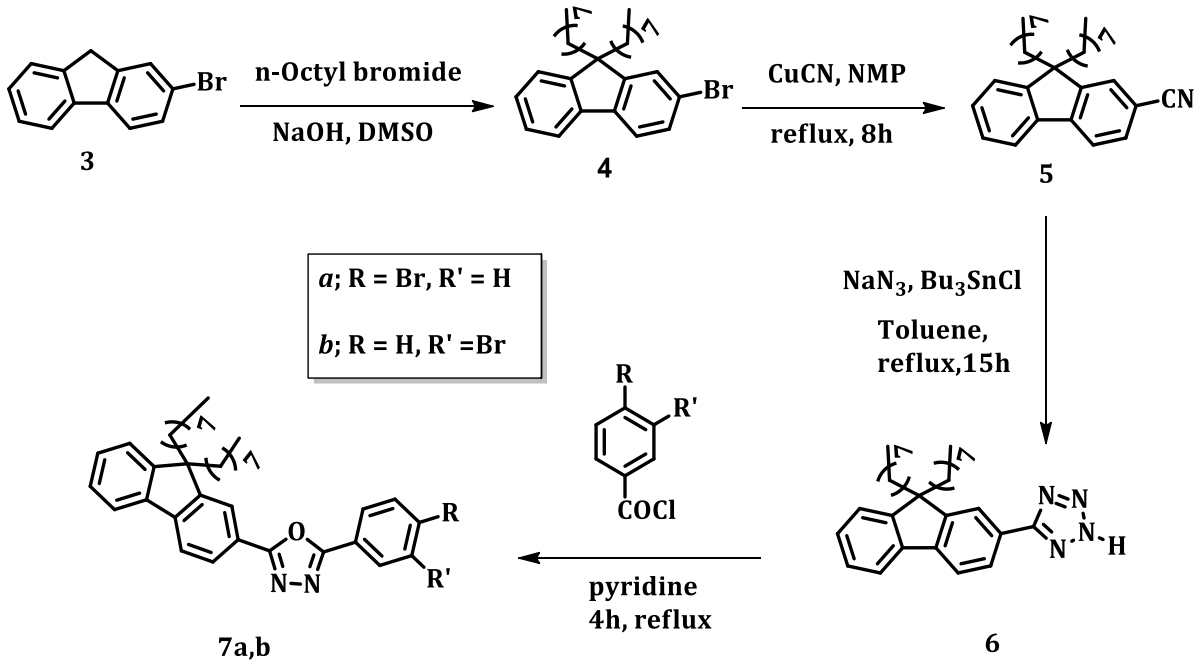

Scheme 3.1. Synthetic method adopted for the precursors **7a** and **7b.**

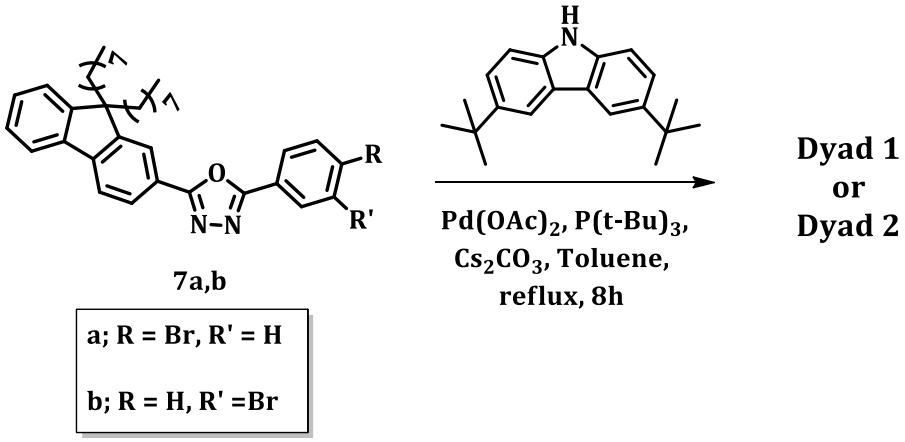

Scheme 3.2. Synthetic method adopted for the donor-acceptor dyads **1** and **2**.

Pd-catalyzed cross-coupling reaction with **7a** and **7b** in presence of cesium carbonate as the additive base, gave the dyads **1** and **2** in quantitative yields, respectively.[16] The starting materials as well as the dyads were purified through column chromatography and recrystallization and were characterized on the basis of various spectroscopic and

analytical evidences. In the ^{1}H NMR spectra, both dyads **1** and **2** showed 52 aliphatic protons and 17 aromatic protons. The peak corresponds to δ 8.16 (t, 4H) of the dyad **1** was observed at δ 8.10 (m, 2H) and δ 8.18 (s, 2H) for the dyad **2** and similarly peak at δ 8.41 (d, 2H) as δ 8.28(m, 1H) and δ 8.36 (s, 1H). In the ^{13}C spectra, the number of carbons for the dyads **1** and **2** were found to be 35 and 37, respectively.

The UV-Visible absorption and fluorescence spectra of the dyads **1** and **2** have been studied in toluene solution (Figure 3.1A). The absorption at 295 nm can be[17] attributed to the carbazole centered n-π* transition and the peaks at 325-330 nm arises from the π-π* transition of the flourene moiety.[18] Notably, the absorption at 350 nm for **1** may be assigned to the charge transfer transition from the electron donating carbazole to the electron accepting oxadiazole moiety. Interestingly, we observed a decrease in the absorption at 350 nm and formation of a new broad band having absorption in the region 345 nm, as the position of the carabzole moiety changed from the *para*- position (dyad **1**) to the *meta*- position (dyad **2**). These observations can be attributed to the minimizing conjugation between the donor and acceptor subunits in case of the dyad **2** owing to its *meta*- linkage, which is in agreement with the literature reports.[19]

Further, we observed blue fluorescence having λ_{max} at 409 and 419 nm (λ_{exc} = 330 nm) for the dyads **1** and **2**, respectively. We have noticed that the fluorescence quantum yield of dyad **1** in toluene (Φ_F = 0.72) is substantially higher than that of dyad **2** (Φ_F = 0.06). This is attributed to the extended π conjugation for *para*- substituted dyad **1**. In the thin film, dyad **1** showed a broad and less intense absorption peak at

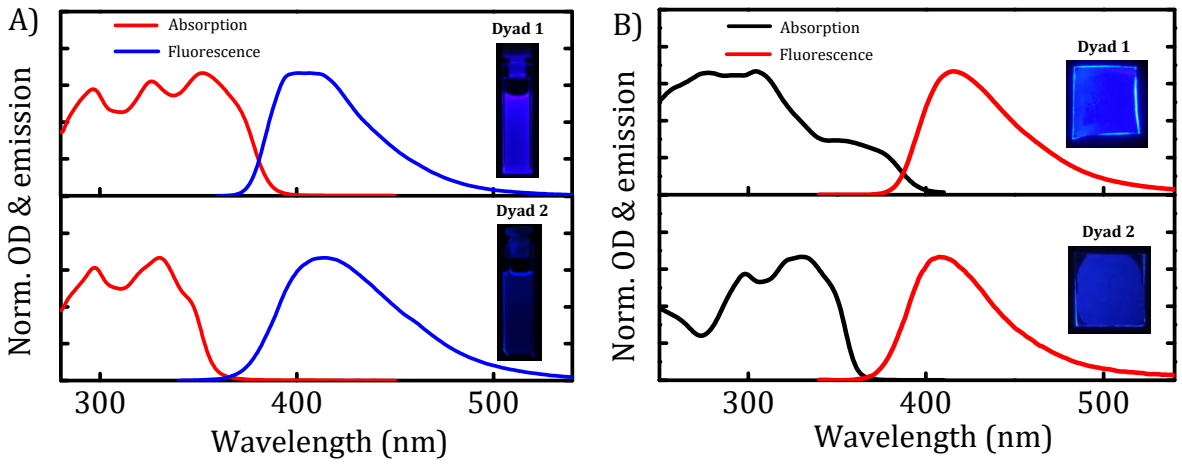

Figure 3.1. Normalized absorption and fluorescence spectra of the dyads **1** and **2** at 298, A) in toluene and B) in film state. Excitation wavelength, 330 nm.

Table 3.1. Summary of the absorption and emission properties of the dyads **1** and **2** in toluene solution and film state. [a]

Dyad	λ_{abs}[b] nm	ε_{max} [b] M^{-1} cm^{-1} x 10^4	λ_{ems}[b],nm (Φ_F)[b]	λ_{abs}[c] nm	λ_{ems}[c] , nm (Φ_F) [c]
1	352, 325	3.82, 3.55	409 (0.72±0.02)	352, 303	415 (0.45±0.02)
2	345, 330	3.54, 5.30	419 (0.06±0.03)	330, 298	409 (0.11±0.02)

[a] Average of more than three independent experiments, [b] measured for toluene and [c] measured for spin cast film. λ_{abs}: absorption wavelength, ε_{max}: molar extinction coefficient, λ_{ems}: emission wave length, Φ_F: absolute quantum yield.

around 352 nm and an intense peak at 303 nm and dyad **2** showed peaks at 330 nm and 290 nm (Figure 3.1B). The emissions maximum of the films of **1** and **2** were observed at 415 nm and 409 nm respectively (λ_{exc} = 330 nm). The calculated CIE coordinates of the dyads **1** and **2** were found to be (0.15, 0.06) and (0.14, 0.13) in toluene and (0.15, 0.11) and (0.16, 0.06) in the film state,

respectively, which are correspond to pure blue emission. The fluorescence lifetimes of the dyads **1** and **2** were measured in toluene and the results are summarized in Table 3.2 and Figure 3.2. The *para*- derivative dyad **1** exhibited monoexponential decay while the *meta*- derivative dyad **2** showed biexponential decay with a short lived minor component and a comparatively long-lived major component (τ_1 = 1.7 ns for **1**; τ_1 = 4.03 ns (23.92 %) and τ_2 = 8.79 ns (76.08 %) for **2**). The observed biexponential decay can be attributed to the presence of different conformers due to the existence of restricted rotation.[20] By using the fluorescence quantum yield (Φ_F) and averaged lifetimes (<τ>), the rate constants of radiative (k_r) and non-radiative (k_{nr}) decay of the dyads were calculated according to equations $k_r = \Phi_F/\tau$ and $k_{nr} = 1 - \Phi_F/\tau$. Compared to the phenoxazine derivatives, the carbazole systems showed a higher radiative transition in these dyads. While comparing the dyads **1** and **2,** the *para*- substituted derivative dyad **1** exhibited higher radiative decay than that of dyad **2** due to the improved conjugation between donor and acceptor moiety.

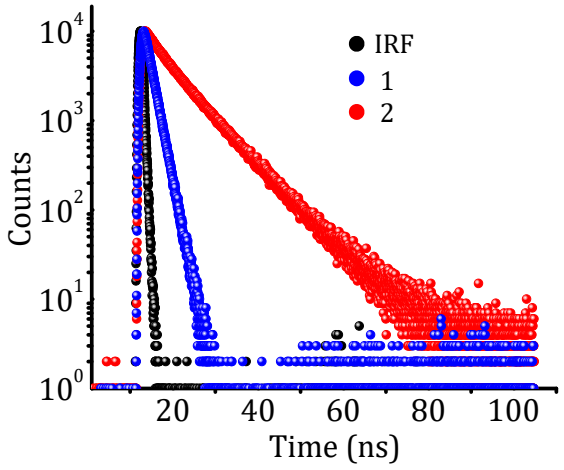

Figure 3.2. Fluorescence decay curves of A) dyad **1** and B) dyad **2** in toluene solution.

Table 3.2. Summary of life time measurements in toluene solution

Dyads	τ (ns)	k_r (10^7 S^{-1})	k_{nr} (10^7 S^{-1})
1	τ_1= 1.7	5.18	0.71
2	τ_1= 4.03 (23.92%) τ_2= 8.79 (76.08%)	0.19	1.27

<τ>: average fluorescence lifetime, τ: fluorescence lifetime, k_r and k_{nr}: rate contants of radiative and non-radiative transition, respectively.

The absorption and emission spectra of dyads **1** and **2** were recorded in various solvents of differing polarity. Upon changing the solvent polarity of the medium from cyclohexane to acetonitrile, the solvatochromic change in the absorption spectra is minimal (Figure 3.3A and 3.4A). This suggests a less polar ground state, which will be less effectively solvated by the polar solvents. In the fluorescence spectra, we observed the broadening of the spectrum with a gradual increase in redshift (Figure 3.3B and 3.4B). From the non-polar cyclohexane to polar acetonitrile, we observed a redshift of *ca.* 90 nm (5380 cm^{-1}) and 110 nm (5500 cm^{-1}) for the dyads **1** and **2**, respectively (Table 3.3 and 3.4). These observations indicate that the solvent-solute interactions found to stabilize the S_1 excited states, yielding a dipole moment that is larger than that in the ground state. The emission maxima (ν_{max}, in wave number) were plotted against the solvent polarity parameter $E_T(30)$ as shown in Figure 3.5A. These systems exhibited a positive solvatochromism with the emission maxima depending approximately linearly on the solvent polarity. From the changes in Stokes shift in various solvents, the change in the dipole moment ($\Delta\mu_{ge}$) between

the ground (S_0) and excited states (S_1) can be calculated using the equation 3.1,[21]

$$\nu_{abs} - \nu_{flu} = \frac{1}{4\pi\varepsilon_0}\frac{2\Delta\mu^2}{hca^3}\Delta f + \text{constant} \ldots\ldots\ldots\ldots (\text{Eq } 3.1)$$

wherein, 'ν_{abs}' and 'ν_{fluo}' are the absorption and fluorescence of the dyads **1** and **2** in wave numbers, respectively, 'ε_0' is the vacuum permittivity, 'h' is the Plank's constant,

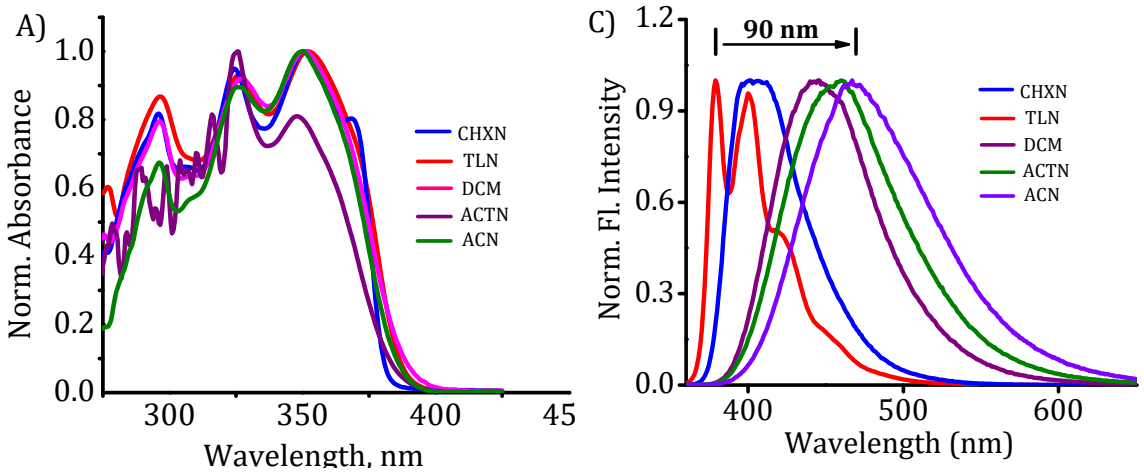

Figure 3.3: Absorption (A) and fluorescence (B) spectra of the dyad **1** in different solvent (10 μM each). Excitation wavelength, 330 nm.

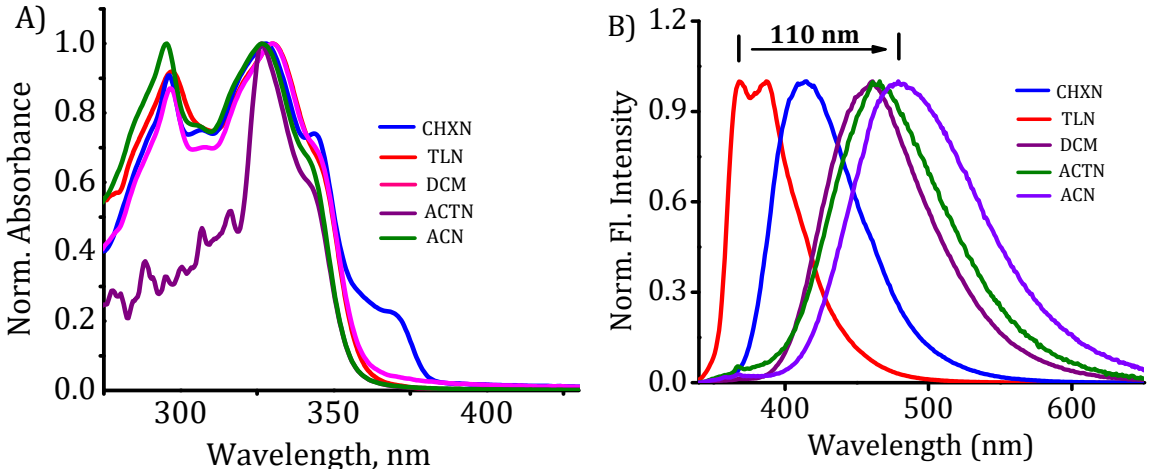

Figure 3.4: Absorption (A) and fluorescence (B) spectra of the dyad **2** in different solvent (10 μM each). Excitation wavelength, 330 nm.

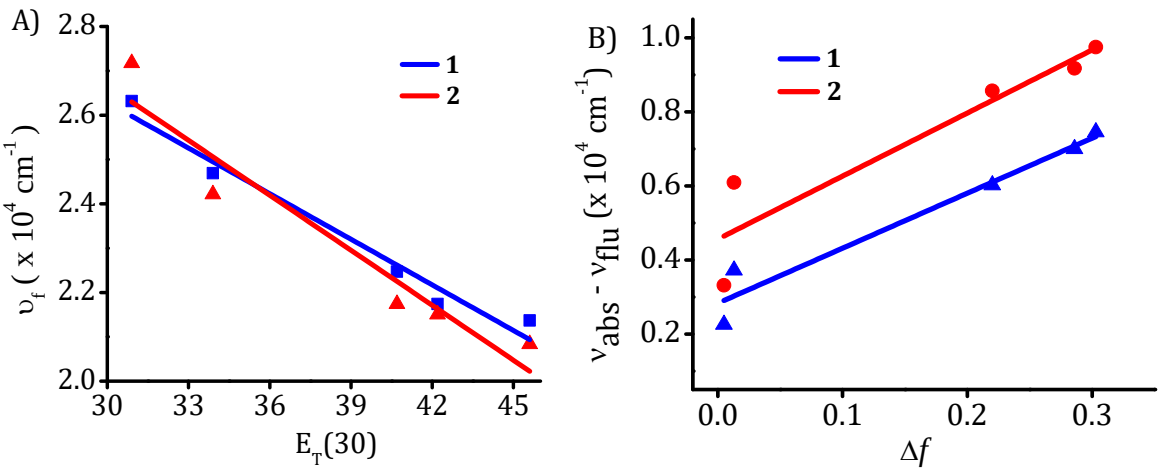

Figure 3.5. A) Plot of the emission maximum in different solvents *vs* solvent polarity parameter $E_T(30)$ and B) plot of Stokes shift against the solvent polarity (Δf). From the left, cyclohexane, toluene, dichloromethane, acetone and acetonitrile solutions and the solid lines show least-squares fit.

'c' is the speed of light and 'a' is the Onsager cavity radius, which was *ca.* 6.98 and 6.97 Å for the dyads **1** and **2**, respectively as determined from DFT calculations using Gaussian 09.[22] The term Δf, known as the solvent polarity parameter was obtained by the equation $((\varepsilon-1)/(2\varepsilon+1)) - ((n^2-1)/(2n^2+1))$, wherein ε is the dielectric constant and n is the refractive index of the solvent. The Stokes shift for emissions changed linearly with Δf as shown in Figure 3.5B. Using the slope value of *ca.* 14859.86 and 17035.47 cm^{-1} for the dyads **1** and **2**, respectively, and equation 3.1, we have estimated the dipole moment change ($\Delta\mu_{ge}$), which is found to be *ca.* 22.42 and 23.95 D for the dyads **1** and **2**, respectively. The calculated dipole moment for the ground states obtained from DFT calculations are *ca.* 3.69 and 2.77 D while the dipole moment of the excited states obtained by the solvatochromic method are *ca.* 26.11 and 26.72 D for the dyads **1** and **2,** respectively. The relatively larger change in the dipole moment suggested ICT character between carbazolyl groups (electron donors) and oxadiazole moiety (electron

Table 3.3. Absorption and emission properties of the dyad **1** in different solvents. [a]

Solvents	ε	n	Δ*f*	λ_a (nm)	ν_a (cm^{-1})	λ_F (nm)	ν_F (cm^{-1})	ν_a - ν_F (cm^{-1})
CHXN	2.02	1.43	0.005	324, 350	28571.4	380	26315.7	2255.64
TLN	2.38	1.49	0.013	325, 352	28409.0	405	24691.3	3717.73
DCM	9.10	1.42	0.220	326, 351	28490.0	445	22471.9	6018.12
ACTN	21.00	1.36	0.286	325, 348	28735.6	460	21739.1	6996.5
ACN	37.50	1.35	0.303	325, 347	28818.4	468	21367.5	7450.93

[a]Average of more than three independent experiments, ε: dielectric constant, n: refractive index, Δ*f*: solvent polarity parameter, λ_a: absorption wavelength, ν_a: wave number corresponds to absorption maximum, λ_F: fluorescence wavelength, ν_F: wave number corresponds to fluorescence maximum.

Table 3.4. Absorption and emission properties of the dyad **2** in different solvents. [a]

Solvents	ε	n	Δ*f*	λ_a (nm)	ν_a (cm^{-1})	λ_F (nm)	ν_F (cm^{-1})	ν_a - ν_F (cm^{-1})
CHXN	2.02	1.43	0.005	328, 344	30487.8	368	27173.91	3313.89
TLN	2.38	1.49	0.013	330, 344	30303.0	413	24213.07	6089.96
DCM	9.10	1.42	0.220	330, 343	30303.0	460	21739.13	8563.9
ACTN	21.00	1.36	0.286	326, 341	30674.8	465	21505.38	9169.47
ACN	37.50	1.35	0.303	327, 341	30581.0	480	20833.33	9747.71

[a]Average of more than three independent experiments, ε: dielectric constant, n: refractive index, Δf: solvent polarity parameter, λ_a: absorption wavelength, ν_a: wave number corresponds to absorption maximum, λ_F: fluorescence wavelength, ν_F: wave number corresponds to fluorescence maximum.

acceptors). These results clearly indicate that the high dipole moment of the charge transfer states is responsible for the solvent polarity dependent redshifted emission observed for the dyads.

Further, we have recorded phosphorescence spectra (delayed by 10 ms) of the dyads **1** and **2** in toluene at 77 K and observed a great overlap with their corresponding fluorescence spectra (Figure 3.6). The triplet energy of the both conjugates was determined from the onset values of corresponding phosphorescence spectrum and the values were found to be *ca.* 3.04 and 3.06 eV for the dyads **1** and **2**, respectively. In addition, a small energy difference (ΔE_{ST}) of *ca.* 0.31 and 0.29 eV was observed between the singlet and triplet excited states of the dyads **1** and **2**, respectively, thereby indicating their use as efficient TADF emitters. To understand the TADF properties, we have compared the photoluminescence efficiency of these molecules in air saturated toluene with the oxygen free toluene (by freeze-thaw degassing). For both the dyads **1** and **2**, we observed an increase in the fluorescence intensity and quantum yields after freeze-thaw degassing of the solutions (Figure 3.7 and Table 3.5). These

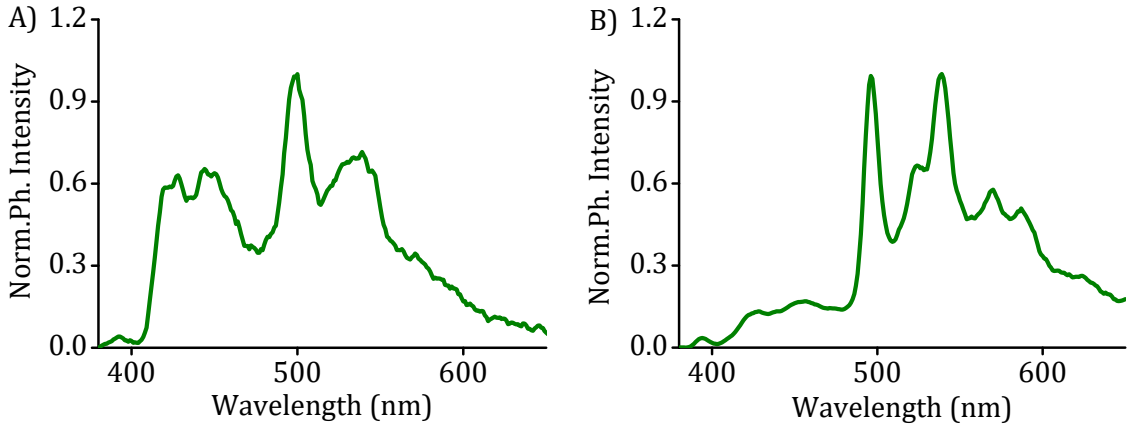

Figure 3.6. Normalized phosphorescence spectra of dyad **1** (A) and **2** (B) in toluene solution (10 μM) at 77 K.

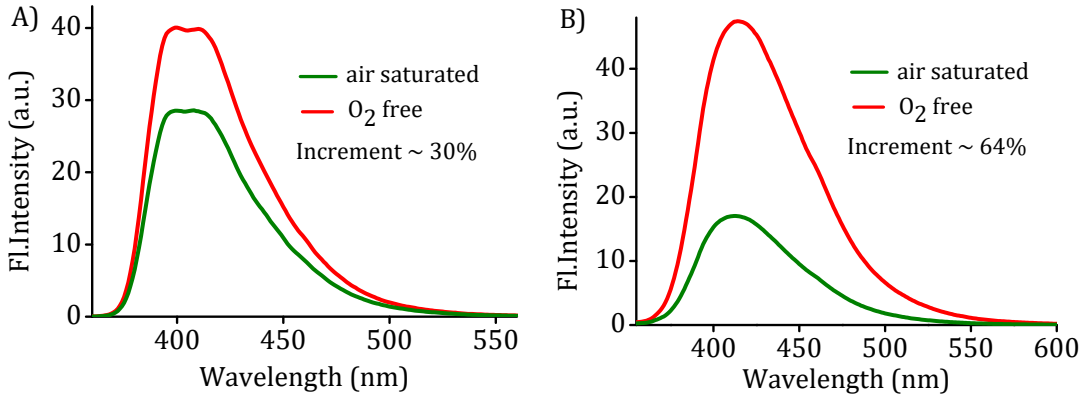

Figure 3.7. Fluorescence intensity changes before and after purging with nitrogen in toluene (10 μM) solution for the compounds, A) **1** and B) **2**. λ_{exc}, 350 nm.

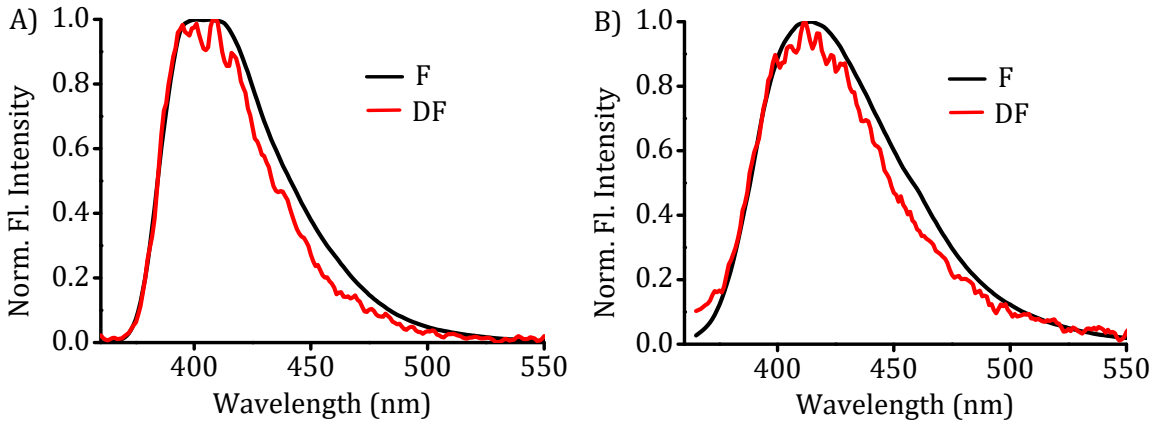

Figure 3.8. Prompt (F) and delayed fluorescence (DF) of the dyads **1** and **2** in toluene solution (10 μM).

observations can be attributed to the quenching of the triplet excited states by the dissolved oxygen present in toluene, and the concentration of which is negligible under freeze-thaw degassing conditions. The dyad **2**, which has relatively a lower ΔE_{ST} value of 0.29 eV and correspondingly, showed *ca.* 64% enhancement in the PLQYs intensity, whereas the dyad **1** with a relatively higher ΔE_{ST} value of 0.31 eV, exhibited the low enhancement of *ca.* 30%, in the emission after the removal of oxygen (Figure 3.7). After removing all the oxygen, the fluorescence quantum yield of dyads **1** and **2** were

increased from 0.77 to 0.88 and 0.06 to 0.13 respectively. In addition, we have recorded the delayed fluorescence of the dyads after a delay time of 60 μs in toluene solution (Figure 3.8).

Table 3.5. Delayed fluorescence properties of dyads **1** and **2** in toluene.

Dyads	ΔE_S (eV)	ΔE_T (eV)	ΔE_{ST} (eV)	Φ_{F+DF}
1	3.35	3.04	0.31	0.88
2	3.35	3.06	0.29	0.13

E_S and E_T: energy of singlet and triplet excited state, Φ_{F+DF}: fluorescence quantum yield in O_2 free toluene solution

3.3.2. Electrochemical, thermal and morphological analysis

The energy values of HOMOs and LUMOs of the dyads are important for the design of the device structure, which can be calculated from the CV curves and UV-Vis absorption spectra. Figure 3.9 shows the cyclic voltammogram of the dyads in dry dichloromethane under argon atmosphere. Both the dyad **1** and dyad **2** exhibited reversible oxidation waves due to the presence of electron donating carbazole group. The oxidation potentials *vs* Ag/Ag^+ were measured to be *ca.* 1.25 and 1.24 V for the dyads **1** and **2**, respectively and which are found to be relatively higher when compared to the phenoxazine derivatives. The redox potential of Fc/Fc^+ (standard value = 4.8 eV with respect to vacuum) was observed at 0.43 V. Based on this, the HOMO energy levels of molecules were estimated using the equation $E^{HOMO} = -E^{ox} - 4.37$ eV and the values are found to be 5.60 and 5.59 eV for the dyad **1** and **2**, respectively. And the LUMO energy levels were obtained by subtraction of the band gap energies (estimated from

the onset wavelengths of the corresponding UV absorption spectra) from the corresponding HOMO energies and the values were found to be approximately 2.43 and 2.22 eV, respectively. Thus, by substituting a weak donor carbazole instead of a strong donor phenoxazine, we achieved a wide band gap and thus a blue shifted absorption and emission properties.

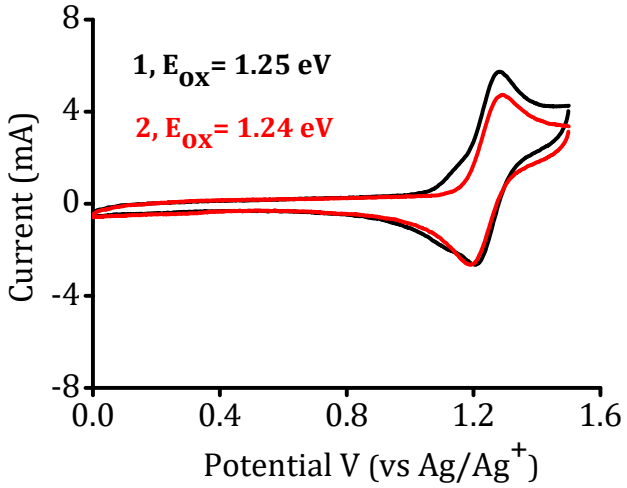

Figure 3.9. Cyclic voltammograms recorded for the dyads in dry dichloromethane (1 mM solutions; scan rate, 100 mV/s).

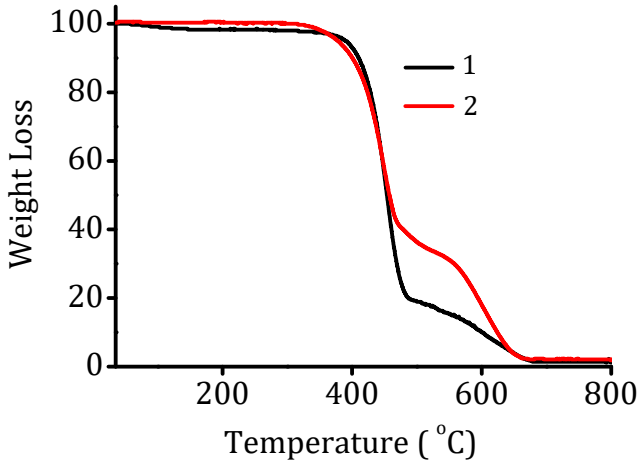

Figure 3.10. Thermogram of the dyads **1** and **2** in N_2 atmosphere.

The thermal stability of the dyads was investigated by using thermogravimetrical analysis (TGA) (Figure 3.10) and both these dyads were found to be thermally quite stable. The decomposition temperature (T_d), defined as the temperature at which 5% mass loss occurs of the dyads **1** and **2** were found to be *ca.* 390 and 375 °C and the melting points of the systems are *ca.* 151 and 159 °C, respectively. A film of thickness ~50 nm was obtained by spin casting a toluene solution of dyads (15 mg/mL) at 1000 rpm. The morphology of the films was studied using atomic force microscopy (AFM). As shown in Figure 3.11, the AFM images of solution processed films revealed smooth and homogeneous film morphologies with very small values of root mean square (RMS) roughness of *ca.* 0.42, 0.36 nm for the dyads **1** and **2,** respectively. These results demonstrate that both the dyad molecules have a good film forming ability by a solution process.

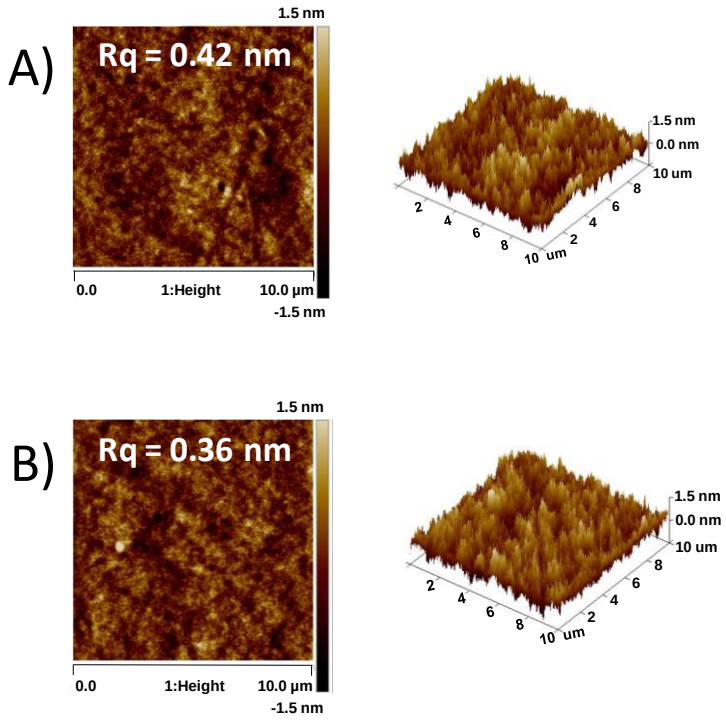

Figure 3.11. AFM images of solution processed A) **1** and B) **2** on ITO plate.

3.3.3. Theoretical calculations

To understand the electronic structure and band gap of the molecules, DFT calculation was performed using B3LYP hybrid functional with 6-311G (d, p) basis set. According to DFT calculations (Figure 3.12), the HOMO orbitals were mainly located on the electron donating carbazole moiety, whereas the LUMO orbitals were mainly distributed on the electron accepting oxadiazole moiety. The well separated HOMO and LUMO is responsible for the observed lower ΔE_{ST} values and reverse intersystem crossing in these dyads. The optimized dihedral angles between the donor moiety (carbazole unit) and the adjacent phenyl ring (θ_d) was 50.2° in dyad **1** and 53.1° in dyad **2**. Due to the reduced dihedral angle of dyads **1** and **2** compared to the phenoxazine derivatives, the electron density of the HOMO was found to be partially

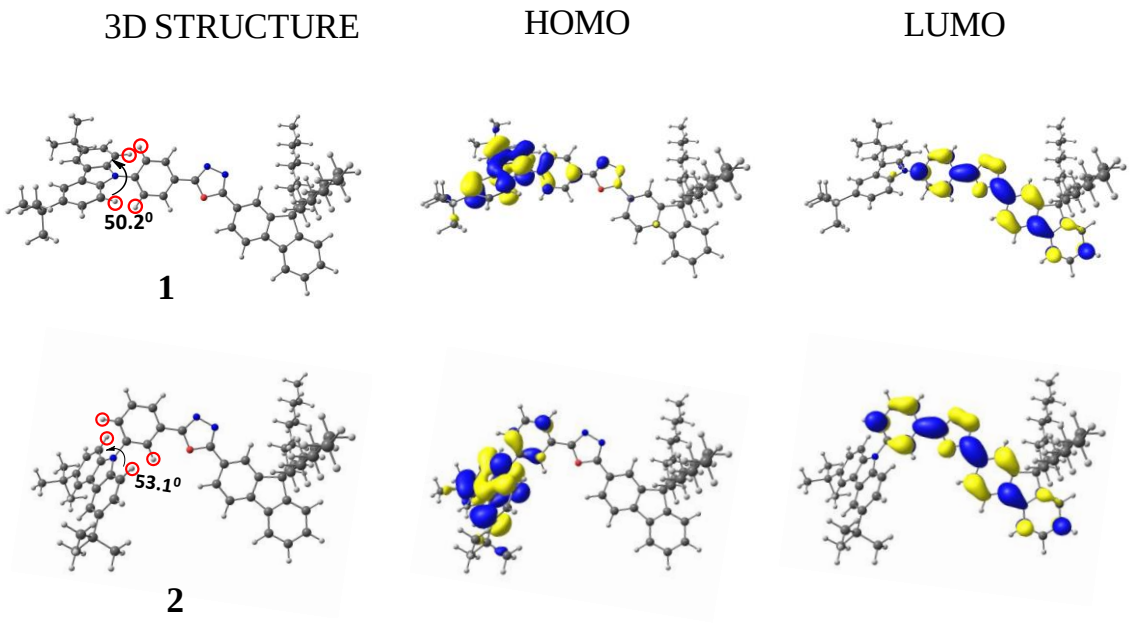

Figure 3.12. HOMO and LUMO of the dyads **1** and **2** calculated at the B3LYP/6-311G (d,p) level.

overlaped to the phenylene linker and which resulted a higher radiative transition for these dyads. The non-bonded H...H steric repulsion owing to the close proximity between C-H bonds of the phenyl rings of donor moiety and N-connected phenyl ring is responsible for the twisted configuration. The HOMO/LUMO values for these dyads **1** and **2** were found to 5.59 and 5.60 / 2.09 and 2.11 eV (Table 3.6).

Table 3.6. Physical and electrochemical data of the dyads **1** and **2**.

Dyads	HOMO/LUMO /ΔE (eV)[a]	HOMO/LUMO /ΔE (eV)[b]	θ_d[b] (°C)	Mp/T_d (°C)
1	5.62/2.43/3.19	5.59/2.09/3.50	50.2	151/390
2	5.61/2.22/3.39	5.60/2.11/3.49	53.1	159/375

[a]Experimentally determined; [b]theoretically calculated; ΔE: energy gap between HOMO and LUMO; θ_d: dihedral angle; Mp: melting point; T_d: decomposition temperature.

3.3.4. Device fabrication

To evaluate the utility of the dyads **1** and **2** in device applications, un-doped OLEDs were fabricated with device configuration having ITO (120 nm)/ Poly(3,4-ethylene-dioxythiophene)-poly(styrenesulfonate) (PEDOT: PSS) (40 nm)/ **1** or **2** (50 nm)/ TPBi (40 nm)/ LiF (1 nm)/ Al (100 nm) as shown in the Figure 3.13. Here, ITO was used as a transparent anode, PEDOT: PSS as the hole injection layer, TPBi as the hole-blocking layer, LiF as the electron-injecting layer and Al as cathode. Figure 3.14 presents current density-voltage, current

density-luminance, current density-current efficiency and electroluminescence (EL) characteristics of the devices fabricated.

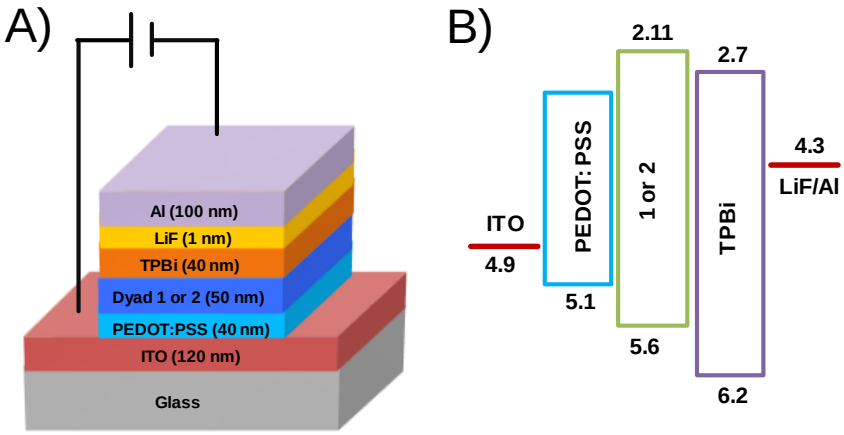

Figure 3.13. A) Device structure and B) energy level diagram of the un-doped solution processed OLEDs fabricated using the dyads **1** and **2**.

The devices exhibited good diode behaviour with the turn on voltage (V_{onset}) of 6.48 and 6.90 V for the dyads **1** and **2**, respectively. The devices based on both dyads **1** and **2** showed deep blue electroluminescence in near ultraviolet (NUV) region having λ_{max} at 410 nm and 408 nm with a narrow FWHM of 54 and 49 nm and CIE coordinates of (0.16, 0.07) and (0.16, 0.05), respectively, which is of very good colour purity (Figure 3.15). Interestingly, the EL spectra of devices showed almost the same maximum wavelength as photoluminescence spectra in the spin coated films. This indicates that, an unsymmetrical structure with long alkyl chain could be able to effectively reduce the possibilities of aggregation and helped the formation of a homogeneous amorphous film by solution processing. The devices of the dyads **1** and **2** showed a maximum luminance of *ca.* 62.17 and 61.45 cd m^{-2} with a current efficiency of ca. 0.45 and 0.44 cd A^{-1}, respectively (Table 3.7).

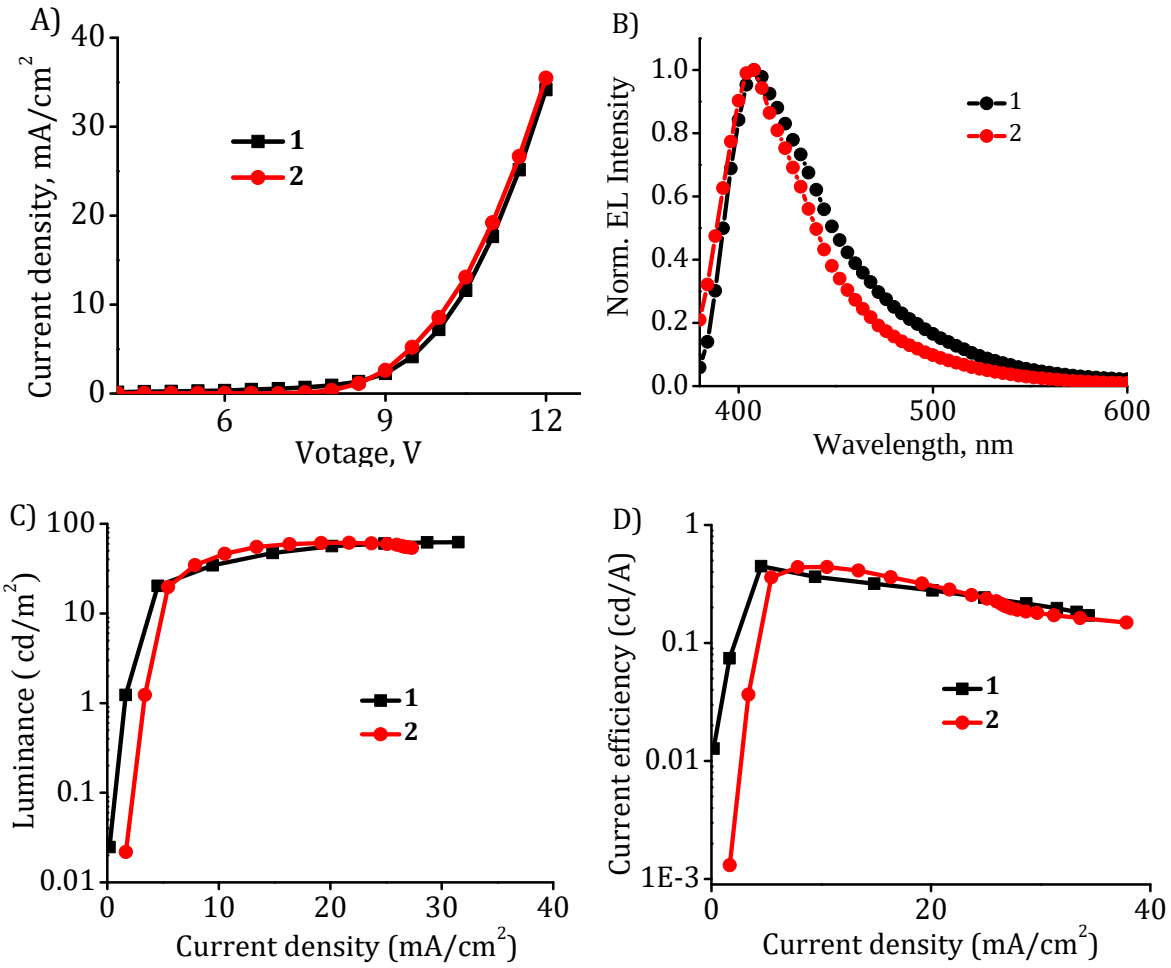

Figure 3.14. A-D) Device characteristics of the un-doped solution processed OLEDs fabricated using the dyads **1** and **2**.

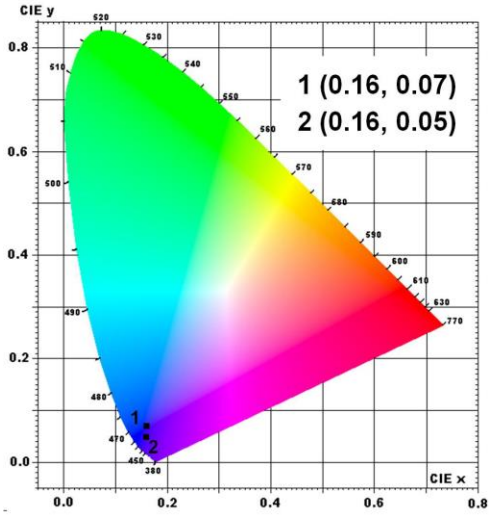

Figure 3.15. CIE coordinates of the emission from devices using dyads **1** and **2.**

Table 3.7. Electroluminescence data of the dyads **1** and **2** in OLED device

Device	V_{onset} (V)	λ_{ems}	CIE coordinates	L_{max} (cd m^{-2})	η_c (cd A^{-1})	η_p (lm W^{-1})
1	6.48	410	(0.16, 0.07)	62.17	0.45	0.18
2	6.90	408	(0.16, 0.05)	61.45	0.44	0.14

V_{onset}: turn-on voltage; λ_{ems}: emission wavelength; L_{max}: maximum luminance; η_c: maximum current efficiency measured; η_p: maximum power efficiency measured. Applied voltage in each case was in the range 11-11.5 V.

As can be seen from Figure 13 (B), there are considerable injection barriers for the holes and electrons. There is an injection barrier of 0.5 V for holes between HTL and EML and the injection barrier for the electrons between cathode and ETL was 1.6 eV. Such large injection barriers are responsible for the observed higher turn on voltage. A very low value of the current density even at high voltage corroborates this point of view. In fact, the low LUMO of 2.11 eV was making it difficult to find a suitable ETL. These observations clearly indicate that there is a large scope for optimization of various parameters required including the injection barriers by suitable buffer layers or doped transport layers to improve the device performance.

3.4. Conclusions

In summary, we have synthesized and characterized two deep blue emitters **1** and **2** based on D-π-A structure that combine carbazole and oxadiazole moieties and have investigated their photphysical, thermal, electrochemical and morphological

properties under different conditions. Both the dyads **1** and **2** showed favorable photophysical properties and excellent thermal stability, solution processability and film morphologies. The solution processed un-doped OLEDs fabricated based on the dyads **1** and **2** showed deep blue electroluminescence in NUV region with excellent blue color purity having λ_{max} at 410 nm and 408 nm and a narrow FWHM of 54 and 49 nm and CIE coordinates of (0.16, 0.07) and (0.16, 0.05), respectively. We observed a maximum luminance of ca. 62.17 and 61.45 cd m^{-2} with a current efficiency of ca. 0.45 and 0.44 cd A^{-1} for the devices based on the dyads **1** and **2**, respectively, thereby demonstrating their potential use in OLEDs.

3.5. Experimental section

3.5.1. General techniques

The melting points were determined on a Mel-Temp II melting point apparatus. The electronic absorption spectra were recorded on a Shimadzu UV-3101 or 2401 PC UV-VIS-NIR scanning spectrophotometer. The fluorescence spectra were recorded on a SPEX-Fluorolog F112X spectrofluorimeter. Film-state photoluminescence was measured using the front face emission scan mode on a SPEX Fluorolog F112X spectrofluorimeter. Measurements of solution state and film-state fluorescence quantum efficiency were carried out using a calibrated integrating sphere in a SPEX Fluorolog spectrofluorimeter. A Xenon-arc lamp was used to excite the film samples placed in the sphere, with 330 nm as the excitation wavelength. This experimental setup and the integrating sphere

system calibrated using the solid state fluorescence quantum yield of the standard sodium salicylate (white powder) was determined to be 60 ± 10%, which is consistent with previously reported values. Fluorescence lifetimes were measured using an IBH (Fluoro Cube) time correlated picosecond single photon counting (TCSPC) system.

CIE, Commission International de l'Eclairage (International Commission on Illumination), chromaticity coordinates (1931) (x, y) were calculated using HORIBA Jobin Yvon Color Calculator provided with integrating sphere. Thermal stability measurements were performed at a heating rate of 10°C/min in a nitrogen atmosphere using Shimadzu, DTG-60 equipment. Cyclic voltammetry is done by CV-50w electro analyzer in DCM using Pt wire as auxiliary electrode, glassy carbon as working electrode. The potential were referenced to the standard Ag/AgCl electrode and ferrocene was used as external standard. ^{1}H NMR was recorded on a 500 MHz Bruker advanced DPX spectrometer. Mass spectra were recorded either on a JEOL AX503 (HRMS) or Shimadzu Biotech Axima CFR plus instrument. The AFM studies were carried out Bruker nanoscope V multimode 8 AFM. All experiments were carried out at room temperature (25±1 °C), unless otherwise mentioned.

The geometry of the dyads **1** and **2** were optimized with B3LYP/6-311G (d,p) level density functional theory in conjunction with polarized continuum model (PCM) solvation method (selected solvent is toluene) as implemented in Gaussian 09 package. Vibrational frequency calculations were carried out on **1**

and **2** at the same level of theory and verified them as true minima on the potential energy surface (number of imaginary frequency = 0).

The electroluminescence properties of the molecules were studied by fabricating un-doped OLEDs by solution processing. The ETL and cathode were deposited using thermal evaporation at a base pressure of 10^{-8} Torr. Patterned ITO coated glass substrates with a sheet resistance of 10 Ω/sq were used as anodes, which were cleaned with detergent, chloroform, isopropanol and de-ionized water and UV–Ozone treated. On the ITO substrate, the HIL, emitting layer, ETL, EIL, and cathode were deposited sequentially without exposing to atmosphere inside glove box. The deposition rate of TPBi and Al was maintained at 2 Å s^{-1}, whereas the deposition rates of LiF were 0.1 Å s^{-1}. The deposition rate and thickness of the deposited layers were controlled in situ by a quartz crystal thickness monitor. The cathode was deposited on the top of the structure through a shadow mask. The devices were encapsulated using UV curable epoxy inside the glove box. The EL spectra, J–V characteristics of the devices were measured using a spectrophotometer and a source meter interfaced to a computer. All of the measurements were carried out at room temperature.

3.5.2. Materials and methods

All the reagents used for synthesis and measurements were purchased from Sigma Aldrich or Alfa Aesar, in analytical grade and used as received, unless otherwise stated. TPBi was purchased from LumTec and Aluminium from Kurt J. Lesker. The synthesis of 2-(4-bromophenyl)-5-(9,9-dioctyl-9H-fluoren-2-yl)-1,3,4-oxadiazol (**7a**)

and 2-(3-bromophenyl)-5-(9,9-dioctyl-9H-fluoren-2-yl)-1,3,4-oxadiazole (**7b**) were discussed in the Chapter 2.

3.5.3. Synthesis and characterization

2-(4-(3,6-Di-tert-butyl-9H-carbazol-9-yl)phenyl)-5-(9,9-dioctyl-9H-fluoren-2-yl)-1,3,4-oxadiazole (1). A mixture of 2-(4-bromophenyl)-5-(9,9-dioctyl-9H-fluoren-2-yl)-1,3,4-oxadiazol (**7a**) (1 g, 1.633 mmol), 3,6-di-tert-butyl-9H-carbazole (1.37 g, 4.9 mmol), Cs_2CO_3 (3.73 g, 1.143 mmol), $Pd(OAc)_2$ (37 mg, 0.1633 mmol) and $P(t\text{-}Bu)_3$ (100 mg, 0.49 mmol) in toluene (30 mL) was heated at 40 °C for 2 h and then the reaction mixture heated at 110 °C for 24 h. The mixture was cooled to room temperature and water and chloroform were added. The organic layer was separated and solvent was removed under reduced pressure. The product **1** was purified by column chromatography over silica gel using a mixture of ethyl acetate and hexane (5:95) and the product was recrystallized from hexane to give 1.1 g (83%) of white crystals of the dyad **1**. ^{1}H NMR (500 MHz, $CDCl_3$, TMS) δ 0.62 (d, 4H, J = 6 Hz), 0.81 (t, 6H, J = 7 Hz), 1.11 (m, 16H), 1.20 (m, 4H), 1.50 (s, 18H), 2.07 (m, 4H), 7.39 (d, 3H, J = 2.5 Hz), 7.47 (d, 2H, J = 8.5 Hz), 7.51 (m, 2H), 7.78 (m, 3H), 7.85 (d, 1H, J = 8 Hz), 8.16 (t, 4H, J = 4 Hz), 8.41 (d, 2H, J = 8.5Hz). ^{13}C NMR (125 MHz, $CDCl_3$) 165.44, 163.98, 151.70, 151.45, 144.97, 143.63, 141.38, 139.86, 138.63, 128.53, 128.36, 127.08, 126.72, 126.08, 123.89, 123.87, 123.07, 122.12,

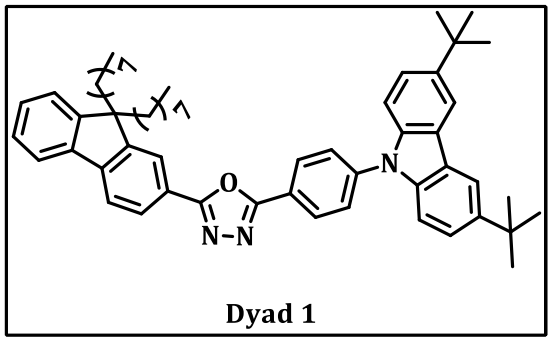

Dyad 1

122.04, 121.34, 120.49, 120.26, 116.45, 109.23, 55.51, 40.31, 34.80, 31.99, 31.76, 29.97, 29.23, 29.19, 23.78, 22.58, 14.05. ESIMS: Calcd for $C_{57}H_{69}N_3O$, 811.54; Found, 812.55 ($M^+ + 1$).

2-(3-(3,6-di-tert-butyl-9H-carbazol-9-yl)phenyl)-5-(9,9-dioctyl-9H-fluoren-2-yl)-1,3,4-oxadiazole (2). A mixture of 2-(3-bromophenyl)-5-(9,9-dioctyl-9H-fluoren-2-yl)-1,3,4-oxadiazole (**7b**) (1 g, 1.633 mmol), *3,6-di-tert-butyl-9H-carbazole* (1.37 g, 4.9 mmol), Cs_2CO_3 (3.73 g, 1.143 mmol), $Pd(OAc)_2$ (37 mg, 0.1633 mmol) and $P(tBu)_3$ (100 mg, 0.49 mmol) in toluene (30 mL) was heated at 40 °C for 2 h and then the reaction mixture was heated at 110 °C for 24 h. The mixture was cooled to room temperature and water and chloroform were added. The organic layer was separated and solvent was removed under reduced pressure. The product **2** was purified by column chromatography over silica gel using a mixture of ethyl acetate and hexane (5:95) and on crystallization from hexane gave 1.05 g (79%) of white crystals of the dyad **2**.^{1}H NMR (500 MHz, $CDCl_3$, TMS) δ 0.59 (d, 4H, J = 6.5 Hz), 0.78 (t, 6H, J = 7 Hz), 1.07 (m, 16H), 1.16 (m, 4H), 1.50 (s, 18H), 2.04 (m, 4H), 7.37 (t, 3H, J = 2.5 Hz), 7.41 (d, 2H, J = 8.5 Hz), 7.51 (m, 2H), 7.76 (m, 3H), 7.83 (d, 1H, J = 8.5 Hz), 8.10 (m, 2H), 8.18 (s, 2H), 8.28 (m, 1H), 8.36 (s, 1H). ^{13}C NMR (125 MHz, $CDCl_3$) 165.62, 163.80, 151.70, 151.45, 145.03, 143.39, 139.84, 139.23, 139.09, 130.74, 129.89, 128.35, 127.06, 126.16, 125.93,125.49, 125.08, 123.89, 123.63, 123.05, 121.98, 121.36, 120.48, 120.23, 116.43, 109.08, 55.52, 40.25, 34.80, 32.02,

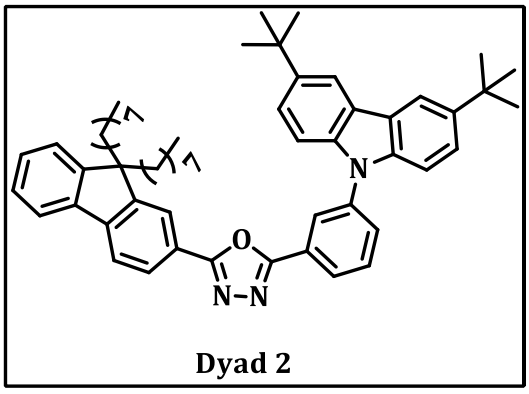

Dyad 2

31.74, 29.93, 29.21, 29.17, 23.76, 22.57, 14.05. ESIMS: Calcd for $C_{57}H_{69}N_3O$, 811.54; Found, 812.55 (M^+ +1).

3.6. References

(1) (a) Kuo, H.-H.; Chen, Y.-T.; Devereux, L. R.; Wu, C.-C.; Fox, M. A.; Kuei, C.-Y.; Chi, Y.; Lee, G.-H. *Adv. Mater.* **2017**, *29*, 1702464(b) Kamtekar, K. T.; Monkman, A. P.; Bryce, M. R. *Adv Mater* **2010**, *22*, 572.

(2) (a) Janghouri, M.; Adineh, M. *J. Photochem. Photobiol. A Chem.* **2017**, *341*, 31(b) Shanmugasundaram, M.; Joseph, J.; Ramaiah, D. *J. Photochem. Photobiol. A Chem.* **2016**, *330*, 156(c) Ning, Z.; Zhou, Y.; Zhang, Q.; Ma, D.; Zhang, J.; Tian, H. *J. Photochem. Photobiol. A Chem.* **2007**, *192*, 8.

(3) de Deus, J. F.; Faria, G. C.; Faria, R. M.; Iamazaki, E. T.; Atvars, T. D. Z.; Cirpan, A.; Akcelrud, L. *J. Photochem. Photobiol. A Chem.* **2013**, *253*, 45.

(4) (a) Tao, Y.; Yang, C.; Qin, J. *Chem. Soc. Rev.* **2011**, *40*, 2943(b) Zhang, T.; Liang, Y.; Cheng, J.; Li, J. *J. Mater. Chem. C* **2013**, *1*, 757.

(5) (a) Yao, L.; Zhang, S.; Wang, R.; Li, W.; Shen, F.; Yang, B.; Ma, Y. *Angew. Chem. Int. Ed.* **2014**, *53*, 2119(b) Prachumrak, N.; Pojanasopa, S.; Namuangruk, S.; Kaewin, T.; Jungsuttiwong, S.; Sudyoadsuk, T.; Promarak, V. *ACS Appl. Mater. Interfaces* **2013**, *5*, 8694(c) Liu, B.; Xu, M.; Tao, H.; Ying, L.; Zou, J.; Wu, H.; Peng, J. *J. Lumin.* **2013**, *142*, 35(d) Fukagawa, H.; Shimizu, T.; Hanashima, H.; Osada, Y.; Suzuki, M.; Fujikake, H. *Adv. Mater.* **2012**, *24*, 5099.

(6) Yang, R. Y.; Li, X. M.; Cao, X. A. *J. Appl. Phys.* **2017**, *122*, 075501.

(7) (a) Kim, B. S.; Lee, J. Y. *Adv. Funct. Mater.* **2014**, *24*, 3970(b) Tsai, M. H.; Lin, H. W.; Su, H. C.; Ke, T. H.; Wu, C. c.; Fang, F. C.; Liao, Y. L.; Wong, K. T.; Wu, C. I. *Adv. Mater.* **2006**, *18*, 1216.

(8) Jou, J.-H.; Kumar, S.; Agrawal, A.; Li, T.-H.; Sahoo, S. *J. Mater. Chem. C* **2015**, *3*, 2974.

(9) (a) Gong, J.-R.; Wan, L.-J.; Lei, S.-B.; Bai, C.-L.; Zhang, X.-H.; Lee, S.-T. *J. Phys. Chem. B* **2005**, *109*, 1675(b) Zhong, G. Y.; Xu, Z.; He, J.; Zhang, S. T.; Zhan, Y. Q.; Wang, X. J.; Xiong, Z. H.; Shi, H. Z.; Ding, X. M.; Huang, W.; Hou, X. Y. *Appl. Phys. Lett.* **2002**, *81*, 1122.

(10) Kamtekar, K. T.; Wang, C.; Bettington, S.; Batsanov, A. S.; Perepichka, I. F.; Bryce, M. R.; Ahn, J. H.; Rabinal, M.; Petty, M. C. *J. Mater. Chem.* **2006**, *16*, 3823.

(11) Farinola, G. M.; Ragni, R. *Chem. Soc. Rev.* **2011**, *40*, 3467.

(12) Duan, L.; Hou, L.; Lee, T.-W.; Qiao, J.; Zhang, D.; Dong, G.; Wang, L.; Qiu, Y. *J. Mater. Chem.* **2010**, *20*, 6392.

(13) Duan, L.; Qiao, J.; Sun, Y.; Qiu, Y. *Adv. Mater.* **2011**, *23*, 1137.

(14) (a) Hladka, I.; Lytvyn, R.; Volyniuk, D.; Gudeika, D.; Grazulevicius, J. V. *Dyes Pigm.* **2018**, *149*, 812(b) Kukhta, N. A.; Matulaitis, T.; Volyniuk, D.; Ivaniuk, K.; Turyk, P.; Stakhira, P.; Grazulevicius, J. V.; Monkman, A. P. *J. Phys. Chem. Lett.* **2017**, *8*, 6199(c) Chercka, D.; Yoo, S.-J.; Baumgarten, M.; Kim, J.-J.; Mullen, K. *J. Mater. Chem. C* **2014**, *2*, 9083(d) Zhang, Y.; Jin, Y.; Bai, R.; Yu, Z.; Hu, B.; Ouyang, M.; Sun, J.; Yu, C.; Liu, J.; Zhang, C. *J. Photochem. Photobiol. A Chem.* **2012**, *227*, 59(e) Michaleviciute, A.; Gurskyte, E.; Volyniuk, D. Y.; Cherpak, V. V.; Sini, G.; Stakhira, P.

Y.; Grazulevicius, J. V. *J. Phys. Chem. C* **2012**, *116*, 20769(f) Kim, S. H.; Cho, I.; Sim, M. K.; Park, S.; Park, S. Y. *J. Mater. Chem.* **2011**, *21*, 9139.

(15) (a) Grybauskaite-Kaminskiene, G.; Ivaniuk, K.; Bagdziunas, G.; Turyk, P.; Stakhira, P.; Baryshnikov, G.; Volyniuk, D.; Cherpak, V.; Minaev, B.; Hotra, Z.; Ågren, H.; Grazulevicius, J. V. *J. Mater. Chem. C* **2018**, *6*, 1543(b) Deksnys, T.; Simokaitiene, J.; Keruckas, J.; Volyniuk, D.; Bezvikonnyi, O.; Cherpak, V.; Stakhira, P.; Ivaniuk, K.; Helzhynskyy, I.; Baryshnikov, G.; Minaev, B.; Grazulevicius, J. V. *New J. Chem.* **2017**, *41*, 559(c) Baryshnikov, G. V.; Gawrys, P.; Ivaniuk, K.; Witulski, B.; Whitby, R. J.; Al-Muhammad, A.; Minaev, B.; Cherpak, V.; Stakhira, P.; Volyniuk, D.; Wiosna-Salyga, G.; Luszczynska, B.; Lazauskas, A.; Tamulevicius, S.; Grazulevicius, J. V. *J. Mater. Chem. C* **2016**, *4*, 5795(d) Bucinskas, A.; Volyniuk, D.; Danyliv, Y.; Grazulevicius, J. V.; Baryshnikov, G.; Minaev, B.; Ivaniuk, K.; Cherpak, V.; Stakhira, P. *RSC Adv.* **2015**, *5*, 78150(e) Boudreault, P.-L. T.; Beaupre, S.; Leclerc, M. *Polym. Chem.* **2010**, *1*, 127.

(16) Ono, K.; Joho, M.; Saito, K.; Tomura, M.; Matsushita, Y.; Naka, S.; Okada, H.; Onnagawa, H. *Eur. J. Inorg. Chem.* **2006**, *2006*, 3676.

(17) (a) Tsuie, B.; L. Reddinger, J.; A. Sotzing, G.; Soloducho, J.; R. Katritzky, A.; R. Reynolds, J. *J. Mater. Chem.* **1999**, *9*, 2189(b) Vyas, P. V.; Bhatt, A. K.; Ramachandraiah, G.; Bedekar, A. V. *Tet. Lett.* **2003**, *44*, 4085(c) Wong, K.-T.; Ku, S.-Y.; Cheng, Y.-M.; Lin, X.-Y.; Hung, Y.-Y.; Pu, S.-C.; Chou, P.-T.; Lee, G.-H.; Peng, S.-M. *J. Org. Chem.* **2006**, *71*, 456(d) Reddy, M. A.; Thomas, A.; Srinivas, K.; Rao, V. J.; Bhanuprakash, K.; Sridhar, B.; Kumar, A.; Kamalasanan, M. N.; Srivastava, R. *J. Mater. Chem.* **2009**, *19*, 6172.

(18) (a) Feng, X. J.; Chen, S. F.; Ni, Y.; Wong, M. S.; Lam, M. M. K.; Cheah, K. W.; Lai, G. Q. *Org. Electron.* **2014**, *15*, 57(b) Huang, H.; Wang, Y.; Pan, B.; Yang, X.; Wang, L.; Chen, J.; Ma, D.; Yang, C. *Chem. Eur. J.* **2013**, *19*, 1828.

(19) Tao, Y.; Wang, Q.; Yang, C.; Zhong, C.; Zhang, K.; Qin, J.; Ma, D. *Adv. Funct. Mater.* **2010**, *20*, 304.

(20) Kaafarani, B. R.; El-Ballouli, A. a. O.; Trattnig, R.; Fonari, A.; Sax, S.; Wex, B.; Risko, C.; Khnayzer, R. S.; Barlow, S.; Patra, D.; Timofeeva, T. V.; List, E. J. W.; Bredas, J.-L.; Marder, S. R. *J. Mater. Chem. C* **2013**, *1*, 1638.

(21) Ishimatsu, R.; Matsunami, S.; Shizu, K.; Adachi, C.; Nakano, K.; Imato, T. *J. Phys. Chem. A* **2013**, *117*, 5607.

(22) Kim, S. Y.; Cho, Y. J.; Lee, A. R.; Son, H. J.; Han, W. S.; Cho, D. W.; Kang, S. O. *Phys. Chem. Chem. Phys.* **2016**, *19*, 426.

Chapter 4

Design of Quinoline–Carbaldehyde Chemosensor and Investigation of Metal Ion Recognition Properties

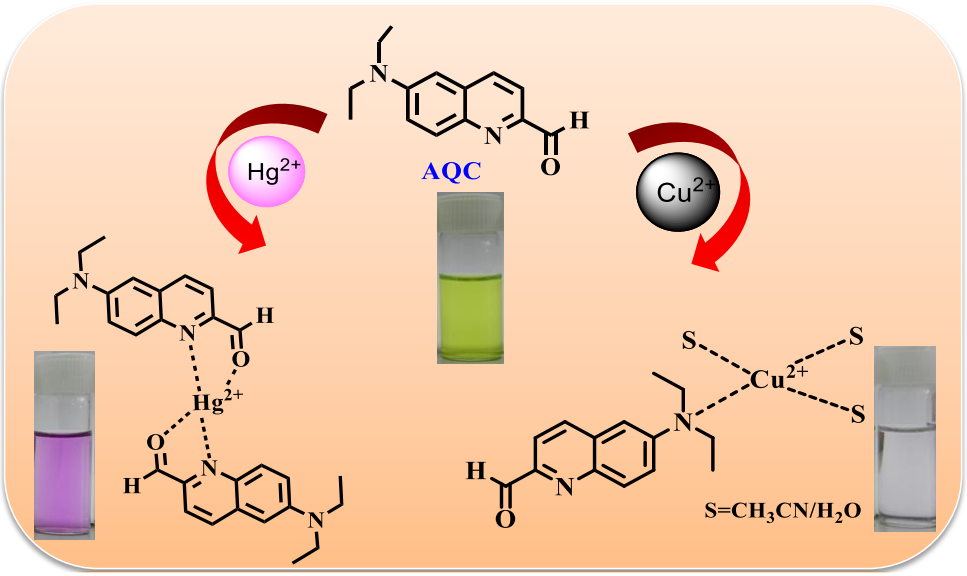

4.1. Abstract

With an objective to develop new colorimetric chemosensor based on organic donor-acceptor small molecules, we designed a quinoline–carbaldehyde probe, 6-diethylaminoquinoline-2-carbaldehyde (**AQC**) and have investigated its sensing behavior towards various metal ions through photophysical, IR and NMR techniques. The probe **AQC** has a donor diethylamino group and acceptor carbaldehyde moiety and hence exhibited intramolecular charge transfer (ICT) properties. From the DFT calculations, the HOMO of **AQC** was found to be delocalized over the entire molecule while in the LUMO, the electron density was localized mostly on the quinoline and

carbaldehyde group. The probe **AQC**, in acetonitrile solution, showed absorption maximum at 412 nm having a shoulder at 365 nm and intense band at 290 nm. It exhibited fluorescence maximum at 506 nm with a fluorescence quantum yield of *ca.* 0.40. When the solvent polarity was increased from cyclohexane to methanol, the absorption maximum was bathochromically shifted by *ca*. 15 nm, while a red-shift of *ca*. 114 nm was observed in the fluorescence spectrum.

We have investigated the interactions of the probe **AQC** with various biologically and environmentally relevant metal ions. The probe can selectively detect both Cu^{2+} and Hg^{2+} ions with an easy, well-defined naked eye visible color changes from yellow to colorless and yellow to pink, respectively. With the successive addition of Cu^{2+} ions, the absorption bands of **AQC** at 290, 365 and 412 nm showed hypochromicity with the concomitant formation of new peaks at 324 and 530 nm and isosbestic points at 343 and 464 nm. Similarly with the addition of Hg^{2+} ions, the bands at 290, 365 and 412 nm showed hypochromicity with the formation of new intense bands at 324 and 537 nm and isosbestic points at 343 and 464 nm. This probe exhibited a stable 1:1 stoichiometric complex involving diethylamino moiety for the selective recognition of Cu^{2+} ions with a detection limit of 25 ppb. For the selective recognition of Hg^{2+} ions, it formed a 2:1 stoichiometric complex involving quinoline nitrogen and aldehyde functionality and showed a detection limit of 360 ppb. The association constants for both Cu^{2+} and Hg^{2+} complexes were determined to be *ca.* $2.1 \pm 0.1 \times 10^4$ M^{-1} and $1.29 \pm 0.2 \times 10^8$ M^{-2}, respectively. Uniquely, this probe can be coated on a glass surface to fabricate a simple solid state dipstick device that can be used for the easy visual detection and analysis of Cu^{2+} and Hg^{2+} ions in the aqueous medium.

4.2. Introduction

Design of organic conjugated small molecule-based chemosensors for the naked eye detection and quantification of important physiological and environmental transition metal ions such as Hg^{2+}, Cu^{2+} and related cations has been an active area of research.[1] Of all the metal ions, Hg^{2+} ion is a well-known global pollutant and remains as a threat to human health.[2] Exposure of human body to even a low concentration of Hg^{2+} ions can lead to neurological diseases, cognitive and motion disorders, and damage to the prenatal brain, digestive system and kidneys.[3] The source of pollution of mercury is by means of oceanic and volcanic emission, gold mining, solid waste incineration, combustion of fossil fuels and the chlor alkali industry. Furthermore, the water soluble Hg^{2+} ions as well as highly toxic organomercury CH_3Hg^{2+} are of serious environmental concern. With regard to Cu^{2+} ions, though they play crucial role in various biological processes,[4] excess concentrations of these ions can be highly toxic. Cu^{2+} ions are also capable of retarding many enzyme-catalyzed reactions by displacing other metal ions and act as co-factor.[5] Deficiency of Cu^{2+} ions can lead to Menkes disease, while high levels can cause Alzheimer or Wilson disease, gastrointestinal disorders and kidney damage[6]. Therefore, the development of molecular probes that can detect these metal ions with high selectivity and sensitivity through naked eye is quite important.

Of the various probes, the colorimetric chemosensors are especially attractive, because the analyte determination can be carried out by the naked eye under visible light.[7] Although a large variety of selective single[8] as well as multianalyte[9] chemosensors have been reported, the development of a simple chemosensor for

multiple metal ions using a single technique through displaying distinct outputs is desirable. Of the several chromophores reported, the quinolines based systems have been utilized for the detection of various alkali, alkaline earth and transition metal ions. Among them, 8-hydroxy-2-methylquinoline has been well exploited as a chelator and which was widely used for recognizing a variety of metal ions[10]. Even though, several quinoline derivatives were synthesized and used as chemosensors, the use of simple quinoline-2-carboxaldehyde directly as a sensor has not been exploited. Herein, we have chosen 6-diethylaminoquinoline-2-carbaldehyde (**AQC**) as a probe and investigated its interactions with various mono- and divalent metal ions as compared to the model compound, 6-ethoxyquinoline-2-carbaldehyde (**EQC**) (Chart 4.1). The **AQC** exhibited high sensitivity and selectivity for both Cu^{2+} and Hg^{2+} ions and signalled the event through visible color changes when compared to other metal ions and the model compound **EQC**. The probe **AQC** can also be coated on a glass surface to fabricate a solid state dipstick device that can be used for the easy visual detection and onsite analysis of Cu^{2+} and Hg^{2+} ions in the aqueous medium.

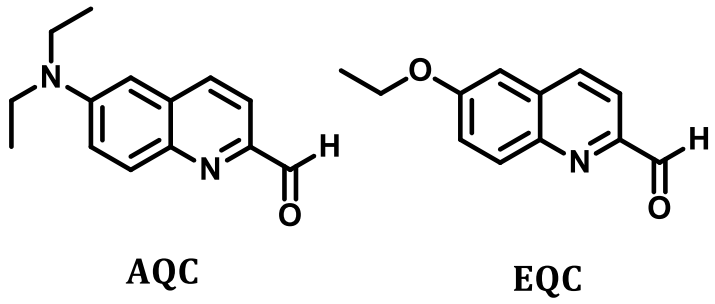

AQC **EQC**

Chart 4.1. Chemical structures of probe **AQC** and model compound **EQC**.

4.3. Results and Discussion

4.3.1. Synthesis and photophysical properties of the probe

The probe **AQC** was prepared from 6-nitroquinaldine *via* a three step procedure by using the modified reported procedure (Scheme 4.1).[11] 6-Nitroquinaldine was reduced with $SnCl_2$/HCl to obtain 6-aminoquinaldine, which was further treated with ethyl iodide to obtain 6-diethylaminoquinaldine. Subsequently on oxidation with SeO_2 in dioxane gave the corresponding aldehyde, **AQC** in *ca.* 74% yield. The model compound, **EQC** was synthesized starting from 6-hydroxy-2-quinaldine as per the reported procedure.[7e]

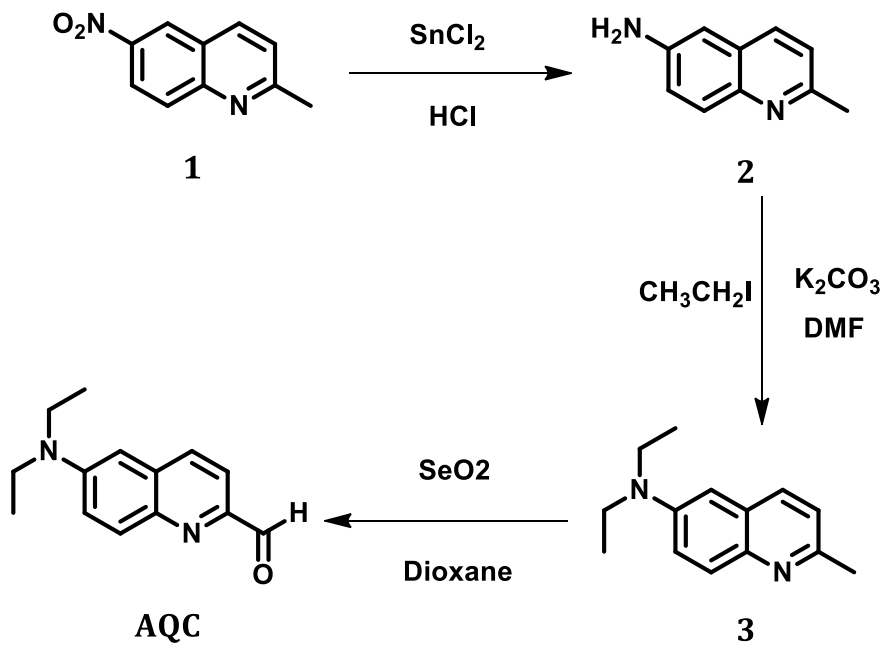

Scheme 4.1. Synthetic route to the probe **AQC**.

The probe **AQC** having the donor diethylamino group and acceptor carbaldehyde moiety was so designed that it can, in principle exhibit an intramolecular charge

transfer (ICT) band, which in turn can be utilized for the detection of various metal ions. We have carried out the theoretical calculations using density functional theory (DFT) with the Gaussian 09 program. The geometry optimization of the probe **AQC** has been performed at the DFT-B3LYP/6-311G (d,p) level. As shown in Figure 1, HOMO of **AQC** interestingly is delocalized over the entire molecule and while in LUMO, the electron density is localized mostly on the quinoline and carbaldehyde groups confirming thereby the possibility of charge transfer in the excited state of the probe.

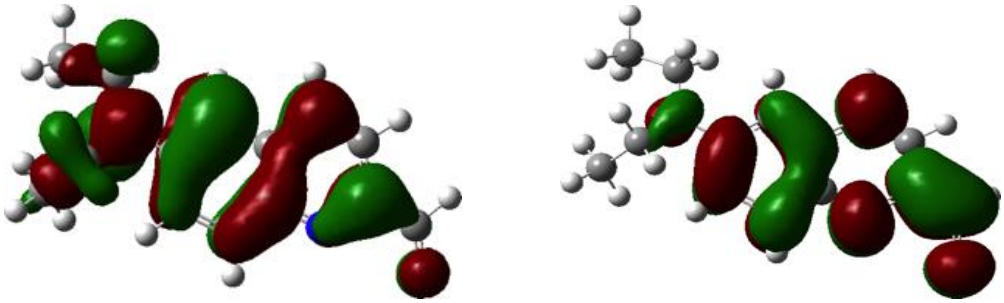

Figure 4.1. HOMO and LUMO orbital pictures of the probe **AQC**.

To further evidence the existence of the excited state intramolecular charge transfer mechanism, we have studied the photophysical properties of the probe **AQC** in solvents having different polarity. Figure 4.2 shows the UV-Vis and fluorescence spectra of the probe **AQC** recorded in different organic solvents. For example, the UV-Vis spectrum of **AQC** in acetonitrile showed the maximum at 412 nm with a shoulder at 365 nm and intense band at 290 nm (Figure 4.2A). When the solvent polarity was increased from nonpolar cyclohexane to polar methanol, the absorption maximum values of the probe **AQC** were bathochromically shifted by *ca*. 15 nm (Table 4.1). Similar studies

were carried for the model compound **EQC**, wherein we observed strong absorption peaks at 263 nm and 339 nm in acetonitrile. As in the case of **AQC**, the model compound **EQC** showed a marginal bathochromic shift of *ca*. 10 nm with the increase in solvent polarity.

The emission spectrum of the probe **AQC** was recorded in various solvents from nonpolar to polar media. The probe displayed a strong fluorescence solvatochromism that was reflected by a large bathochromic shift of its fluorescence emission maximum with the increase in solvent polarity (Figure 4.2B), when compared to the absorption spectral changes. The maximum emission wavelength of **AQC** was red shifted by *ca*. 114 nm, when the solvent was changed from cyclohexane (440 nm) to methanol (554 nm) with a large difference in stokes shift of 2355 cm^{-1} to 6163 cm^{-1}, respectively. Subsequently, we have studied the correlation of the fluorescence band positions of **AQC** with the polarity index $E_T(30)$,[12] for which we observed a good linearity (Table 4.1). We calculated the fluorescence quantum yields (Φ_F) in different solvents by using proflavine hemisulfate (Φ_F = 0.34) as the standard.[13] Interestingly, **AQC** showed relatively high fluorescence quantum yields in all solvents studied ranging from Φ_F = 0.34 to 0.54, except in cyclohexane (0.1) (Table 4.1). Thus, the observed solvent polarity dependent fluorescence properties of the probe **AQC**, confirm the existence of intramolecular charge transfer in the excited state. The fluorescence properties of the model compound **EQC** were studied and which showed weak fluorescence emission when compared to **AQC** under similar conditions.

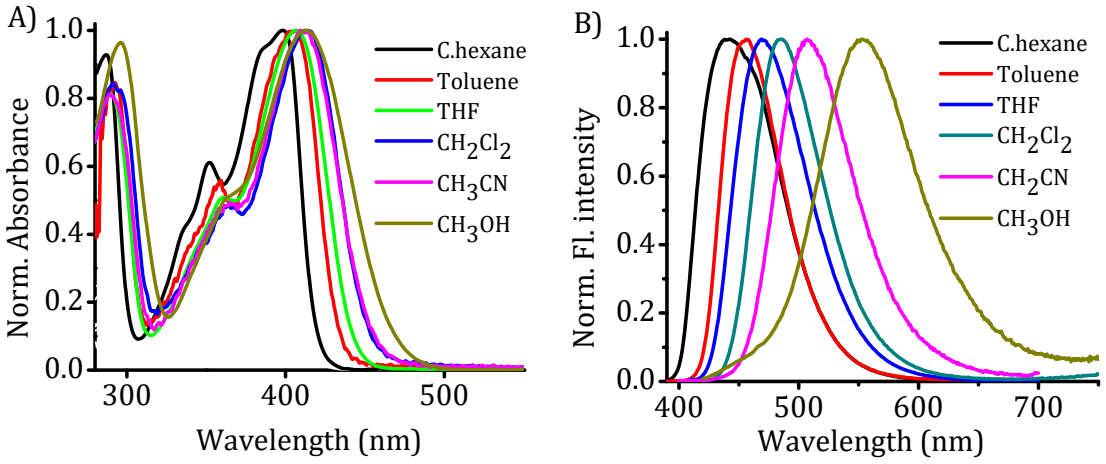

Figure 4.2. Normalized A) absorption and B) fluorescence spectra of the probe **AQC** (10 μM) in different solvents. Excitation at the corresponding absorption maximum (λ_{max}) in the solvent.

Table 4.1. Photophysical properties of the probe **AQC** in different solvents.

Solvent	$E_T(30)^a$ (k cal mol^{-1})	λ_{max} (nm)	$\varepsilon*10^4$ (M^{-1} cm^{-1})	$\lambda_{em}{}^b$ (nm)	$\Phi_F{}^c$	Stokes shift^d (cm^{-1})
C.hexane	30.9	399	2.84	440	0.10	2335
Toluene	33.9	405	1.71	456	0.46	2762
THF	37.4	406	3.02	469	0.46	3309
CH_2Cl_2	40.7	414	3.17	485	0.54	3536
CH_3CN	45.6	412	2.84	506	0.40	4509
CH_3OH	55.4	413	1.86	554	0.34	6163

[a]$E_T(30)$ is the polarity index, [b]emission maximum excited at the corresponding λ_{max}, [c]fluorescence quantum yield relative to proflavine hemisulfate (Φ_F = 0.34 in water). Error ± 10%, [d]Stokes shift = $(1/\lambda_{max} - 1/\lambda_{em})$.

4.3.2. Study of the interactions with metal ions

With an objective to evaluate the potential use of the probe **AQC** as chemosensor, we have investigated its interactions with various monovalent and divalent metal ions through optical spectroscopic techniques. For example, with the increase in concentration of Cu^{2+} ions, we observed a decrease in the absorption bands of **AQC** at 290, 365 and 412 nm with the concomitant formation of new peaks at 324 and 530 nm. We observed isosbestic points at 343 and 464 nm, which clearly indicate the formation of a well-defined **AQC-Cu^{2+}** complex (Figure 4.3A). Upon addition of 1 eq of Cu^{2+} ions, the spectrum reached its maximum decrease in the absorbance at 412 nm with a maximum increase in absorbance at 530 nm. Further addition of Cu^{2+} ions showed negligible spectral changes, indicating 1:1 binding mode between the probe **AQC** and Cu^{2+} ions (Figure 4.3B). These absorption spectral changes enabled the

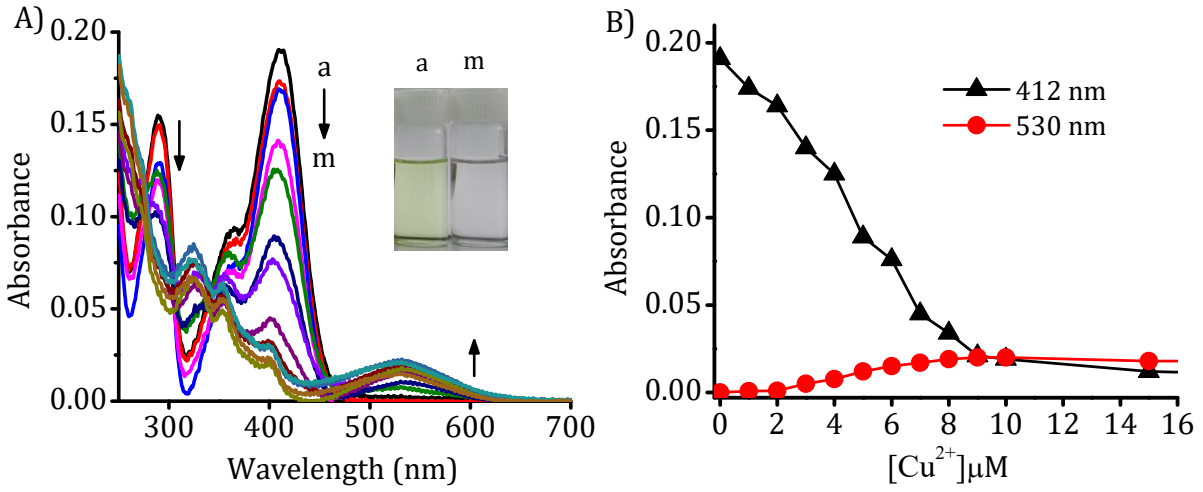

Figure 4.3. A) UV–Vis spectral changes of **AQC** (10 μM) upon addition of Cu^{2+} ions in acetonitrile. (a) 0, (b) 1, (d) 3, (f) 5, (h) 7, (k) 10, (l) 15 and (m) 20 μM. B) Variation in absorbance at 412 and 530 nm with the change in concentration of Cu^{2+} ions.

observation of a colorimetric switching from yellow to colorless by the naked eye (inset of Figure 4.3A) in the presence of Cu^{2+} ions.

Similarly with the addition of Hg^{2+} ions, we observed ratiometric changes in the absorption spectra of the probe **AQC** (Figure 4.4A). The absorption bands of **AQC** at 290, 365 and 412 nm were decreased with the addition of Hg^{2+} ions, subsequently, we observed intense new bands at 324 and 537 nm, with the addition of Hg^{2+} ions along with isosbestic points at 343 and 464 nm. These observations clearly indicate the formation of a well-defined **AQC-Hg^{2+}** complex. Upon addition of 0.5 eq of Hg^{2+} ions, we observed its saturation at 537 nm, indicating 2:1 binding of the probe **AQC** with Hg^{2+} ions (Figure 4.4B). These absorption spectral changes enabled the observation of a colorimetric switching from yellow to pink by the naked eye as shown in the inset of Figure 4.4A for the recognition of Hg^{2+} ions.

To understand the mechanism, we employed the model compound **EQC** and

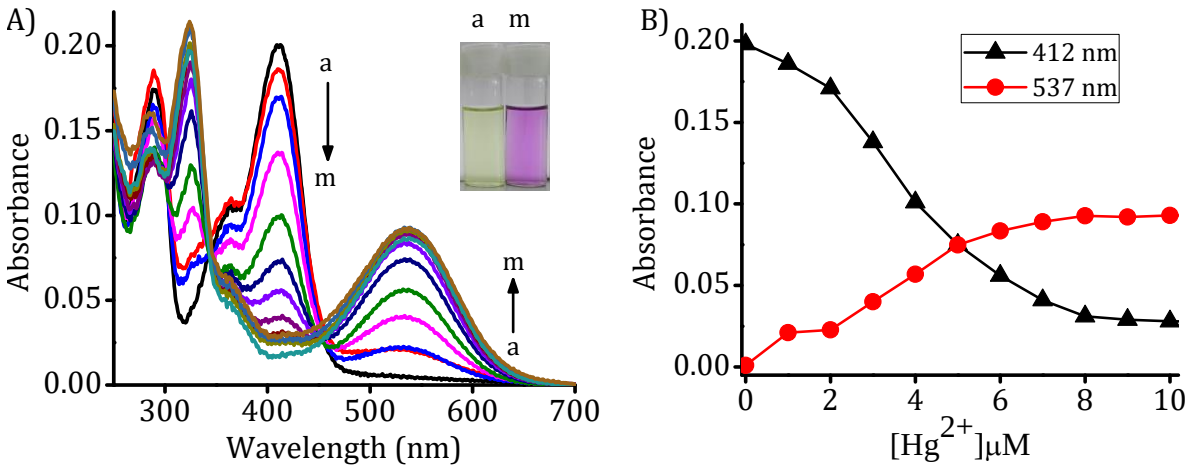

Figure 4.4. A) UV–vis spectral changes of **AQC** (10 µM) upon addition of Hg^{2+} ions in acetonitrile. (a) 0, (b) 1, (d) 3, (f) 5, (h) 7, (k) 10, (l) 15 and (m) 20 µM. B) Variation in the absorbance at 412, 537 nm with the change in concentration of Hg^{2+} ions.

investigated its interactions with different mono and divalent metal ions. For example, with an increase in the concentration of Hg^{2+} ions, we observed a bathochromic shift in the absorption bands at 263 nm and 339 nm of **EQC** with the formation of new distinct bands at 278, 349 and, 389 nm having isosbestic points at 270, 296 and 344 nm (Figure 4.5A). In contrast, **EQC** showed negligible changes in the absorption spectra with the increase in addition of Cu^{2+} ions (Figure 4.5B). These observations demonstrated the importance of the substituents present on the quinaldine moiety, which play a major role for the observed selectivity of the metal ion recognition. In the emission spectrum, the probe **AQC** showed bright green fluorescence at 506 nm in acetonitrile. The fluorescence intensity was found to be quenched with the gradual addition of different concentrations of both Cu^{2+} and Hg^{2+} ions (Figure 4.6). The quenching mechanism could be due to the charge transfer from the probe to the metal ions (LMCT). In addition, the quenching of the fluorescence in the copper coordinated complex may be due to the paramagnetic nature of the Cu^{2+} ions.[14]

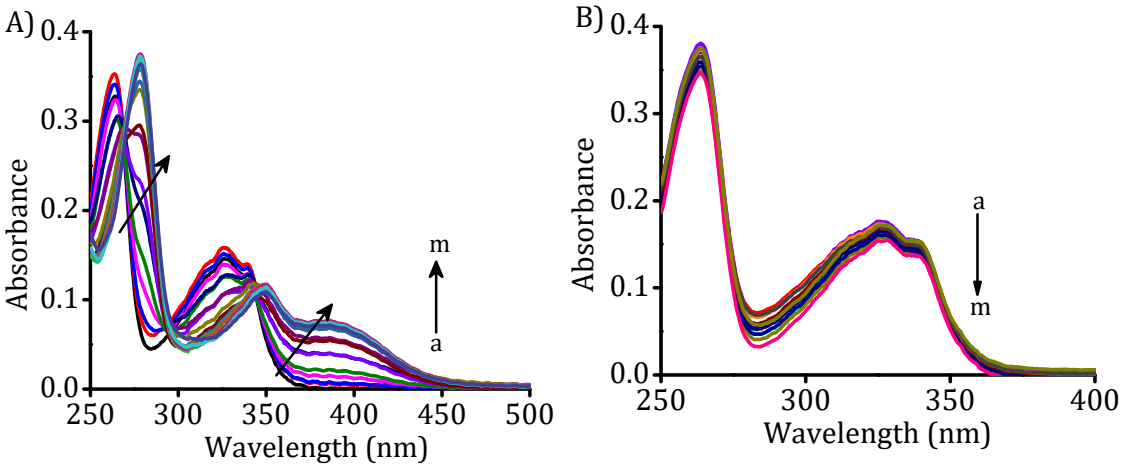

Figure 4.5. UV–Vis spectral changes of the model compound **EQC** (10 μM) upon addition of A) Hg^{2+} and B) Cu^{2+} ions. (a) 0 and (m) 20 μM in CH_3CN.

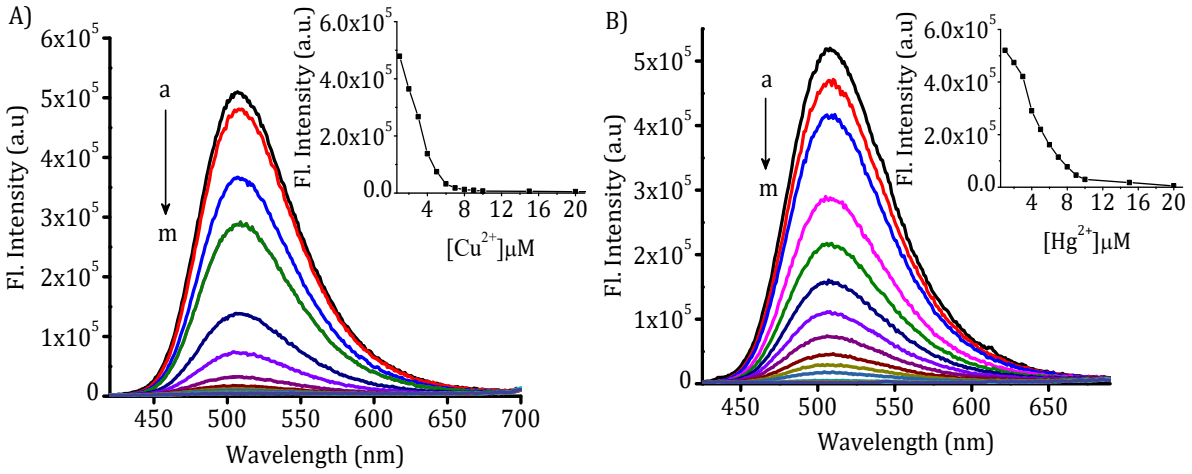

Figure 4.6. Fluorescence spectral changes of **AQC** (10 μM) in CH_3CN on varying the concentration of A) Cu^{2+} and B) Hg^{2+} ions. (a) 0, (m) 20 μM. Insets show the variation in fluorescence intensity at 506 nm under similar conditions. Excitation wavelength, 464 nm.

4.3.3. Selectivity and reversibility of the complexation

To demonstrate the selectivity of the probe **AQC** as a colorimetric chemosensor for Cu^{2+} and Hg^{2+} ions, we have investigated its interactions with other important monovalent and divalent metal ions such as Na^{+}, K^{+}, Ag^{+}, Mg^{2+}, Ca^{2+}, Mn^{2+}, Fe^{2+}, Co^{2+}, Ni^{2+}, Zn^{2+}, Cd^{2+} and Pb^{2+} ions under identical experimental conditions. The relative changes in the absorbance of the probe **AQC** upon the addition of different metal ions are shown in Figure 4.7A. The selectivity of the probe **AQC** can be observed visually, since the changes in color of **AQC** from yellow to colorless and yellow to pink observed only upon addition of Cu^{2+} and Hg^{2+} metal ions, respectively. Interestingly, the presence of all other metal ions used for the present studies showed negligible changes in the absorption spectra of the probe **AQC** as can be seen from Figure 4.7. Similarly, we have carried out the interactions of the model compound **EQC** with various metal ions.

Expectedly, **EQC** showed negligible interactions with the monovalent and divalent metal ions including Cu^{2+} ions under identical conditions (Figure 4.7B). However, with the addition of Hg^{2+} ions, we observed the color change from yellow to pink, thereby indicating that the model compound **EQC** exhibits selective interactions only with Hg^{2+} ions as compared to other ions.

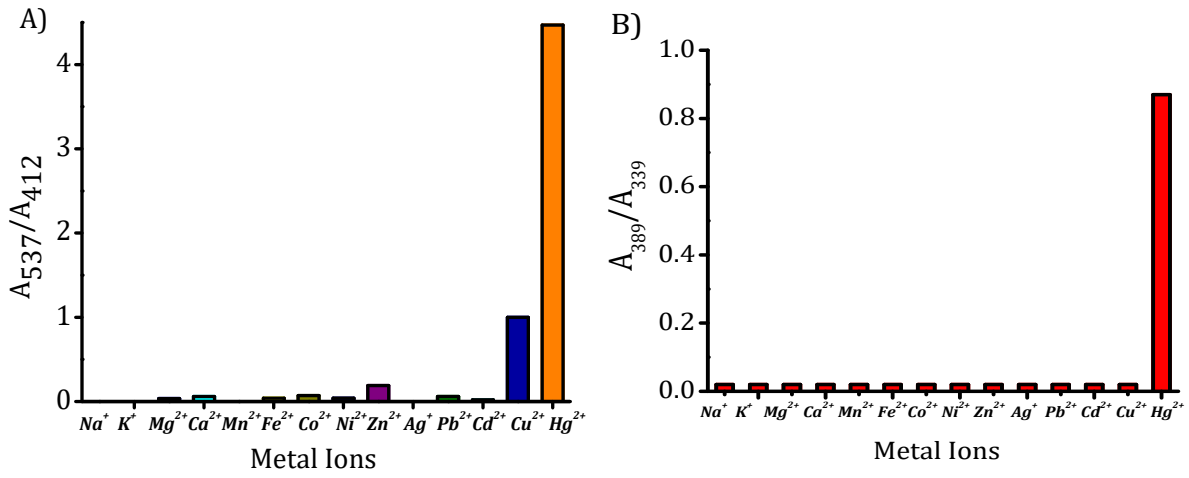

Figure 4.7. Selectivity graph showing the changes in absorbance ratio (A_{537}/A_{412}) of the probe **AQC** (10 μM) (A) and ratio (A_{389}/A_{339}) of the probe **EQC** (10 μM) (B) by the addition of different metal ions (10^{-4} M).

To test the potential of the probe **AQC** in presence of a mixture of metal ions, we have investigated the impact of the metal ions such as Na^+, K^+, Ag^+, Mg^{2+}, Ca^{2+}, Mn^{2+}, Fe^{2+}, Co^{2+}, Ni^{2+}, Zn^{2+}, Cd^{2+} and Pb^{2+}. As shown in Figure 4.8 and Figure 4.9, the presence of metal ions, including Na^+, K^+, Ag^+, Mg^{2+}, Ca^{2+}, Mn^{2+}, Fe^{2+}, Co^{2+}, Ni^{2+}, Cd^{2+} and Pb^{2+}, showed negligible effect on the detection and selectivity of **AQC** for Cu^{2+} and Hg^{2+} ions. Further to investigate the role of different anions, we carried out a series of experiments using counter ions such as perchlorate, chloride and acetate salts of Cu^{2+} and Hg^{2+} ions, respectively. Interestingly, upon changing the counter ion from the

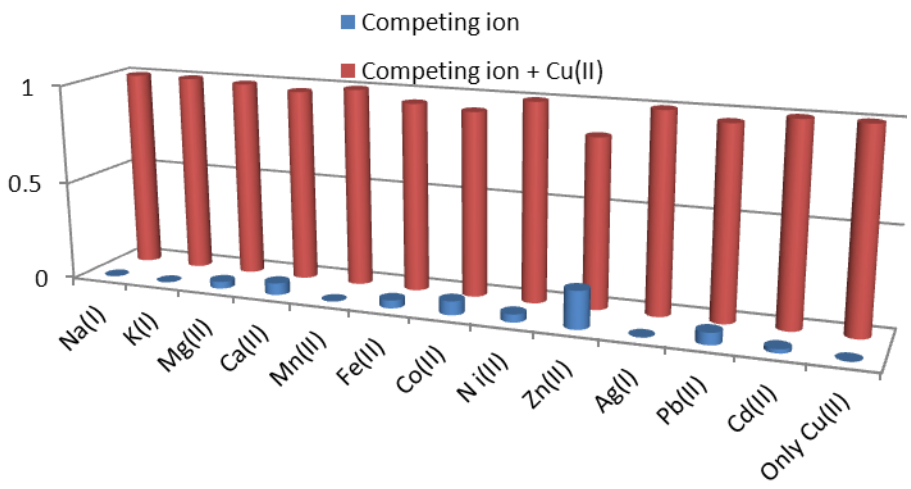

Figure 4.8. The changes in absorbance (A_{530}/A_{412}) of **AQC** (10^{-5} M) in acetonitrile in the presence of competing metal ions. The blue bars represent the absorbance ratio of **AQC** in the presence of the selected cations (10^{-5} M). The red bars represent the change in absorbance ratio that occurs upon subsequent addition of Cu^{2+} (10^{-5} M) to the above mentioned solutions, respectively.

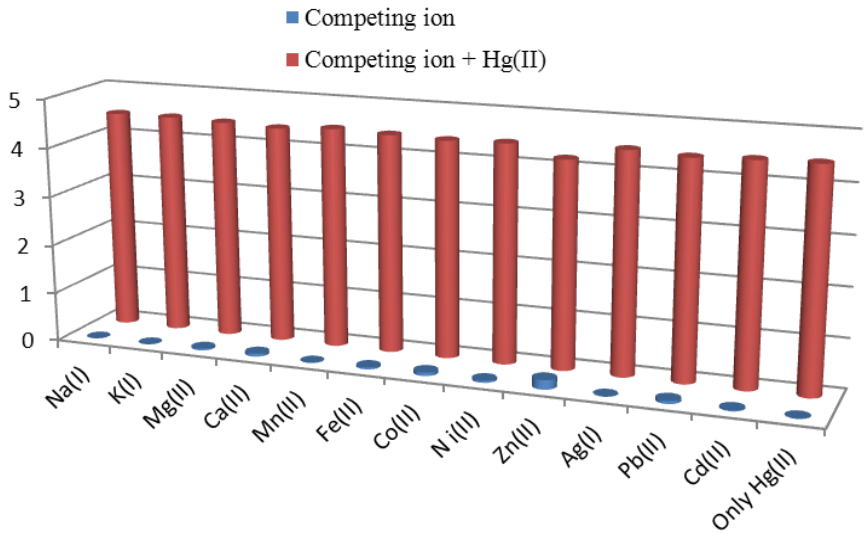

Figure 4.9. The changes in absorbance (A_{537}/A_{412}) of **AQC** (10^{-5} M) in acetonitrile in the presence of selected metal ions. The blue bars represent the absorbance ratio of **AQC** in the presence of the selected cations (10^{-5} M). The red bars represent the change in absorbance ratio that occurs upon subsequent addition of Hg^{2+} (10^{-5} M) to the above mentioned solutions, respectively.

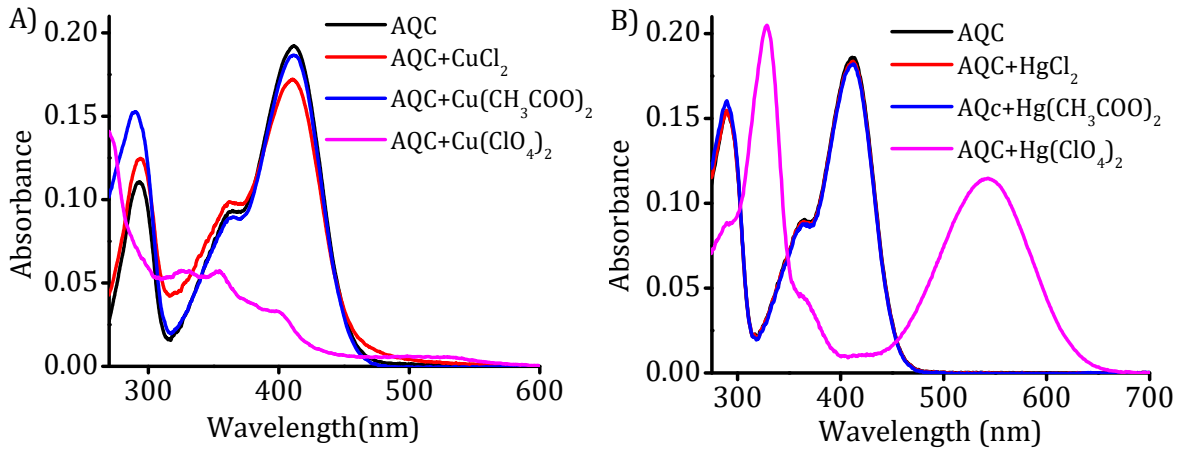

Figure 4.10. A) Changes in the absorption spectra of **AQC** (10^{-5}M) by the addition of different copper anions (10^{-5}M) B) Changes in absorption spectra of **AQC** (10^{-5}M) by the addition of different mercury anions(10^{-5}M).

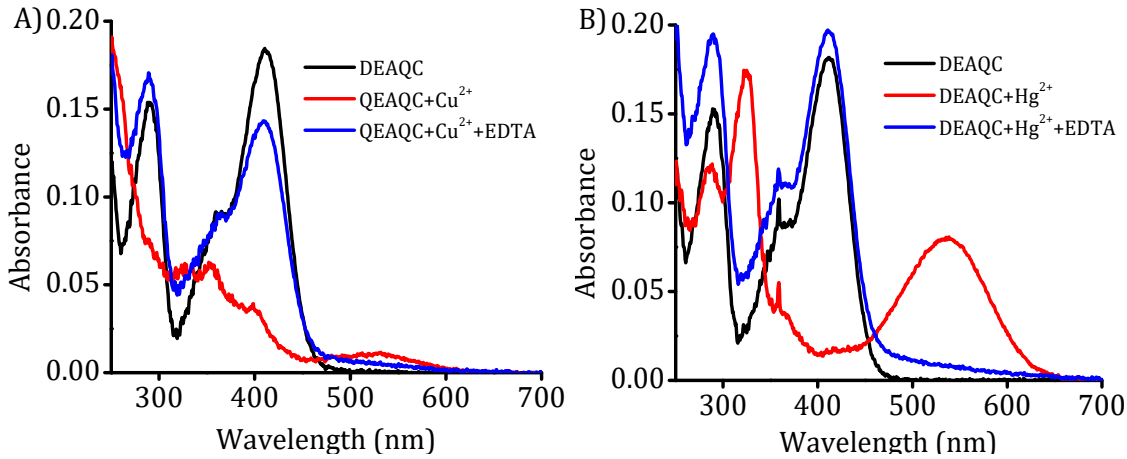

Figure 4.11. Reversibility of the complex formation with the addition of 1 eq of EDTA (10 μM). A) **AQC**-Cu^{2+} and B) **AQC**-Hg^{2+} complexes in CH_3CN.

perchlorate to chloride the affinity of the probe towards Cu^{2+} ions exhibited non-negligible decrease, while negligible effect was observed with the acetate ions (Figure 4.10A). In contrast, both the chloride and acetate salts of Hg^{2+} showed negligible influence on the detection by the probe **AQC** (Figure 4.10B).

To investigate the reversibility of the complexation of the probe **AQC** with Cu^{2+}

and Hg^{2+} ions, we have investigated the interaction of the probe with a strong chelator, ethylenediaminetetraacetic acid (EDTA)[3] (Figure 4.11). The probe **AQC** initially showed absorption and fluorescence emission maxima at 412 and 506 nm, which upon addition of one equivalent of Cu^{2+} and Hg^{2+} ions resulted in a significant decrease in the absorbance as well as quenching of fluorescence intensity. When EDTA was added to the solution of [**AQC**-(Hg^{2+}/Cu^{2+})] complexes, we observed the reversibility with an increase in both the absorbance and fluorescence intensity. This is due to the fact that EDTA is a strong chelating agent, which has higher affinity for metal ions (10^{21} M^{-1} for Hg^{2+} and 10^{18} M^{-1} for Cu^{2+}), when compared to the probe **AQC**.

4.3.4. Nature of the complexation

To understand the mode of binding of the probe **AQC** with the Cu^{2+} and Hg^{2+} ions, we have investigated its complexation process through Job plot, Benesi-Hildebrand method, ^{1}H NMR, Fourier transform infrared spectral (FT-IR), MALDI-TOF MS and cyclic voltammetry (CV) techniques. The stoichiometry for the binding of the probe **AQC** was examined by the method of continuous variation of ratio of mole fraction (Job's plot)[15]. We observed the stoichiometry of 1:1 and 2:1 for the complexes **AQC**-Cu^{2+} (Figure 4.12A) and **AQC**-Hg^{2+} (Figure 4.12B), respectively. Similarly, the stoichiometry of the binding for the model compound **EQC** was estimated and it is found to be 2:1 for **EQC**-Hg^{2+} complex (Figure 4.13).

The association constants of the probe **AQC** with these metal ions were calculated using the Benesi-Hildebrand analysis[16] utilizing the absorption titration data. We observed the association constant values of *ca.* $2.1 \pm 0.1 \times 10^4$ M^{-1} and $1.29 \pm 0.2 \times$

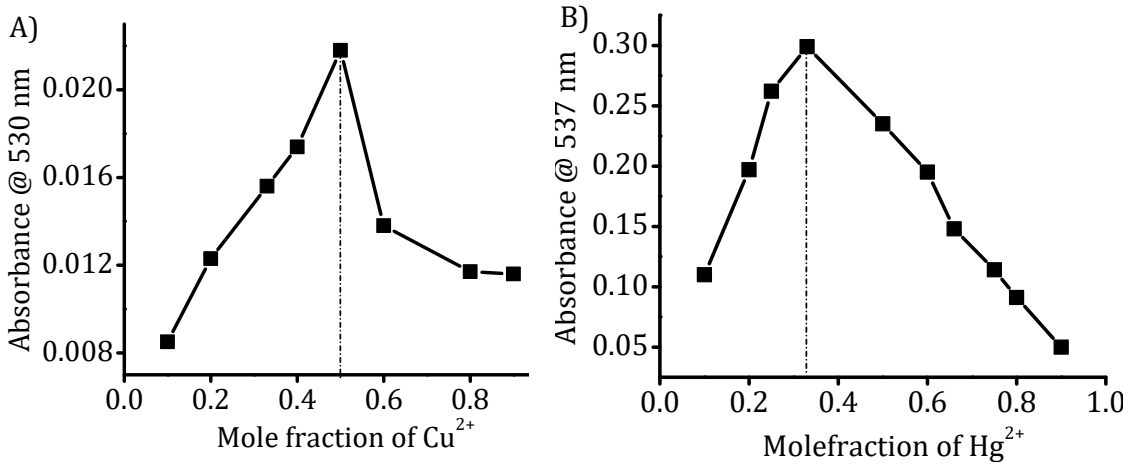

Figure 4.12: Job plot analysis for the complexation of probe **AQC** (33 μM) with A) Cu^{2+} (33 μM) and B) Hg^{2+} ions (33 μM) in CH_3CN.

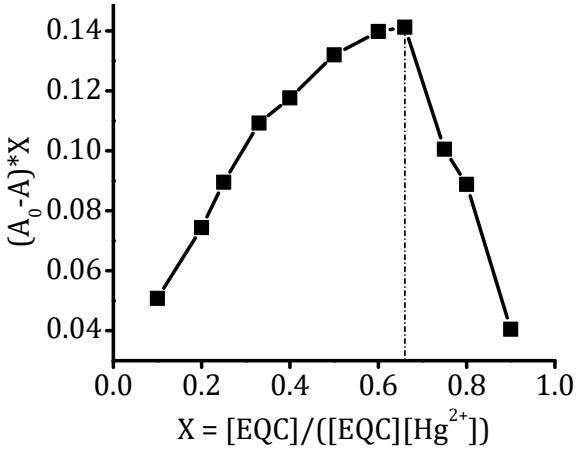

Figure 4.13: Job plot analysis for the complexation of the model compound **EQC** (33 μM) with Hg^{2+} ions (33 μM) in CH_3CN.

10^8 M^{-2} for **AQC**-Cu^{2+} (Figure 4.14A) and **AQC**-Hg^{2+} (Figure 4.14B) complexes, respectively. From the titration results, the detection limit was found to be 25 ppb (Figure 4.15A) for Cu^{2+} ions, whereas the sensitivity was observed to be 360 ppb for Hg^{2+} ions (Figure 4.15B) under identical conditions. The sensitivity in detection of about *ca.* 25 and 360 ppb for Cu^{2+} and Hg^{2+} ions is quite high when compared to the literature reported sensors by 10-15 and 2-3 fold respectively.[17]

We have carried out ^{1}H NMR spectral changes of the probe **AQC** in the presence and absence of different concentrations of Cu^{2+} and Hg^{2+} ions in CD_3CN (Figure 4.16 and 4.17) to confirm the nature of the complexation. The ^{1}H NMR spectrum of the probe **AQC** in CD_3CN showed one aldehyde proton H1 as a singlet at δ 9.99, five aromatic protons H2, H3, H4, H5 and H6 at δ 8.05, 7.79, 6.91, 7.44-7.48 and 7.96

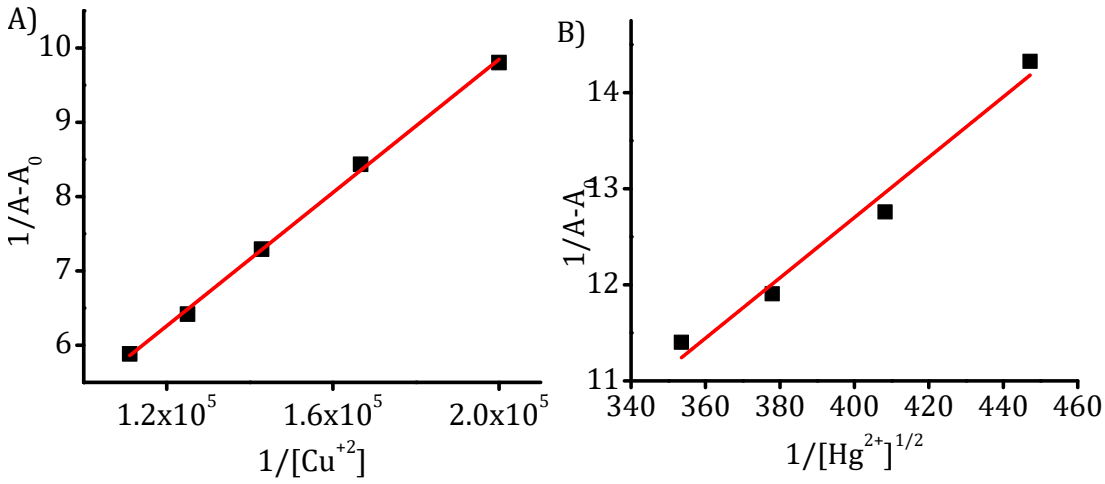

Figure 4.14: Benesi–Hildebrand fit for A) **AQC**-$Cu^{2+}$and B) **AQC**-Hg^{2+} complexes with the titration of the probe **AQC** (10 μM) with metal ions in acetonitrile.

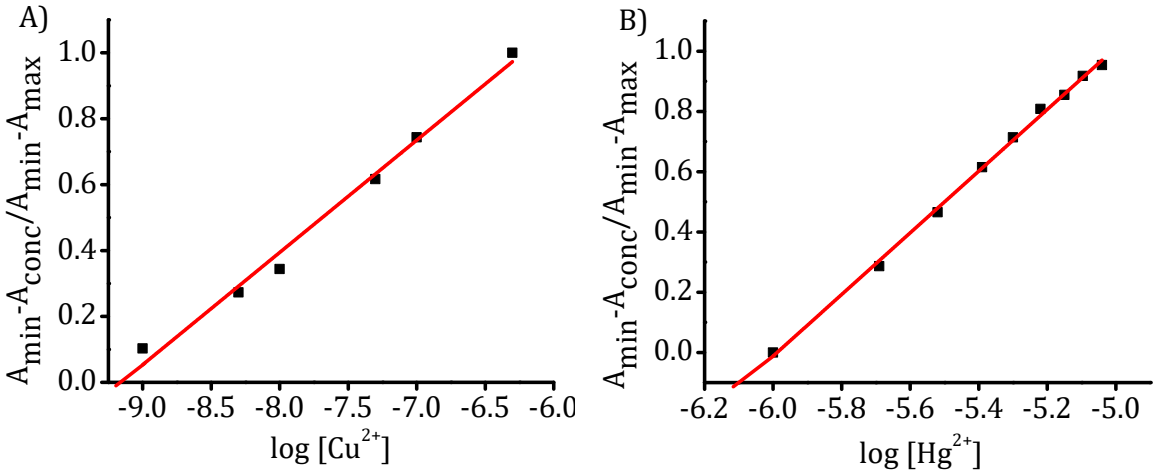

Figure 4.15: Linear plot of relative absorbance changes of the probe **AQC** in CH_3CN vs A) log [Cu^{2+}] and B) log[Hg^{2+}].

respectively. Whereas the *N*-CH_2 protons (H7 protons) appeared as a quartet at δ 3.51-3.56 while -CH_3 protons observed (H8 protons) at 1.23 as a triplet. With the increase in the addition of Cu^{2+} ions concentration, we observed a significant decrease in the intensity and broadening of the peaks in the ^1H NMR spectrum of the probe **AQC**. At 1 eq of Cu^{2+} ions, we observed the disappearance of the peaks corresponding to H4, H5 and H7 protons, while broadening of the protons was observed with H2, H3, and H6 protons due to the presence of highly paramagnetic Cu^{2+} ions in the near vicinity.[18] However, the peak corresponding to the aldehyde at δ 9.99 remained unaffected. The selective broadening, and disappearance of the -N-CH_2 protons (H7) and the aromatic protons H4 and H5 near to -N-CH_2 indicate that Cu^{2+} ions coordinate with the diethylamino moiety of the probe **AQC** (Figure 4.16). In contrast, with the increase in the addition of Hg^{2+} ions concentration, the aldehyde proton H1 at δ 9.99 showed a significant down field shift of $\Delta\delta$ = 0.23. The quinoline aromatic protons H2, H3, H4, H5 and H6 also showed a regular down field shift with the gradual addition of Hg^{2+} ions. On the other hand, aliphatic N-CH_2 protons (H7) and -CH_3 protons (H8), showed negligible changes in their chemical shifts. These observations indicate the co-ordination of the Hg^{2+} ions with both the aldehyde oxygen and the quinoline nitrogen functionalities of the probe **AQC** (Figure 4.17).

Further evidence for the coordination complexes was obtained through the analysis of the infrared spectrum (FT-IR) of **AQC** in presence and absence of Cu^{2+} and Hg^{2+} ions. The characteristic carbonyl stretching frequency of the probe **AQC** appeared at 1695 cm^{-1} (Figure 4.18A). On co-ordination with Cu^{2+} ions, we observed a shift in the -C=O stretching frequency to higher wave numbers from 1695 to 1704 cm^{-1}, which

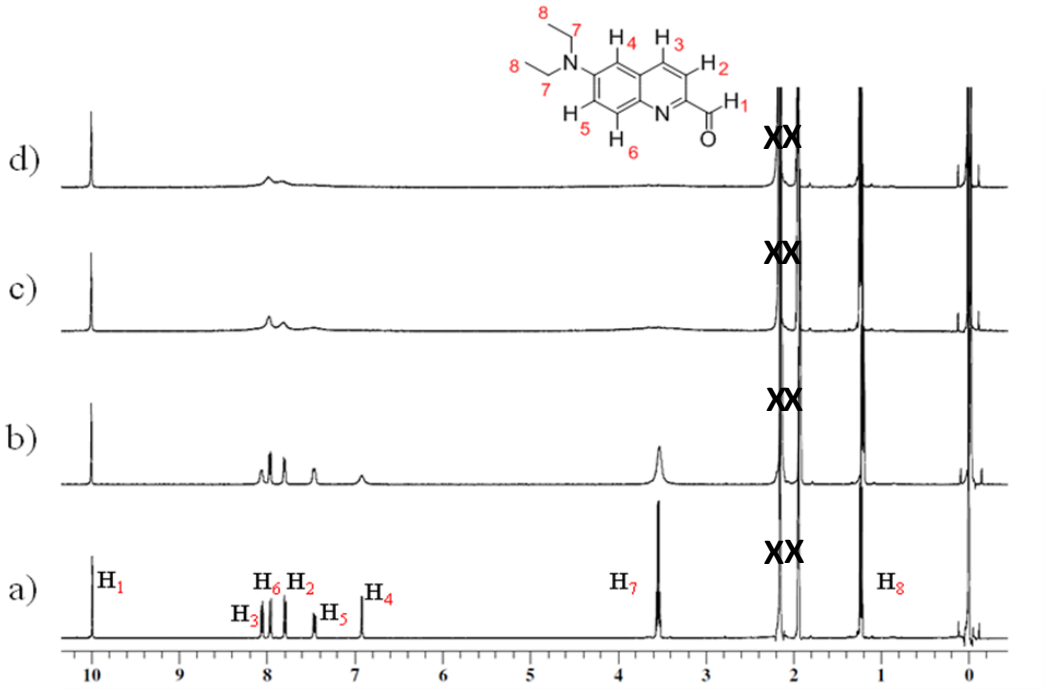

Figure 4.16: Changes in the ^{1}H NMR spectra of the probe **AQC** with the addition of Cu^{2+} ions in CD_3CN. a) **AQC** alone, b) 0.2 eq, c) 0.5 eq, d) 1 eq of Cu^{2+} ions.

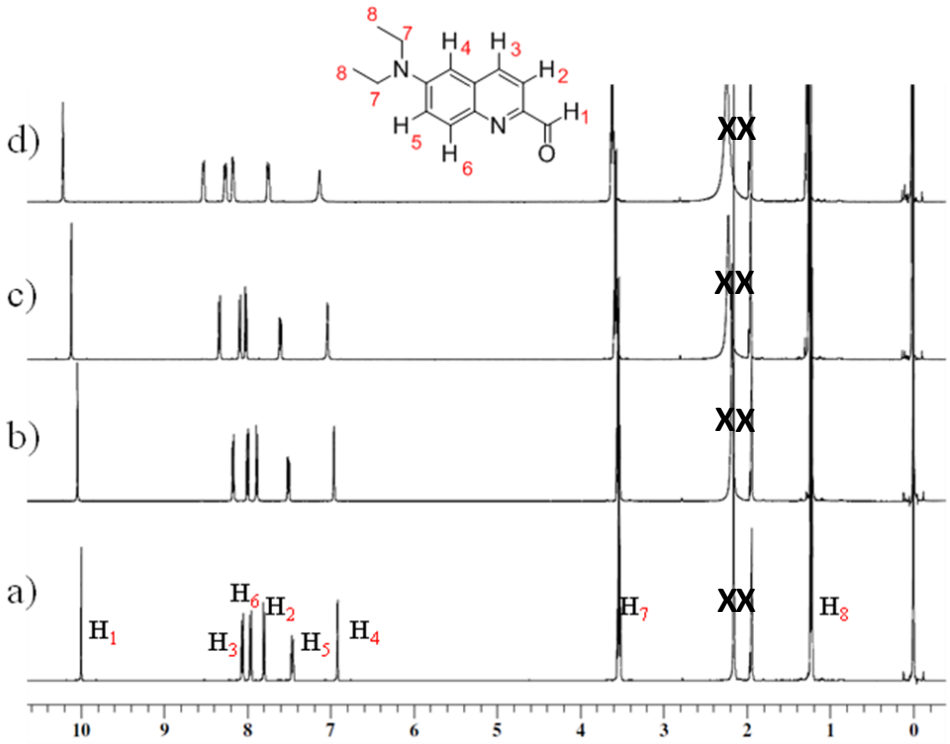

Figure 4.17: Changes in the ^{1}H NMR spectra of the probe **AQC** with the addition of Hg^{2+} ions in CD_3CN. a) **AQC** alone, b) 0.1 eq, c) 0.2 eq, d) 0.5 eq of Hg^{2+} ions.

indicates the coordination of the aliphatic nitrogen (-N-CH_2) with the Cu^{2+} ions (Figure 4.18B). In the case of Hg^{2+} ions, we observed a shift in -C=O stretching frequency to lower wave numbers from 1695 to 1668 cm^{-1} as compared to the free probe (Figure 4.18C). This indicates the coordination of aldehyde oxygen and quinoline nitrogen of the probe **AQC** with Hg^{2+} ions. The strong peaks observed at 1090 and 1096 cm^{-1} in the IR-spectra of **AQC**-Cu^{2+} and **AQC**-Hg^{2+} complexes could be attributed due to the presence of non-coordinated perchlorate ions in both these complexes.

Furthermore, we have analyzed the complexation through MALDI-TOF mass spectral analysis. We observed a peak at 332 corresponding to **AQC**-Cu^{2+}-CH_3CN complex (Figure 4.19) in the mass spectrum indicating the formation of a 1:1 stoichiometric complex between **AQC** and Cu^{2+} ions. However, the complex formed between the probe **AQC** and Hg^{2+}, showed a peak at 674.6 for [(**AQC**)$_2$-Hg^{2+}-H_2O], (Figure 4.20), which corresponds to a 2:1 stoichiometry for the complex between **AQC** and Hg^{2+} ions.

The cyclic voltammogram (CV) of **AQC** using tetrabutylammonium hexafluorophosphate as the supporting electrolyte at a scan speed of 100 mV/s showed one irreversible redox potential value of 0.95 V (Figure 4.21). This value could be attributed to the first oxidation of N,N-diethylamine group. With the addition of 1.0 eq of Cu^{2+} ions to the solution of **AQC**, we observed a shift in the first oxidation value to 0.97 V. The observed increase in the oxidation potential of **AQC** could be attributed to the coordination of the diethylamino group with Cu^{2+} ions. In the case of Hg^{2+} ions, with the addition of 0.5 eq, we observed the first oxidation potential value shift from 0.95 to 0.90 V. The observed decrease in the redox potential of **AQC** could be attributed to the

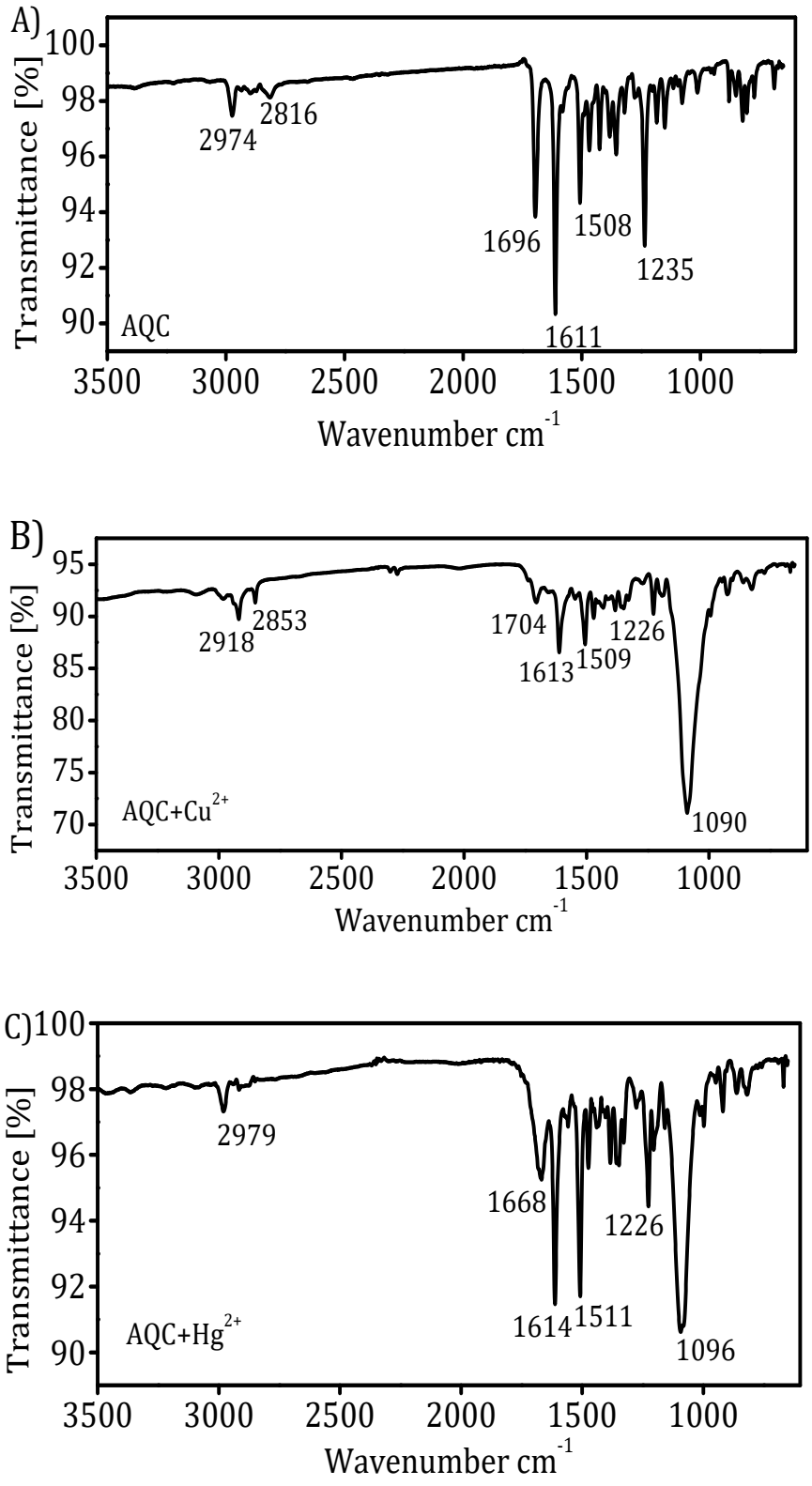

Figure 4.18. IR spectra of **AQC** (A), **AQC**-Cu^{2+} (B) and **AQC**-Hg^{2+} (C) complexes.

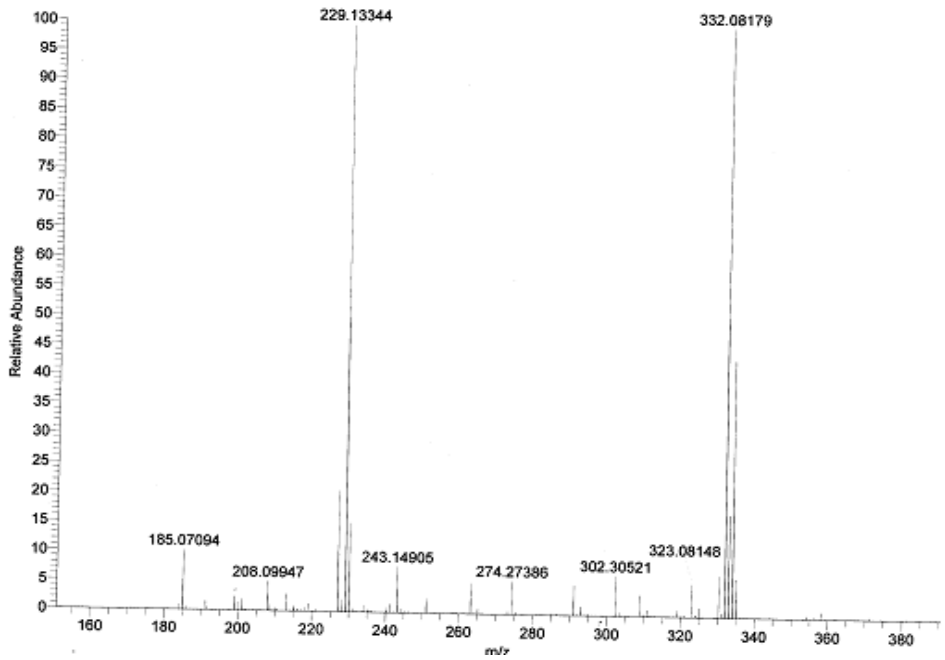

Figure 4.19. MALDI-TOF mass spectrum of an acetonitrile solution of **AQC** containing 1eq of $Cu(ClO_4)_2$.

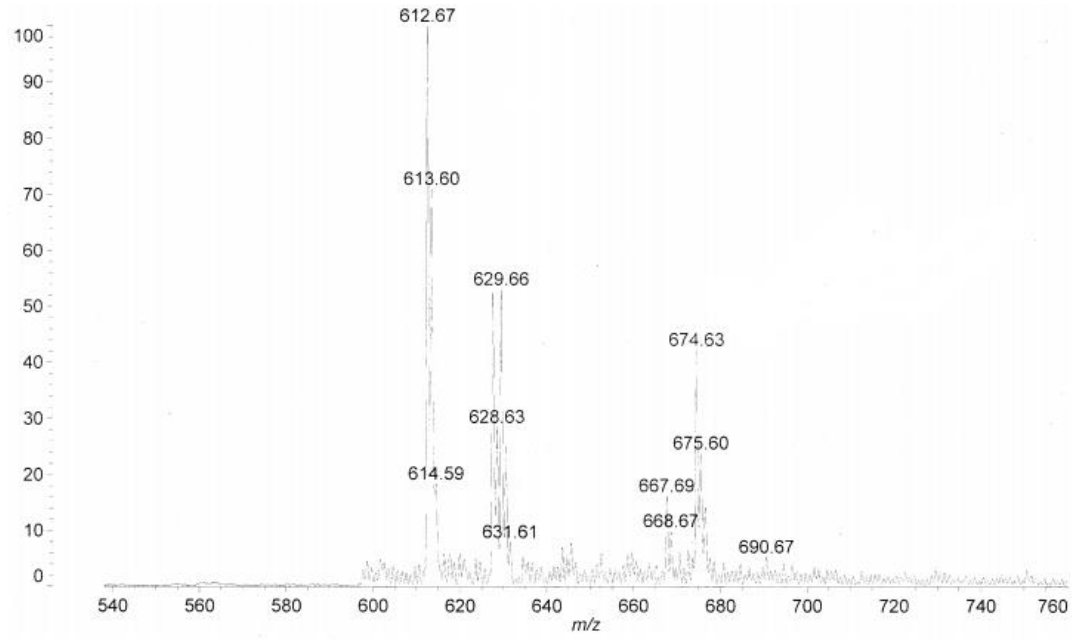

Figure 4.20. MALDI-TOF mass spectrum of an acetonitrile solution of **AQC** containing 0.5eq of $Hg(ClO_4)_2$.

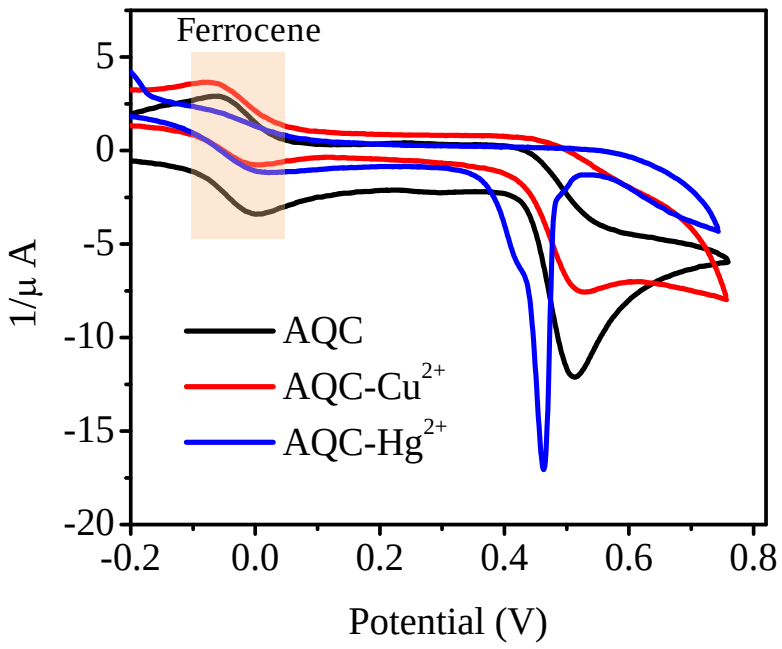

Figure 4.21. Cyclic voltammogram of **AQC** in CH_3CN.

coordination of the quinoline nitrogen moiety and aldehyde oxygen atoms with Hg^{2+} ions. These observations are in accordance with the literature reports known for the donor-acceptor systems.[19]

Based on these experimental evidences, we propose the structures shown in Chart 4.2 for the metal co-ordinated complexes of the probe **AQC** and the model compound **EQC** with the Cu^{2+} and Hg^{2+} ions. In the case of the **AQC**-Cu^{2+} complex, the preferential site for Cu^{2+} ions binding is the diethylamino group with a 1:1 stoichiometry. In contrast, the Hg^{2+} ions in the complexes **AQC**-Hg^{2+} and **EQC**-Hg^{2+} show the coordination with both the aldehyde oxygen and quinolone nitrogen atoms with a 2:1 stoichiometry. Interestingly such a distinctive binding of the probe **AQC** results in the selective and sensitive colorimetric detection of both Cu^{2+} and Hg^{2+} ions.

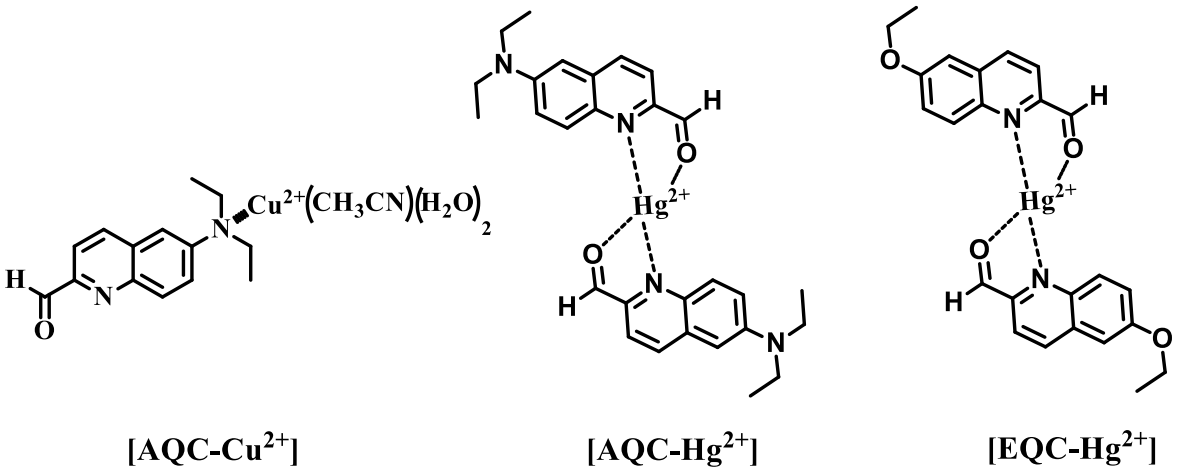

Chart 4.2. Proposed structures for complexes **AQC**-Cu^{2+}, **AQC**-Hg^{2+} and **EQC**-Hg^{2+}.

4.3.5. Detection of metal ions using dipstick method

To evaluate the versatility of the probe, we have prepared a "dipstick" based on the probe **AQC** for the detection of Cu^{2+} and Hg^{2+} ions in the aqueous medium. For this purpose, the probe **AQC** (1 mg) was adsorbed over silica (2 g), a slurry of which was coated on a glass stick as support (Figure 4.22A). The probe **AQC** alone showed yellow color when coated on the glass surface. The color of the dipstick changed from yellow to colorless when dipped in a solution containing 50 μM concentration of Cu^{2+} ions in the aqueous medium (Figure 4.22B). Similarly, when the probe coated dip-stick was dipped in a solution containing Hg^{2+} ions, its color changed from yellow to pink (Figure 4.22**C**). These results demonstrate the simple and convenient method and for the sensitive and selective detection and on-site analysis of Cu^{2+} and Hg^{2+} ions in the aqueous medium.

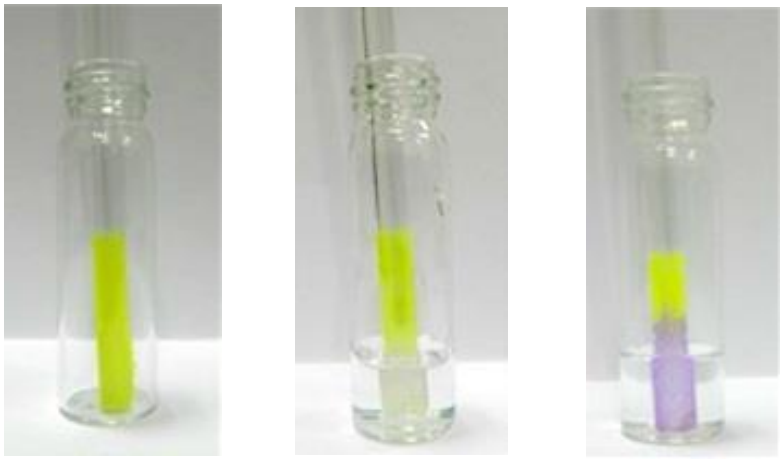

Figure 4.22. Photograph of the dipstick device showing the detection of metal ions (5×10^{-5} M) by the probe **AQC** in aqueous solution. A) The probe **AQC** (yellow color) coated over a glass support, the change in color of the dipstick from intense yellow to B) colorless in presence of Cu^{2+} ions and C) pink in the presence of Hg^{2+} ions.

4.4. Conclusions

In summary, we have developed a simple colorimetric probe **AQC** having diethylamino and quinoline-2-carbaldehyde functional units. This probe showed profound selectivity towards both Cu^{2+} and Hg^{2+} ions as compared to other metal ions and signaled the event through ratiometric absorption changes. The uniqueness of this probe is that it forms stable complexes with Cu^{2+} and Hg^{2+} ions and exhibits different binding sites and acts as a visual colorimetric probe for the selective detection of Cu^{2+} and Hg^{2+} ions. The 1:1 stoichiometric complexation with Cu^{2+} ions showed a color change from yellow to colorless, while with Hg^{2+} ions, it showed a 2:1 stoichiometric complexation and the color change from yellow to pink. Uniquely, the probe **AQC** can be effectively coated on the solid support to make a dipstick, which can be used for a

simple, selective, sensitive and dual mode detection and on-site analysis of both Cu^{2+} and Hg^{2+} ions in the aqueous medium.

4.5. Experimental Section

4.5.1. General techniques

The melting points were determined on a Mel-Temp II melting point apparatus. The electronic absorption spectra were recorded on a Shimadzu UV-3101 spectrophotometer. The fluorescence spectra were recorded on a SPEX-Fluorolog F112X spectrofluorimeter. ^{1}H NMR spectra were recorded on a 500 MHz Bruker Avance DPX spectrometer. The mass spectra were recorded on Thermo Scientific Exactive ESI-MS spectrophotometer. MALDI-TOF MS analysis was performed with a Shimadzu Biotech Axima CFR plus instrument equipped with a nitrogen laser in the linear mode using 2,5- dihydroxybenzoicacid (DHB) as the matrix. The FT-IR spectra were recorded on a Perkin Elmer Model 882 Infrared spectrometer. Cyclic voltammetric measurements were performed on a BAS CV50W voltammetric analyzer; using 1 mM probe solution in acetonitrile at a scan rate of 100 mV/s using 0.1 M tetrabutylammonium hexafluorophosphate as supporting electrolyte. The glassy carbon, standard calomel electrode and platinum wires were used as working, reference and auxiliary electrodes, respectively, and internally calibrated with ferrocene. First oxidation wave potentials were calculated by the addition of 0.44 V to the potentials measured vs ferrocene.

All the solvents were purified and distilled before use. Quantum yields of

fluorescence were determined by the relative methods using optically dilute solutions. Quinine sulphate in 0.1 M H_2SO_4, with a quantum yield of 0.54,[41] was used as the standard and the quantum yields of fluorescence were calculated using the equation 4.1.

$$\Phi_F = \frac{A_s F_u n_u^2}{A_u F_s n_s^2} \Phi_s \quad \ldots\ldots\ldots\ldots\ldots 4.1.$$

wherein A_s and A_u are the absorbance of the standard and unknown, respectively; F_s and F_u are the areas of fluorescence peaks of the standard and unknown, respectively; and n_s and n_u are the refractive indices of the standard and unknown solvents, respectively. Φ_s and Φ_F are the fluorescence quantum yields of the standard and unknown, respectively.

4.5.2. Materials

All the reagents used for synthesis and measurements were purchased from Sigma–Aldrich (MO, USA), in analytical grade and used as received, unless otherwise stated. The measurements related to the cations of Mn^{2+}, Fe^{2+}, Co^{2+}, Ni^{2+}, Cu^{2+}, Zn^{2+}, Hg^{2+}, Cd^{2+}, Pb^{2+}, Ag^{+}, Mg^{2+}, Ca^{2+}, K^{+} and Na^{+} were obtained by using their perchlorate salts. Metal ions, probe **AQC** and the model compound **EQC** were dissolved in acetonitrile to obtain 1 mM stock solutions. Before spectroscopic measurements, the solution was freshly prepared by diluting the concentrated stock solution to the required concentration. 6-Amino-2-quinaldine, mp 181-183 °C (mixture mp 185-187 °C), and 6-ethoxyquinoline-2-carbaldehyde (**EQC**), mp 104-106 °C (mixture mp 100-101° C) were prepared as per the reported procedures.

4.5.3. Calculation of association constants

The association constants between the probes **AQC** / **EQC** and Cu^{2+}/ Hg^{2+} ions were analyzed using the absorption data and were calculated employing Benesi-Hildebrand equations 4. 2 and 4. 3,

$$\frac{1}{(A - A_0)} = \frac{1}{(A - A_0)} + \frac{1}{K\,(A - A_c)[Cu^{2+}]} \ldots\ldots\ldots\ldots \quad 4.2.$$

$$\frac{1}{(A - A_0)} = \frac{1}{(A - A_0)} + \frac{1}{K\,(A - A_c)[Hg^{2+}]^{1/2}} \ldots\ldots\ldots\ldots \quad 4.3.$$

wherein K is the association constant, A is the absorbance of the free dyad, A_0 is the observed absorbance of the [dyad-M^{2+}] complex, and A_c is absorbance at the saturation.

4.5.4. Computational details

Quantum chemical calculations have been performed based on the density functional theory (DFT) using Gaussian 09 software. The ground state geometry optimization of probe **AQC** has been carried out at the DFT-B3LYP /6-311G (d,p) level followed by the vibrational frequency analysis to ensure that the obtained geometries represent minima on potential energy surface. The HOMO and LUMO pictures were obtained by using gauss-view program.

4.5.5. Synthesis and characterization

***N, N-diethyl-6-amino-2-quinaldine (3)*.** To a solution of 6-amino-2-quinaldine (2 g, 12.6 mmol) in dry DMF (10 mL) under argon atmosphere, activated K_2CO_3 (5.216 g, 37.8 mmol) was added and stirred at 25 °C for 30 min. To this mixture ethyl iodide (5.89 g, 37.8 mmol) was added slowly to the reaction mixture and stirring was continued for 8 h at 25 °C. The solvent was removed under vacuum and extracted with ethyl acetate. The combined organic layer was washed with brine solution and dried over Na_2SO_4, evaporated and purified through silica gel column chromatography (ethyl acetate / petroleum ether 1:9) to afford N,N-diethyl-6-amino-2-quinaldine (2.6 g, 81%). ^{1}H NMR ($CDCl_3$, 500 MHz) δ 7.78 (d, J = 9.41 Hz, 1H), 7.73 (d, J = 8.51 Hz, 1H), 7.17-7.21 (m, 1H), 7.05 (d, J = 8.51 Hz, 1H), 6.66 (*s*, 1H), 3.35-3.40 (q, J = 7.25 Hz, 4H), 2.58 (s, 3H), 1.14 (t, J = 7. 25 Hz, 6H); ESI-MS: m/z Cald for $C_{14}H_{18}N_2$ 214.31 and Found $[M]^+$ 214.86.

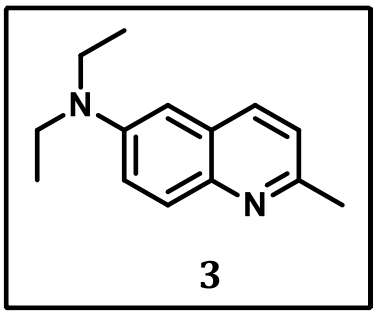

3

6-(diethylamino)quinoline-2-carbaldehyde (AQC): Selenium dioxide (1.66 g, 15 mmol) in dioxane suspension was heated at 60 °C and then N,N-diethyl-6-amino-2-quinaldine (2.14 g, 10 mmol) was introduced. The mixture was heated at 80 °C for 3 h. After cooling to room temperature, the reaction mixture was filtered on celite, evaporated and purified through silica gel column chromatography (ethyl acetate/petroleum ether 5:95) to afford **AQC** (2 g, 74%). mp 56 °C. ^{1}H NMR (CD_3CN, 500 MHz) δ 9.99 (s, 1H), 8.05 (d, J =

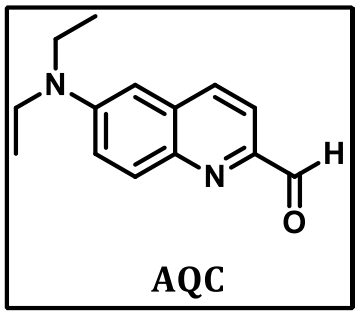

AQC

8.5 Hz, 1H), 7.96 (d, *J* = 9.4 Hz, 1H), 7.79 (d, *J* = 8.5 Hz, 1H), 7.44-7.48 (dd, *J* = 9.4, 1H), 6.91 (s, 1H), 3.51-3.56 (q, *J* = 6.9 Hz, 4H), 1.23 (t, *J* = 6.9 Hz, 6H); ESI-MS: m/z Cald for $C_{14}H_{16}N_2O$ 228.30 and Found 229.37 $[M+H]^+$.

4.6. References

(1) (a) Mi, Y. S.; Cao, Z.; Chen, Y. T.; Xie, Q. F.; Xu, Y. Y.; Luo, Y. F.; Shi, J. J.; Xiang, J. N. *Analyst* 2013, *138*, 5274(b) Mei, Q.; Wang, L.; Tian, B.; Yan, F.; Zhang, B.; Huang, W.; Tong, B. *New J. Chem.* 2012, *36*, 1879(c) Shankar, B. H.; Ramaiah, D. *J. Phys. Chem. B* 2011, *115*, 13292(d) Jisha, V. S.; Thomas, A. J.; Ramaiah, D. *J. Org. Chem.* 2009, *74*, 6667(e) Avirah, R. R.; Jyothish, K.; Ramaiah, D. *Org. Lett.* 2007, *9*, 121.

(2) Magos, L. *J. Appl. Toxicol.* 1988, *8*, 150.

(3) Rice, K. M.; Walker, E. M.; Wu, M.; Gillette, C.; Blough, E. R. *J. Prev. Med. Public Health* 2014, *47*, 74.

(4) Krämer, R. *Angew. Chem. Int. Ed.* 1998, *37*, 772.

(5) Koval, I. A.; Gamez, P.; Belle, C.; Selmeczi, K.; Reedijk, J. *Chem. Soc. Rev.* 2006, *35*, 814.

(6) (a) Deraeve, C.; Boldron, C.; Maraval, A.; Mazarguil, H.; Gornitzka, H.; Vendier, L.; Pitié, M.; Meunier, B. *Chem. Eur. J.* 2008, *14*, 682(b) Gaggelli, E.; Kozlowski, H.; Valensin, D.; Valensin, G. *Chem. Rev.* 2006, *106*, 1995(c) Barnham, K. J.; Masters, C. L.; Bush, A. I. *Nat. Rev. Drug Discov.* 2004, *3*, 205.

(7) (a) Karunakaran, S. C.; Paul, A. K.; Ramaiah, D. *RSC Adv.* 2014, *4*, 30644(b) Adarsh, N.; Shanmugasundaram, M.; Ramaiah, D. *Anal. Chem.* 2013, *85*, 10008(c) Narayanaswamy, N.; Govindaraju, T. *Sens. Actuators B, Chem.* 2012, *161*, 304(d)

Wu, Q.-Q.; Duan, X.-Y.; Song, Q.-H. *J. Phys. Chem. C* 2011, *115*, 23970(e) Suresh, P.; Azath, I. A.; Pitchumani, K. *Sens. Actuators B, Chem.* 2010, *146*, 273(f) Jisha, V. S.; Arun, K. T.; Hariharan, M.; Ramaiah, D. *J. Am. Chem. Soc.* 2006, *128*, 6024(g) de Silva, A. P.; Gunaratne, H. Q. N.; Gunnlaugsson, T.; Huxley, A. J. M.; McCoy, C. P.; Rademacher, J. T.; Rice, T. E. *Chem. Rev.* 1997, *97*, 1515.

(8) (a) Liu, Z.; Tonnelé, C.; Battagliarin, G.; Li, C.; Gropeanu, R. A.; Weil, T.; Surin, M.; Beljonne, D.; Lazzaroni, R.; Debliquy, M.; Renoirt, J.-M.; Müllen, K. *J. Phys. Chem. B* 2014, *118*, 309(b) Lee, H. Y.; Swamy, K. M. K.; Jung, J. Y.; Kim, G.; Yoon, J. *Sens. Actuators B, Chem.* 2013, *182*, 530(c) Jung, J. Y.; Kang, M.; Chun, J.; Lee, J.; Kim, J.; Kim, J.; Kim, Y.; Kim, S.-J.; Lee, C.; Yoon, J. *Chem. Commun.* 2013, *49*, 176(d) Svechkarev, D.; Dereka, B.; Doroshenko, A. *J. Phys. Chem. A* 2011, *115*, 4223(e) Chen, X.; Nam, S.-W.; Jou, M. J.; Kim, Y.; Kim, S.-J.; Park, S.; Yoon, J. *Org. Lett.* 2008, *10*, 5235.

(9) (a) Kim, H. N.; Ren, W. X.; Kim, J. S.; Yoon, J. *Chem. Soc. Rev.* 2012, *41*, 3210(b) Yuan, M.; Zhou, W.; Liu, X.; Zhu, M.; Li, J.; Yin, X.; Zheng, H.; Zuo, Z.; Ouyang, C.; Liu, H.; Li, Y.; Zhu, D. *J. Org. Chem.* 2008, *73*, 5008(c) Avirah, R. R.; Jyothish, K.; Ramaiah, D. *J. Org. Chem.* 2008, *73*, 274.

(10) Praveen, L.; Babu, J.; Reddy, M. L. P.; Luxmi Varma, R. *Tet. Lett.* 2012, *53*, 3951.

(11) Tahtaoui, C.; Guillier, F.; Klotz, P.; Galzi, J.-L.; Hibert, M.; Ilien, B. *J. Med. Chem.* 2005, *48*, 7847.

(12) Reichardt, C. *Chem. Rev.* 1994, *94*, 2319.

(13) Melhuish, W. H. *Journal of the Optical Society of America* 1964, *54*, 183.

(14) Nair, A. K.; Neelakandan, P. P.; Ramaiah, D. *Chem. Commun.* 2009, 6352.

(15) Zeng, L.; Miller, E. W.; Pralle, A.; Isacoff, E. Y.; Chang, C. J. *J. Am. Chem. Soc.* 2006, *128*, 10.

(16) Benesi, H. A.; Hildebrand, J. H. *J. Am. Chem. Soc.* 1949, *71*, 2703.

(17) (a) Kaur, K.; Kumar, S. *Dalton Trans.* 2011, *40*, 2451(b) Ou, S.; Lin, Z.; Duan, C.; Zhang, H.; Bai, Z. *Chem. Commun.* 2006, 4392.

(18) Satcher, J. H.; Balch, A. L. *Inorg. Chem.* 1995, *34*, 3371.

(19) (a) Chen, C.; Dong, H.; Chen, Y.; Guo, L.; Wang, Z.; Sun, J.-J.; Fu, N. *Org. Biomol. Chem.* 2011, *9*, 8195(b) Arunkumar, E.; Ajayaghosh, A.; Daub, J. *J. Am. Chem. Soc.* 2005, *127*, 3156.

List of publications

1. Design and synthesis of solution processable green fluorescent D-π-A dyads for OLED applications, **T. Shameel**, K. S. Sanju, A. Soman, K. N. N. Unni, J. Joseph, and D. Ramaiah, *New J. Chem.*, **2018**, *42*, 5456-5464.
2. Simple solution processable carbazole-oxadiazole hybrids for un-doped deep-blue OLEDs, **T. Shameel**, A. Soman, K. N. N. Unni, J. Joseph, and D. Ramaiah, *J. Photochem. Photobiol. A Chem.* **2018**, *358*, 192-200.
3. Simultaneous binding of a cyclophane and classical intercalators to DNA: observation of FRET-mediated white light emission, K. S. Sanju, **T. Shameel**, P. P. Neelakandan, J. Joseph and D. Ramaiah, *Phys. Chem. Chem. Phys.* **2015***, 17*, 13495-13500.
4. Selective and dual naked eye detection of Cu^{2+} and Hg^{2+} ions using a simple quinoline-carbaldehyde chemosensor, C. L. Devi, **T. Shameel**, B. H. Shankar and D. Ramaiah, *Sensors and Actuators B*, **2014,** *204,* 480–488.

List of papers/posters presented in conference proceedings

1. **T. Shameel**, A. Soman, K. N. N. Unni, J. Joseph and D. Ramaiah, Solution processable carbazole-oxadiazole luminescent systems for non-doped deep-blue OLEDs, A paper presented in National Conference on Luminescence and its Applications (NCLA), CSIR-NIIST, Thiruvananthapuram, Kerala, India, **2018**, February 14-16*.*
2. **T. Shameel**, K. S. Sanju, A. Soman, K. N. N. Unni, J. Joseph and D. Ramaiah, Solution processable green fluorescent emitters with low singlet-triplet energy gap for OLED applications, A poster presented in 8th East Asia Symposium (EAS8) 'Functional Dyes and Advanced Materials', CSIR-NIIST, Thiruvananthapuram, Kerala, India, **2017**, September 20-22.
3. **T. Shameel**, C. Lavanya devi, B. H. Shankar and D. Ramaiah, Selective and dual naked eye detection of Cu^{2+} and Hg^{2+} ions using a simple quinoline – carbaldehyde system, A poster presented in Materials Research Society of India (MRSI) Symposium 'Advanced Materials for Sustainable Applications', CSIR-NEIST, Jorhat, India, **2016**, February 18-20.